UNIVERSITY OF THESSALY
SCHOOL OF ENGINEERING
DEPARTMENT OF MECHANICAL ENGINEERING

ESTIMATION OF ACCOMMODATION COEFFICIENTS CHARACTERIZING GAS-SURFACE INTERACTION IN FULLY DEVELOPED RAREFIED GAS FLOWS THROUGH MICROCHANNELS

by
ALEXIOS VATIS

Submitted in partial fulfillment of the requirements for the degree of Diploma in Mechanical Engineering at the University of Thessaly

Volos, 2020

UNIVERSITY OF THESSALY
SCHOOL OF ENGINEERING
DEPARTMENT OF MECHANICAL ENGINEERING

ESTIMATION OF ACCOMMODATION COEFFICIENTS CHARACTERIZING GAS-SURFACE INTERACTION IN FULLY DEVELOPED RAREFIED GAS FLOWS THROUGH MICROCHANNELS

by
ALEXIOS VATIS

Submitted in partial fulfillment of the requirements for the degree of Diploma in Mechanical Engineering at the University of Thessaly

Volos, 2020

Approved by the Committee on Final Examination:

Advisor	Prof. Dimitris Valougeorgis, Professor, Department of Mechanical Engineering, University of Thessaly
Member	Dr. Giorgos Tatsios, Department of Mechanical Engineering, University of Thessaly
Member	Prof. Vasilis Bontozoglou, Professor, Department of Mechanical Engineering, University of Thessaly

Date Approved: [October 15, 2020]

ESTIMATION OF ACCOMMODATION COEFFICIENTS CHARACTERIZING GAS-SURFACE INTERACTION IN FULLY DEVELOPED RAREFIED GAS FLOWS THROUGH MICROCHANNELS

Alexios Vatis

Department of Mechanical Engineering, University of Thessaly

Supervisor: Prof. Dimitris Valougeorgis

Abstract

Pressure and temperature driven rarefied gas flows through long rectangular microchannels, including the interaction between the gas and the channel wall, have been extensively investigated due to their theoretical and technological interest. However, several issues related to the estimation of the accommodation coefficients characterizing the gas-surface interaction are still under investigation. In the present diploma thesis an attempt is made to further improve our understanding on this topic by comparing experimental and numerical results and deducing the accommodation coefficients based on reversed engineering practices. More specifically, based on specific experimental, geometrical and operational data, the deduced flow rates are computed and accordingly compared with the corresponding measured ones. The accommodation coefficients are identified in order to match the numerical with the experimental mass flow rates. This work is done for both the pressure and temperature driven flows and for five gases, namely Helium, Neon, Nitrogen, Argon, Krypton. The pressure driven flow is a Poiseuille type flow and the temperature one is the so-called thermal creep flow. The computed results are based on kinetic modeling using the linearized Shakhov kinetic model subject to Maxwell and Cercignani-Lampis boundary conditions. In the pressure driven flow a very good agreement between the computational and experimental results is achieved for both boundary conditions and all gases concluding to a suitable value for the accommodation coefficients. For each gas a specific value of the accommodation coefficient has been estimated providing excellent agreement between

computations and measurements in the whole range of gas rarefaction. On the contrary significant discrepancies have been observed in the temperature driven flow. The accommodation coefficients as well as the imposed temperature difference has been accordingly modified in order to improve the agreement. It has been found that the accommodation coefficients providing good agreement between computations and measurements are not constant and strongly depend on the temperature difference and the gas rarefaction parameter. Therefore, the obtained results cannot be generalized. Further work on this issue is required.

Key words: Kinetic theory, Shakhov, Maxwell, Cercignani-Lampis, microflows, gas-surface interaction, accommodation coefficients

ΥΠΟΛΟΓΙΣΜΟΣ ΤΩΝ ΣΥΝΤΕΛΕΣΤΩΝ ΑΛΛΗΛΕΠΙΔΡΑΣΗΣ ΑΕΡΙΟΥ-ΤΟΙΧΩΜΑΤΟΣ ΣΕ ΠΛΗΡΩΣ ΑΝΕΠΤΥΓΜΕΝΗ ΑΡΑΙΩΠΟΙΗΜΕΝΗ ΡΟΗ ΣΕ ΜΙΚΡΟΑΓΩΓΟΥΣ

Αλέξιος Βατής

Τμήμα Μηχανολόγων Μηχανικών, Πανεπιστήμιο Θεσσαλίας, 2020

Επιβλέπων Καθηγητής: Δημήτρης Βαλουγεώργης

Περίληψη

Τόσο στη ροή αραιωποιημένων αερίων σε αγωγούς ορθογωνικής διατομής λόγω διαφοράς πίεσης και θερμοκρασίας όσο και στην αλληλεπίδραση μεταξύ αερίου και τοιχώματος έχουν αφιερώθει πολλές μελέτες λόγω του επιστημονικού και τεχνολογικού ενδιαφέροντός τους. Ωστόσο, αρκετά θέματα σχετικά με τον υπολογισμό των συντελεστών που χαρακτηρίζουν την αλληλεπίδραση αερίου-τοιχώματος χρήζουν επιπλέον μελέτης. Στην παρούσα διπλωματική εργασία γίνεται μια προσπάθεια για την περαιτέρω κατανόηση στο ζήτημα αυτό, συγκρίνοντας πειραματικά και υπολογιστικά δεδομένα με απώτερο σκοπό την εξαγωγή των συντελεστών αλληλεπίδρασης. Πιο συγκεκριμένα, εφαρμόζοντας τις παραμέτρους του πειράματος, διαστάσεις και συνθήκες εφαρμογής, σε υπολογιστικό μοντέλο παράγονται οι μαζικές παροχές, οι οποίες συγκρίνονται με τις αντίστοιχες πειραματικές. Οι συντελεστές αλληλεπίδρασης με τη σειρά τους προσαρμόζονται ανάλογα, ώστε να υπάρξει ταύτιση μεταξύ των αποτελεσμάτων. Η συγκεκριμένη εργασία εστιάζει τόσο στην ροή λόγω διαφοράς πίεσης όσο και θερμοκρασίας, για πέντε αέρια (Ήλιο, Νέον, Άζωτο, Αργό, Κρύπτον). Η πρώτη περίπτωση είναι ροή τύπου Poiseuille, ενώ η δεύτερη είναι γνωστή ως θερμικός ερπισμός (thermal creep). Τα υπολογιστικά αποτελέσματα προέρχονται απο την επίλυση του γραμμικού κινητικού μοντέλου Shakhov εφαρμόζοντας συνοριακές συνθήκες τύπου Maxwell και Cercignani-Lampis. Για την ροή λόγω διαφοράς πίεσης η σύγκριση των υπολογιστικών και πειραματικών αποτελεσμάτων είναι ικανοποιητική και για τις δύο συνοριακές συνθήκες για όλα τα αέρια, με επακόλουθο την εξαγωγή κατάλληλης τιμής για τους συντελεστές αλληλεπίδρασης. Αντίθετα στη ροή λόγω διαφοράς θερμοκρασίας δεν επιτυγχάνεται ταύτιση μεταξύ των δύο μεθόδων και ως συνέπεια δεν μπορεί να προκύψει κάποια τιμή για τους συντελεστές αλληλεπίδρασης.

Λέξεις-κλειδιά: Κινητική θεωρία, Shakhov, Maxwell, Cercignani-Lampis, μικροροές, αλληλεπίδραση αερίου-τοιχώματος

Contents

LIST OF TABLES

LIST OF FIGURES

Chapter 1 **INTRODUCTION**

A brief presentation of the background theory is made to help the comprehension of the study and its purposes. Basic principles of kinetic theory are discussed along with the related equations such as the Boltzmann equation (BE) and the associated kinetic models with the implemented boundary conditions. Also, a review is made on similar studies and their contribution in solving modern flow problems.

1.1 Knudsen number and flow regimes

Based on the scale and conditions of the flow, different modeling approaches can be implemented. From a macroscopic scale the gas can be described thermodynamically or mechanically depending if it is in equilibrium or not, respectively. An example of these methods is the Navier-Stokes equations, which introduce the transport coefficients, i.e. thermal conductivity coefficient (k), dynamic viscosity (μ), diffusion coefficient (D) in order to provide valid results. On the other hand, if the approach is from a microscopic scale, where the motion of individual particles needs to be studied, molecular dynamics is applied.

A third approach lying between the previous two is also possible. It is at a mesoscale approach and deals with the motion of a larger number of particles. This method is called kinetic theory and is a branch of statistical mechanics, which describes the evolution of transport phenomena in dilute gases even far from equilibrium. The degree of non-equilibrium depends on the differences between density, temperature and velocity of particles inside the gas. The approach to equilibrium is achieved with the transport processes (mass, momentum and energy) that take place inside the gas. The target of kinetic theory is through admissions and assumptions to describe phenomena in a gas from a molecular point of view which are also valid in the macroscopic scale. Therefore, through kinetic theory it is possible to extract data for the transport coefficients, but also to study their interaction. Mathematically, kinetic theory is described by a distribution function which contains information on the distribution of molecules and of their velocities on a given system which depends on time.

An important dimensionless number in kinetic theory is the Knudsen number Kn or it's inversely proportional rarefaction parameter δ. The Knudsen number expresses the average distance traveled by a molecule between two successive collisions, known as the mean free path (MFP) divided by a characteristic length scale of the configuration, e.g. the diameter in a tube. The Knudsen number may be written as

$$Kn = \frac{\lambda}{L_c} \approx \frac{1}{\delta}. \tag{1.1}$$

By defining the Knudsen number, a classification of the state of the gas regarding the density can be made, i.e. how rarefied is the gas. For high values of Knudsen number, or low values of rarefaction parameter, respectively, the rarefaction of the gas is more pronounced. On the reverse case the gas tends to a continuum medium. Generally, four regimes of gas rarefaction are distinguished.

- Hydrodynamic regime ($Kn \to 0\ or\ \delta \to \infty$): The MFP is much smaller than the characteristic length ($\lambda \ll L_c$) and the interactions between the molecules are high and constant. In this regime the continuum mechanics equations can be applied (e.g. Navier-Stokes).
- Slip flow regime ($10^{-2} < Kn < 10^{-1}\ or\ 10 < \delta < 10^2$): Here the nonslip velocity and temperature continuity on the surface stops to apply and new boundary conditions must be used, that of the velocity slip and temperature jump. The continuous mechanics equations can still be applied.
- Transition regime ($10^{-1} < Kn < 10\ or\ 10^{-1} < \delta < 10$): In this regime the continuous mechanics equations are no longer applicable and the BE is employed.
- Free molecular regime ($Kn \to \infty\ or\ \delta \to 0$): The MFP is way bigger than the characteristic length ($\lambda \gg L_c$) and no collisions occur between the molecules, that's why it is also called collisionless regime. The flow is affected only by the interaction between gas and surface.

It is noted that the BE is valid in the whole range of gas rarefaction, and its application is limited to the late slip, transition and free molecular regimes due to the high computational cost and complexity associated with its solution.

1.2 Historic Review

Kinetic theory originated when Maxwell formulated the statistical approach of gases, meaning that their particles are moving independently and randomly, while the previous notion, that all particles have the same velocity, was abandoned. Later he introduced the velocity distribution function for a uniform a gas in equilibrium, the Maxwell distribution eq. (1.2).

$$f^M = \frac{N}{(2\pi RT)^{3/2}} \exp\left[-\frac{(\tilde{\boldsymbol{\xi}} - \tilde{\boldsymbol{u}})^2}{2RT}\right] \tag{1.2}$$

where $\tilde{\boldsymbol{\xi}}$ is the molecular velocity, $\tilde{\boldsymbol{u}}$ the hydrodynamic velocity, N the number of particles per cubic meter, R the gas constant and T the temperature.

Boltzmann on his turn derived an integro-differential equation, (1.3), in order to describe the evolution of the VDF and the approach to equilibrium for dilute gases. This equation was named after him (Boltzmann's Equation) and proved that Maxwell's distribution can be extracted from the solution of the BE. The basic assumptions of the BE are that only pairs of molecules can react at the same time and the molecular chaos assumption (Stosszahlansatz) introduced by Maxwell, i.e. the velocities of colliding molecules are uncorrelated. The former assumption limits the application of the equation only in gases with low density, e.g. dilute gases, while the latter defines the expected number of collisions between molecules and renders the equation irreversible in time.

$$\left(\frac{\partial}{\partial t} + \tilde{\boldsymbol{\xi}}_{\mathbf{1}} \cdot \nabla_r + \tilde{\boldsymbol{F}} \cdot \nabla_{\xi_1}\right) f_1 = \iiint (f_1' f_2' - f_1 f_2) g b db d\varphi d\tilde{\boldsymbol{\xi}}_{\mathbf{2}} \tag{1.3}$$

where $\tilde{\boldsymbol{\xi}}_{\mathbf{1}}, \tilde{\boldsymbol{\xi}}_{\mathbf{2}}$ are the molecular velocities before the collision, ∇_r, ∇_{ξ_1} are the gradient operators with respect to r , ξ_1, $\tilde{\boldsymbol{F}}$ is the external force per unit mass applied on the molecules, f_1, f_2 & $f_1' f_2'$ are distribution functions before and after collision respectively, $g = \left|\tilde{\boldsymbol{\xi}}_{\mathbf{2}} - \tilde{\boldsymbol{\xi}}_{\mathbf{1}}\right|$ is the relative velocity before the collision, b is the impact parameter, i.e. the distance between the asymptotes of a molecule at rest and another at a trajectory and φ is the azimuthal angle specifying the position of a plane in space.

Another important achievement of Boltzmann was the extraction of the H-theorem (or E-theorem from entropy, as he called it) using the BE. The H-theorem proves that kinetic theory describes a process which is irreversible in time and that the molecular collisions tend to increase the entropy. A consequence of the irreversibility as time tends to infinity is that the VDF describing the gas will either change indefinitely or it will reach a limiting function, i.e.

in equilibrium. Proving the increase of entropy, the H-theorem can be compared to the 2nd thermodynamic law, though its use is more general since it is also valid far from equilibrium, but only for dilute gases. The relation connecting the quantity H with entropy (S) is

$$S = -k_B H_M + c \tag{1.4}$$

where S is the entropy, H_M the H-function, k_B the Boltzmann's constant and c a constant reflecting the arbitrariness of the zero point of entropy.

1.3 Kinetic Models

Boltzmann's equation has a wide spectrum of applications in rarefied gas dynamics. Due to the complicated collision integral (1.5) at the right hand side of the BE, its solution is a daunting and computationally intensive task. In some cases the non-linearity is necessary for the proper description of the problem, e.g. computing of the flow field of the entry of a body from space, because of the formation of shock waves due to hypersonic speeds. Yet in other cases, like gas flow on long capillaries, the BE can be linearized. To facilitate the solution of rarefied gas dynamics problems several different methods have been deployed with the most prominent being the deterministic solution of the kinetic model equations and the stochastic Direct Simulation Monte Carlo Method (DSMC). In the first method, through the kinetic models, the collision integral in BE is replaced by collision model, $J(f)$, which contains the essential information of the former. In the latter method (DSMC), the BE is solved in a stochastic manner. The collision terms of the various models must satisfy some of the properties of the collision term of the BE given by

$$Q(f,f) = \iiint (f_1' f_2' - f_1 f_2) g b db d\varphi d\tilde{\boldsymbol{\xi}}_2 \tag{1.5}$$

The properties that must be satisfied are the following:

i. Collision invariants:

$$\int \psi(\xi) J(f) d\tilde{\boldsymbol{\xi}} = 0, \tag{1.6}$$

where $\psi(\xi) = 1, m\tilde{\xi}, m\frac{\xi^2}{2}$

ii. H-theorem:

$$\int log\, f\, J(f)\, d\tilde{\boldsymbol{\xi}} \leq 0 \tag{1.7}$$

iii. Correct expressions for the transport coefficients.

Many kinetic models have been derived over the years, considering the area of study, e.g. monatomic or polyatomic gas, shock waves and more. The first model that was formed and the most known is the BGK model which has a wide range of applications. The BGK model assumes that collisions change f by an amount which is proportional to the departure of f from a the local Maxwellian distribution. The collision term of the BGK model is given by

$$J_{BGK}(f) = v(f^M - f) \tag{1.8}$$

where v is the collision frequency and it is chosen so BGK's solution provides the correct expression of the transport coefficients.

Another model that has been formulated is the Shakhov (S) model, given by

$$J_S(f) = \frac{P}{\mu}(f^S - f) \tag{1.9}$$

where P is the pressure and f^S equals to

$$f^S = f^M\left(1 + 2\frac{(1-Pr)}{5}\frac{m}{N(k_BT)^2}\widetilde{\boldsymbol{Q}}\cdot(\tilde{\boldsymbol{\xi}} - \tilde{\boldsymbol{u}})\left(\frac{(\tilde{\boldsymbol{\xi}} - \tilde{\boldsymbol{u}})^2}{2RT} - \frac{5}{2}\right)\right) \tag{1.10}$$

Pr is the Prandtl number, $\widetilde{\boldsymbol{Q}}$ is the heat flux vector and f^M is the local Maxwellian distribution, (1.2). Compared to the BGK model the S model is more advanced, since it provides the correct expressions for viscosity and thermal conductivity at the same (this is not true for the BGK model). It, also, satisfies the collision invariants, but comes short regarding the fulfillment or not of the H-theorem. It is emphasized however, that the linearized Shakhov model, which is used in the present work does satisfy the H-theorem.

1.4 Gas-Surface Interaction

Modeling the interaction between a gas and a wall is of great importance in rarefied gas flows and special attention should be given in selecting the appropriate model. For an impermeable wall a particle with a given velocity $\tilde{\boldsymbol{\xi}}'$ that impacts it will be re-emitted with a velocity $\tilde{\boldsymbol{\xi}}$. The impinging molecules may scatter specularly, meaning that the molecules are reflected while maintaining their tangential velocity constant and changing sign on their normal velocity, or diffusely, i.e. the molecules may travel uniformly to any direction. A combination of diffuse and specular reflection is also possible while more complicated models also exist. A major factor that affects the scattering is the roughness of the surface,

while additional factors that concur in the reflection of the molecules are the wall temperature and velocity. In Fig. 1.1 a graphical view of diffuse and specular reflection is provided.

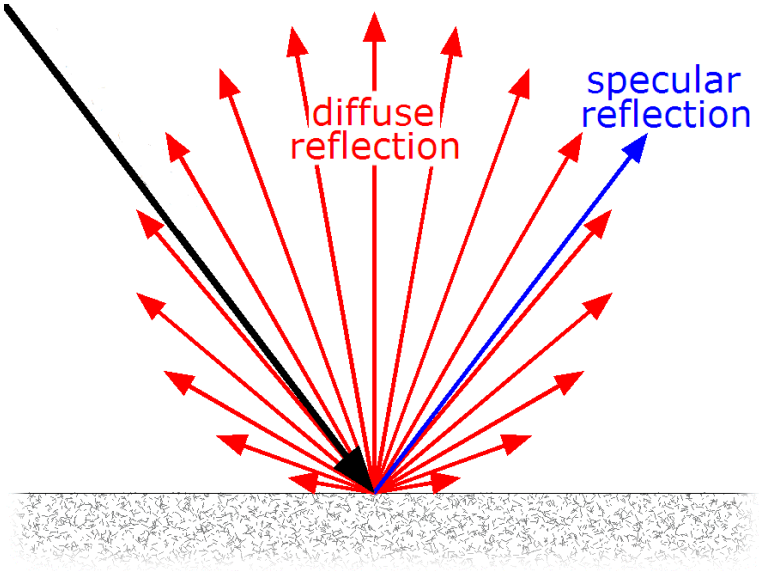

Figure 1.1: Specular-Diffuse reflection

Gas-surface interaction is typically characterized using the scattering kernel $R(\tilde{\boldsymbol{\xi}}', \tilde{\boldsymbol{\xi}})$, which expresses the probability of an impinging particle with velocity $\tilde{\boldsymbol{\xi}}'$ to be re-emitted with velocity $\tilde{\boldsymbol{\xi}}$. If the number of particles with velocity $\tilde{\boldsymbol{\xi}}'$ in $d\tilde{\boldsymbol{\xi}}'$ that impact on the surface for a given area and time is multiplied by the scattering kernel and is integrated over the whole range of incident velocity $\tilde{\boldsymbol{\xi}}'$, then the returning particles with velocity $\tilde{\boldsymbol{\xi}}$ will be found

$$\tilde{\boldsymbol{\xi}} \cdot \tilde{\mathbf{n}}\, \mathrm{f}(\tilde{\boldsymbol{\xi}}) = -\int_{\tilde{\boldsymbol{\xi}}' \cdot \tilde{\mathbf{n}} \leq 0} \tilde{\boldsymbol{\xi}}' \cdot \tilde{\mathbf{n}}\, \mathrm{f}(\tilde{\boldsymbol{\xi}}') R(\tilde{\boldsymbol{\xi}}', \tilde{\boldsymbol{\xi}}) d\tilde{\boldsymbol{\xi}}' \tag{1.11}$$

where $\mathrm{f}(\tilde{\boldsymbol{\xi}}')$ and $\mathrm{f}(\tilde{\boldsymbol{\xi}})$ are the VDFs before and after the impinging, respectively and $\tilde{\mathbf{n}}$ is the unit normal vector towards the flow domain.

The scattering kernel satisfies the following properties. For example, since the scattering kernel is a probability density function it must be positive:

$$R(\tilde{\boldsymbol{\xi}}', \tilde{\boldsymbol{\xi}}) \geq 0. \tag{1.12}$$

Also, the sum of all probabilities must be equal to one:

$$\int_{\tilde{\boldsymbol{\xi}}\cdot\tilde{\mathbf{n}}\geq 0} R\left(\tilde{\boldsymbol{\xi}}', \tilde{\boldsymbol{\xi}}\right) d\tilde{\boldsymbol{\xi}} = 1. \tag{1.13}$$

Another important property is the reciprocity condition, which occurs due to the reversibility of microprocesses of the gas-surface interaction and is valid if a surface is in a local equilibrium, [17], given by

$$\tilde{\boldsymbol{\xi}}' \cdot \tilde{\mathbf{n}} \exp\left(-\frac{m\xi'^2}{2k_B T_w}\right) R\left(\tilde{\boldsymbol{\xi}}', \tilde{\boldsymbol{\xi}}\right) = -\tilde{\boldsymbol{\xi}} \cdot \tilde{\mathbf{n}} \exp\left(-\frac{m\xi^2}{2k_B T_w}\right) R\left(-\tilde{\boldsymbol{\xi}}, -\tilde{\boldsymbol{\xi}}'\right) \tag{1.14}$$

where $\tilde{\boldsymbol{\xi}}' \cdot \tilde{\mathbf{n}} \geq 0, \tilde{\boldsymbol{\xi}} \cdot \tilde{\mathbf{n}} \leq 0$.

Maxwell was the first one who formulated the scattering kernel for a diffuse and specular interaction between particles and surfaces given by

$$R_d\left(\tilde{\boldsymbol{\xi}}', \tilde{\boldsymbol{\xi}}\right) = \frac{2\tilde{\boldsymbol{\xi}} \cdot \tilde{\mathbf{n}}}{\pi(2RT_w)^2} \exp\left(-\frac{(\tilde{\boldsymbol{\xi}} - \tilde{\boldsymbol{u}}_w)^2}{2RT_w}\right), \tag{1.15}$$

$$R_s\left(\tilde{\boldsymbol{\xi}}', \tilde{\boldsymbol{\xi}}\right) = \delta\left(\tilde{\boldsymbol{\xi}}' - \tilde{\boldsymbol{\xi}} + 2(\tilde{\boldsymbol{\xi}} \cdot \tilde{\mathbf{n}})\tilde{\mathbf{n}}\right) \tag{1.16}$$

where R_d is the diffuse kernel, R_s the specular kernel, $\tilde{\boldsymbol{u}}_w$ is the wall velocity and δ(x) Dirac delta function. For a better and more thorough description of the interaction, since the particles are not emitted from the surface only specularly or diffusely, the linear combination of the two kernels is also used, creating the so-called Maxwell or diffuse-specular model and introduced the accommodation coefficient (AC) a^M, where $0 \leq a^M \leq 1$ denotes the percentage of particles emitted diffusively.

$$R_{ds}\left(\tilde{\boldsymbol{\xi}}', \tilde{\boldsymbol{\xi}}\right) = a^M R_d\left(\tilde{\boldsymbol{\xi}}', \tilde{\boldsymbol{\xi}}\right) + (1 - a^M) R_s\left(\tilde{\boldsymbol{\xi}}', \tilde{\boldsymbol{\xi}}\right) \tag{1.17}$$

The Maxwell model has a wide range of application until today, though sometimes it fails to describe successfully a problem, as different values of AC occur between the Poiseuille flow and the thermomolecular pressure difference (TPD) or between the free molecular and hydrodynamic regimes [26]. Also, the thermomolecular pressure ratio exponent γ always equals to $\gamma = 0.5$ in the free molecular regime, regardless the value of AC, while experiments have proven that a lower value is possible [25]. The reason behind this shortcoming is because the scattering kernel depends on a single free variable for the description of the gas-surface interaction, while a more complicated expression is needed.

Another, more recent, scattering kernel was introduced by Cercignani & Lampis (CL) in 1971, [11], which includes two accommodation coefficients. The CL kernel is given by

$$R(\tilde{\boldsymbol{\xi}}', \tilde{\boldsymbol{\xi}}) = \frac{m^2 \xi_n}{2\pi a_n a_t (2-a_t)(k_B T_w)^2} \exp\left\{ -\frac{m\left[{\xi_n}^2 + (1-a_n){\xi_n}'^2\right]}{2k_B T_w a_n} \right.$$
$$\left. - \frac{m[\xi_t - (1-a_t)\xi_t']^2}{2k_B T_w a_t (2-a_t)} \right\} I_0\left(\frac{\sqrt{1-a_n}\, m \xi_n {\xi_n}'}{a_n k_B T_w} \right) \tag{1.18}$$

where I_0 denotes the modified Bessel function of first kind and zeroth order

$$I_0(x) = \frac{1}{\pi} \int_0^{\pi} \exp(x \cos\varphi)\, d\varphi \tag{1.19}$$

${\xi_n}', \xi_t'$ are the normal and tangential components of the velocity. The physical meaning of parameter a_t is associated with the tangential momentum, while the parameter a_n is associated with the kinetic energy corresponding to the normal velocity. Therefore, they are called tangential momentum AC (TMAC) and normal energy AC (NEAC) respectively. The range of the former is $0 \leq a_t \leq 2$, while of the latter is $0 \leq a_n \leq 1$. When both accommodation coefficients are equal to unity ($a_t = a_n = 1$) the CL kernel converts to the diffuse one, while for the value of zero ($a_t = a_n = 0$) it converts to the specular kernel. Also, for the limiting values of $a_t = 2$ and $a_n = 0$ the peculiar case of back-scattering is described, a state that the diffuse-specular model cannot approach. In a real case scenario a complete back-scattering is not possible, but a partial is, for rough surfaces. Moreover, the CL model manages to recover the plume-like structure around the line of specular reflection in the experiment of thermal beam scattering and can successfully match the TPD between numerical and experimental measurements for values lower than 0.5. A shortcoming of the model is the prediction of a fixed value for the thermal slip coefficient.

Other models have been developed in an effort to surpass the weaknesses of the Maxwell kernel. For example, Epstein proposed a generalized scattering kernel, [19], which includes the dependence of the AC to the velocities of the impinging molecules. However, the Epstein model has also some shortcomings, such as its incapability of describing the back-scattering. To exploit the advantages and overcome the drawbacks of both Epstein and CL kernels a combined new BC was proposed by Wu and Struchtrup [18]. Additional models have been proposed by Klinc & Kuěčer, which later was extended by combining it with the Epstein model [20,21], by Lord who introduced an improvement to the CL model, [22]. Modeling of the gas-surface interaction still remains a field of further investigation.

1.5 Rarefied gas flows in long channels

The problem of a rarefied gas flow through capillaries of various lengths and cross sections is of great importance and many studies and experiments have been performed. More specifically, efforts are made in order to understand all the parameters and conditions that may affect the flow. The investigation includes linear or non-linear flows [4], various cross-sections (circular, rectangular, triangular) [5,9,10,23], short or long channels. In all cases the force may be driven by pressure or/and temperature gradients. The field has drawn so much attention because of the range and development of practical applications encountered in aerospace and engineering, vacuum technology and the emerging field of Micro-Electro-Mechanics-Systems (MEMS). This entire numerical and experimental works include the gas-surface interaction. Because of that, the identification of the accommodation coefficients, characterizing the gas-surface interaction, is important for the accurate modeling of rarefied gas flows. The developed databases concerning the computed overall quantities should always refer to the implemented gas-surface interaction model. Some major drawbacks, regarding not only the gas-surface interaction but all the involved parameters, is the introduction of assumptions and simplifications, which are need in order to solve the problem and therefore the results may be not easily compared with experiments.

1.6 Thesis objectives and structure

The main objective of the diploma thesis is to extract the accommodation coefficients characterizing the gas-surface interaction in specific flow configurations. To achieve this, the rarefied gas flow in a long rectangular duct is solved by applying the linearized Shakhov kinetic model along with the Maxwell or Cercignani-Lampis boundary conditions. Comparisons are performed between the numerical and experimental results and the accommodation coefficients are extracted such that the difference between the computed and measured flows rates is minimized.

The structure of the thesis is as follows: In Chapter 2. the flow configurations, governing equations along with the associated boundary conditions and the flow rate computation model are provided, along with a short description of the cited experimental setup. In Chapter 3, for both problems, extensive kinetic databases are built for the dimensionless flow rates in terms of the gas rarefaction parameter and the accommodation coefficients. In Chapters 4 and 5 the extraction of the accommodation coefficients for the

pressure and temperature driven flows respectively is provided. Finally, in Chapter 6 a brief summary with the main concluding remarks are stated.

Chapter 2 **KINETIC MODELING**

A detailed description of the pressure and temperature driven flow configurations along with the governing kinetic equations and the associated boundary conditions is provided. The computed overall dimensionless quantities, as well as the corresponding dimensional ones are defined. Finally, for completeness purposes a short description of the cited experimental flow setup is given.

2.1 Flow configuration

The problem of the fully developed flow of a rarefied gas through a long duct of rectangular cross-section, under steady conditions driven by pressure and temperature gradients is considered. The flow takes place through a long rectangular duct connected to two vessels, meaning that the length of the duct is much greater than its width and height. Thus, the end effects can be neglected and the pressure varies only in the axial direction, while it remains constant in every cross section. The flow may be due to a pressure or a temperature gradient. The first case is that of a pressure difference imposed at the two vessels. The vessel with the high pressure is the upstream vessel, while the vessel with the low pressure is the downstream one. It is assumed that the pressure at the two vessels is the same with the corresponding channel end. This is a Poiseuille type flow. The second case regards a temperature difference between the vessels and a linear variation of the temperature along the channel wall. Then, in rarefied gas dynamics, a flow is observed from the low towards the high temperature vessel. This is the so-called thermal creep flow. In both flow configurations it is considered that the cross section of the duct lies on the x-y plane and z-axis is parallel to the length of the channel.

2.2 Governing kinetic equations

Modeling is based on the Shakhov kinetic model because of its advantages over the BGK model that were cited in Chapter 1. The non-linear Shakhov model with no external force is described by the equation

$$\frac{\partial f}{\partial t} + \tilde{\boldsymbol{\xi}} \cdot \frac{\partial f}{\partial \tilde{\boldsymbol{r}}} = \frac{P}{\mu}(f^S - f) \tag{2.1}$$

Since the flow is steady-state the time derivative is zero and eq. (2.1) will become

$$\xi_x \frac{\partial f}{\partial x'} + \xi_y \frac{\partial f}{\partial y'} + \xi_z \frac{\partial f}{\partial z'} = \frac{P}{\mu}(f^S - f) \tag{2.2}$$

Next, the linearization of the Shakhov model for each problem is described.

2.2.1 Pressure driven flow

For extracting the linear model in a fully developed pressure driven flow a perturbed distribution is introduced as

$$f = f^0(1 + h(x, y, \tilde{\boldsymbol{\zeta}})x_P + x_P \frac{z'}{H}) \tag{2.3}$$

where $h(x, y, \tilde{\boldsymbol{\zeta}})$ is called perturbation function, $\|x_P\| = \left\|\frac{H}{P_0}\frac{dP}{dz'}\right\| < 1$ and f^0 is the absolute Maxwellian distribution,

$$f^0 = \frac{N_0}{(2\pi RT)^{3/2}}\ exp\left(-\frac{\xi^2}{2RT_0}\right) \tag{2.4}$$

Next the local Maxwellian is expanded in Taylor series keeping terms up to first order

$$f^M = f^0 + (N - N_0)\left.\frac{\partial f^M}{\partial N}\right|_0 + (\tilde{\boldsymbol{u}} - \tilde{\boldsymbol{u}}_{\boldsymbol{0}}) \cdot \left.\frac{\partial f^M}{\partial \tilde{\boldsymbol{u}}}\right|_0 + (T - T_0)\left.\frac{\partial f^M}{\partial T}\right|_0 \tag{2.5}$$

Following some manipulation it is deduced that

$$\begin{aligned} f^S = f^0 \Bigg[1 + \frac{N - N_0}{N_0} + \frac{2\tilde{\boldsymbol{\xi}} \cdot \tilde{\boldsymbol{u}}}{2RT_0} + \frac{T - T_0}{T_0}\left(\left(\frac{\xi}{\sqrt{2RT_0}}\right)^2 - \frac{3}{2}\right) \\ + \frac{2}{15}\frac{m}{N_0(k_B T)^2}\tilde{\boldsymbol{\xi}} \cdot \tilde{\boldsymbol{Q}}\left(\left(\frac{\xi}{\sqrt{2RT_0}}\right)^2 - \frac{5}{2}\right)\Bigg] \end{aligned} \tag{2.6}$$

To proceed, in the non-linear model the VDF is replaced by the perturbed distribution

$$\tilde{\boldsymbol{\xi}}\frac{\partial\left[f_0\left(1+hx_p+x_p\frac{z'}{H}\right)\right]}{\partial\tilde{\boldsymbol{r}}}=\frac{P}{\mu}\left(f^S-f^0\left(1+hx_p+x_p\frac{z'}{H}\right)\right) \tag{2.7}$$

After some mathematical manipulation the linearized Shakhov model equation is deduced:

$$\zeta_x\frac{\partial h}{\partial x}+\zeta_y\frac{\partial h}{\partial y}=\delta\left[2\zeta_z v_z+\frac{4}{15}\zeta_z q_z\left(\zeta^2-\frac{5}{2}\right)-h\right]-\zeta_z \tag{2.8}$$

where $\tilde{\boldsymbol{\zeta}}=\frac{\tilde{\boldsymbol{\xi}}}{v_0}, x=\frac{x'}{H},\ y=\frac{y'}{H}, q_z=\frac{Q_z}{v_0 P_0 x_p}, v_z=\frac{u_z}{v_0 x_p}$.

To continue, two projections are introduced which are going to help in the calculations for both the pressure and temperature driven flow. The first projected distribution function is defined as

$$\varphi=\frac{1}{\sqrt{\pi}}\int_{-\infty}^{+\infty}\zeta_z\, h e^{-{\zeta_z}^2}d\zeta_z \tag{2.9}$$

Operating accordingly in (2.8) it is deduced that

$$\zeta_x\frac{\partial\varphi_P}{\partial x}+\zeta_y\frac{\partial\varphi_P}{\partial y}=\delta\left[v_z+\frac{2}{15}q_z\left({\zeta_x}^2+{\zeta_y}^2-1\right)-\varphi_P\right]-\frac{1}{2} \tag{2.10}$$

where φ_P is the projection (2.8) referring to the pressure driven flow. The second projected distribution function is defined as

$$\psi=\frac{1}{\sqrt{\pi}}\int_{-\infty}^{+\infty}{\zeta_z}^3\, h e^{-{\zeta_z}^2}d\zeta_z \tag{2.11}$$

and operating accordingly in (2.8) it is deduced that

$$\zeta_x\frac{\partial\psi_P}{\partial x}+\zeta_y\frac{\partial\psi_P}{\partial y}=\delta\left[\frac{3}{2}v_z+\frac{1}{5}q_z\left({\zeta_x}^2+{\zeta_y}^2\right)-\psi_P\right]-\frac{3}{4} \tag{2.12}$$

where ψ_P is the projection (2.11) referring to the pressure driven flow The macroscopic velocity is given by

$$u_z=\frac{1}{N}\iiint_{-\infty}^{+\infty}\xi_z f d\tilde{\boldsymbol{\xi}} \tag{2.13}$$

The moments of the VDF are also linearized. More specifically, the bulk velocity becomes

$$u_z = \frac{1}{N}\iiint_{-\infty}^{+\infty} \xi_z f_0 \left(1 + hx_p + x_p \frac{z'}{H}\right) d\tilde{\boldsymbol{\xi}} = \frac{v_0 x_p}{\pi^{\frac{3}{2}}} \iiint_{-\infty}^{+\infty} \zeta_z \, he^{-\zeta^2} d\tilde{\zeta} \tag{2.14}$$

In addition, the dimensionless macroscopic velocity $v_{z,P}$ is introduced as

$$v_{z,P} = \frac{u_z}{v_0 x_p} = \frac{1}{\pi^{3/2}} \iiint_{-\infty}^{+\infty} \zeta_z \, he^{-\zeta^2} d\tilde{\zeta} = \frac{1}{\pi} \iint_{-\infty}^{+\infty} \varphi_P \, e^{-{\zeta_x}^2} e^{-{\zeta_y}^2} d\zeta_x d\zeta_y \tag{2.15}$$

Similarly, the heat flux given by

$$Q_z = \frac{m}{2} \iiint_{-\infty}^{+\infty} (\xi_z - u_z) \left(\tilde{\boldsymbol{\xi}} - \tilde{\boldsymbol{u}}\right)^2 f d\tilde{\boldsymbol{\xi}} \tag{2.16}$$

is linearized as

$$Q_z = \frac{m}{2} \iiint_{-\infty}^{+\infty} (\xi_z - u_z) \left(\tilde{\boldsymbol{\xi}} - \tilde{\boldsymbol{u}}\right)^2 f_0 (1 + hx_P + x_P) d\tilde{\boldsymbol{\xi}} \tag{2.17}$$

and non-dimensionalized as

$$Q_z = \frac{P_0 v_0 x_P}{\pi^{\frac{3}{2}}} \iiint_{-\infty}^{+\infty} \zeta_z \left(\zeta^2 - \frac{5}{2}\right) h \, exp(-\zeta^2) d\tilde{\boldsymbol{\zeta}} \tag{2.18}$$

The z-component of the dimensionless heat flux $q_{z,P}$ is given by

$$q_{z,P} = \frac{Q_z}{P_0 v_0 x_P} = \frac{1}{\pi^{\frac{3}{2}}} \iiint_{-\infty}^{+\infty} \zeta_z \left(\zeta^2 - \frac{5}{2}\right) h \, exp(-\zeta^2) d\tilde{\boldsymbol{\zeta}} \tag{2.19}$$

and in terms of the projected distributions as

$$q_{z,P} = \frac{1}{\pi} \iint_{-\infty}^{+\infty} \left[\psi_P + \left({\zeta_x}^2 + {\zeta_y}^2 - \frac{5}{2}\right) \varphi_P\right] exp\left(-{\zeta_x}^2 - {\zeta_y}^2\right) d\zeta_x d\zeta_y \tag{2.20}$$

2.2.2 Temperature driven flow

The linearized Shakhov model equation for the temperature driven flow is obtained in a similar manner as the for the pressure driven flow, using the same projections, using however a slightly different definition of the perturbed distribution given by

$$f = f_0\left[1 + hx_T + x_T\frac{z'}{H}\left(\frac{\xi^2}{2RT_0} - \frac{5}{2}\right)\right] \tag{2.21}$$

where $\|x_T\| = \left\|\frac{H}{T_0}\frac{dT}{dz'}\right\| < 1$

The linearized distribution functions are introduced in the non-linear model to yield

$$\tilde{\boldsymbol{\xi}}\frac{\partial\left[f_0\left(1 + hx_T + x_T\frac{z'}{H}\left(\frac{\xi^2}{2RT_0} - \frac{5}{2}\right)\right)\right]}{\partial\tilde{r}} = \frac{P}{\mu}\left\{f^S - f_0\left[1 + hx_T + x_T\frac{z'}{H}\left(\frac{\xi^2}{2RT_0} - \frac{5}{2}\right)\right]\right\} \tag{2.22}$$

$$\zeta_x\frac{\partial h}{\partial x} + \zeta_y\frac{\partial h}{\partial y} = \delta\left[2\zeta_z v_z + \frac{4}{15}\zeta_z q_z\left(\zeta^2 - \frac{5}{2}\right) - h\right] - \zeta_z\left(\zeta^2 - \frac{5}{2}\right) \tag{2.23}$$

Next the projections (2.9) & (2.11) are used in equation (2.23) to get the projected kinetic equations. For the projections (2.9) and (2.11) the final expressions are

$$\zeta_x\frac{\partial\varphi_T}{\partial x} + \zeta_y\frac{\partial\varphi_T}{\partial y} = \delta\left[v_z + \frac{2}{15}q_z\left({\zeta_x}^2 + {\zeta_y}^2 - 1\right) - \varphi_T\right] - \frac{1}{2}\left({\zeta_x}^2 + {\zeta_y}^2 - 1\right) \tag{2.24}$$

and

$$\zeta_x\frac{\partial\psi_T}{\partial x} + \zeta_y\frac{\partial\psi_T}{\partial y} = \delta\left[\frac{3}{2}v_z + \frac{1}{5}q_z\left({\zeta_x}^2 + {\zeta_y}^2\right) - \psi_T\right] - \frac{3}{4}\left({\zeta_x}^2 + {\zeta_y}^2\right) \tag{2.25}$$

respectively. Next, the macroscopic velocity and heat flux for the temperature driven flow are calculated. The macroscopic velocity is linearized as

$$u_z = \frac{1}{N}\iiint_{-\infty}^{+\infty}\xi_z f\,d\tilde{\boldsymbol{\xi}} = \frac{1}{N}\iiint_{-\infty}^{+\infty}\xi_z f_0\left(1 + hx_T + x_T\frac{z'}{H}\left(\frac{\xi^2}{2RT_0} - \frac{5}{2}\right)\right)d\tilde{\boldsymbol{\xi}} \tag{2.26}$$

and is non-dimensionalized as

$$v_{z,T} = \frac{u_z}{v_0 x_T} = \frac{1}{\pi}\iint_{-\infty}^{+\infty}\varphi_T\, e^{-{\zeta_x}^2}e^{-{\zeta_y}^2}d\zeta_x d\zeta_y \tag{2.27}$$

Similarly, the heat flux is linearized and non-dimensionalized as

$$Q_z = \frac{m}{2}\iiint_{-\infty}^{+\infty}(\xi_z - u_z)\left(\tilde{\boldsymbol{\xi}} - \tilde{\boldsymbol{u}}\right)^2 f_0\left(1 + hx_T + x_T\frac{z'}{H}\left(\frac{\xi^2}{2RT_0} - \frac{5}{2}\right)\right)d\tilde{\boldsymbol{\xi}} \qquad (2.28)$$

$$Q_z = \frac{P_0 v_0 x_T}{\pi^{\frac{3}{2}}}\iiint_{-\infty}^{+\infty}\zeta_z\left(\zeta^2 - \frac{5}{2}\right)h\,exp(-\zeta^2)d\tilde{\boldsymbol{\zeta}} \qquad (2.29)$$

$$q_{z,T} = \frac{Q_z}{P_0 v_0 x_T} = \frac{1}{\pi}\iint_{-\infty}^{+\infty}\left[\psi_T + \left({\zeta_x}^2 + {\zeta_y}^2 - \frac{5}{2}\right)\varphi_T\right]exp\left(-{\zeta_x}^2 - {\zeta_y}^2\right)d\zeta_x d\zeta_y \qquad (2.30)$$

As it seen the expressions of the dimensionless macroscopic velocity and heat flux are the same as for the pressure driven flow but of course the corresponding projected distributions functions are different. Therefore, the results for the macroscopic velocity and heat flux for the temperature driven flow will differ from the pressure driven since the linear models are defined for different perturbed distributions.

2.2.3 Overall Quantities

For the pressure and temperature driven flows the dimensionless flow rate and heat flow rate are given by

$$G_P = -2\frac{H}{W}\int_{-W/2H}^{W/2H}\int_{-1/2}^{1/2} v_{z,P}\,dxdy \qquad (2.31)$$

$$G_T = 2\frac{H}{W}\int_{-W/2H}^{W/2H}\int_{-1/2}^{1/2} v_{z,T}\,dxdy \qquad (2.32)$$

and the corresponding heat flow rates are given by

$$Q_P = 2\frac{H}{W}\int_{-W/2H}^{W/2H}\int_{-1/2}^{1/2} q_{z,P}\,dxdy \qquad (2.33)$$

$$Q_T = -2\frac{H}{W}\int_{-W/2H}^{W/2H}\int_{-1/2}^{1/2} q_{z,T}\,dxdy \qquad (2.34)$$

The kinetic coefficients G_P and Q_T are due to direct effects and more specifically they are the flow rate and the heat flow deduced due to the pressure and temperature difference, respectively. The kinetic coefficients G_T and Q_P are due to cross effects that approach zero as moving towards to the hydrodynamic regime. The first one is a flow rate due to a temperature difference, well known as the thermal creep flow rate and the second one is a heat flow due to a pressure difference well known as the mechanocaloric flux. It has been proved, [12-14], that G_T and Q_P obey the Onsager-Casimir relation for any scattering kernel that fulfills the reciprocity condition

$$G_T = Q_P \tag{2.35}$$

A more detailed presentation of the derivations is apposed on appendix A.

2.3 Boundary conditions

Two boundary condition models are considered, namely the Maxwell and the Cercignani-Lampis (CL). The Maxwell boundary conditions has only one accommodation coefficient, while the CL boundary conditions have two. Both have been implemented in order to have a thorough and complete study. It is necessary to linearize the boundary conditions and also perform the projection procedure in order to obtain expressions compatible to the deduced kinetic equations.

2.3.1 Maxwell boundary conditions

For the pressure driven flow, the perturbed distribution (2.3) is substituted in eq (1.11) to yield

$$\begin{aligned} |\xi_n| \frac{N_0}{(2\pi RT)^{\frac{3}{2}}} \, exp\left(-\frac{\xi^2}{2RT_0}\right)\left(1 + h(\tilde{\boldsymbol{\zeta}})x_P + x_P \frac{z'}{H}\right) = \int\limits_{\xi_n<0} \left|\xi_n{}'\right| R(\tilde{\boldsymbol{\xi}}' \\ \rightarrow \tilde{\boldsymbol{\xi}}) \frac{N_0}{(2\pi RT)^{3/2}} \, exp\left(-\frac{\xi'^2}{2RT_0}\right)(1 + h(\tilde{\boldsymbol{\zeta}}')x_P + x_P \frac{z'}{H}) d\tilde{\boldsymbol{\xi}}' \end{aligned} \tag{2.36}$$

The equation is split into two parts:

$$|\xi_n| \, exp\left(-\frac{\xi^2}{2RT_0}\right)(1 + x_P \frac{z'}{H}) = (1 + x_P \frac{z'}{H}) \int_{\xi_n<0} \left|\xi_n{}'\right| R(\tilde{\boldsymbol{\xi}}' \rightarrow \tilde{\boldsymbol{\xi}}) \, exp\left(-\frac{\xi'^2}{2RT_0}\right) d\tilde{\boldsymbol{\xi}}' \tag{2.37}$$

$$|\xi_n|\, exp\left(-\frac{\xi^2}{2RT_0}\right) h(\tilde{\boldsymbol{\zeta}}) = \int_{\xi_n<0} \left|\xi_n{}'\right| R(\tilde{\boldsymbol{\xi}}' \to \tilde{\boldsymbol{\xi}})\, h(\tilde{\boldsymbol{\zeta}}') exp\left(-\frac{\xi'^2}{2RT_0}\right) d\tilde{\boldsymbol{\xi}}' \qquad (2.38)$$

Using the reciprocity condition in (2.37) it is found that

$$|\xi_n|\, exp\left(-\frac{\xi^2}{2RT_0}\right) = \int\limits_{\xi_n'<0} |\xi_n|\, R(-\tilde{\boldsymbol{\xi}} \to -\tilde{\boldsymbol{\xi}}')\, exp\left(-\frac{\xi^2}{2RT_0}\right) d\tilde{\boldsymbol{\xi}}' \Rightarrow \qquad (2.39)$$

$$\Rightarrow 1 = \int\limits_{\xi_n'<0} R\left(-\tilde{\boldsymbol{\xi}} \to -\tilde{\boldsymbol{\xi}}'\right)\, d\tilde{\boldsymbol{\xi}}' \Rightarrow \qquad (2.40)$$

$$\Rightarrow 1 = \int\limits_{\xi_n'<0} R(\tilde{\boldsymbol{\xi}}' \to \tilde{\boldsymbol{\xi}})\, d\left(-\tilde{\xi}\right) = \int\limits_{\xi_n'>0} R(\tilde{\boldsymbol{\xi}}' \to \tilde{\boldsymbol{\xi}})\, d\left(\tilde{\boldsymbol{\xi}}\right) \qquad (2.41)$$

which is the normalization condition, (1.13). Next for the second part (2.38) it is seen that

$$|\xi_n|\, exp\left(-\frac{\xi^2}{2RT_0}\right) h(\tilde{\boldsymbol{\zeta}}) = \int\limits_{\xi_n<0} \left|\xi_n{}'\right| R(\tilde{\boldsymbol{\xi}}' \to \tilde{\boldsymbol{\xi}})\, exp\left(-\frac{\xi'^2}{2RT_0}\right) h(\tilde{\boldsymbol{\zeta}}') d\tilde{\boldsymbol{\xi}}' \qquad (2.42)$$

Substituting $R(\tilde{\boldsymbol{\xi}}' \to \tilde{\boldsymbol{\xi}})$ with the Maxwell kernel results to

$$h(\tilde{\boldsymbol{\zeta}}) = \frac{1}{|\xi_n|} \int\limits_{\xi_n<0} \left|\xi_n{}'\right| \left[a^M R_d(\tilde{\boldsymbol{\xi}}', \tilde{\boldsymbol{\xi}}) + (1-a^M) R_s(\tilde{\boldsymbol{\xi}}', \tilde{\boldsymbol{\xi}})\right] exp\left(\frac{\xi^2 - \xi'^2}{2RT_0}\right) h(\tilde{\boldsymbol{\zeta}}') d\tilde{\boldsymbol{\xi}}' \qquad 2.43)$$

$$h(\tilde{\boldsymbol{\zeta}}) = \frac{a^M}{|\xi_n|} \int\limits_{\xi_n<0} \left|\xi_n{}'\right| \frac{2\xi_n}{\pi(2RT_w)^2} \exp\left(\frac{\xi^2 - \xi^2 - \xi'^2}{2RT_w}\right) h(\tilde{\boldsymbol{\zeta}}') d\tilde{\boldsymbol{\xi}}' +$$

$$+ \frac{1-a^M}{|\xi_n|} \int\limits_{\xi_n<0} \left|\xi_n{}'\right| \delta(\tilde{\boldsymbol{\xi}}' - \tilde{\boldsymbol{\xi}} + \mathbf{2}(\tilde{\boldsymbol{\xi}} \cdot \tilde{\mathbf{n}})\tilde{\mathbf{n}}) exp\left(\frac{\xi^2 - \xi'^2}{2RT_0}\right) h(\tilde{\boldsymbol{\zeta}}') d\tilde{\boldsymbol{\xi}}' \qquad (2.44)$$

$$h(\tilde{\boldsymbol{\zeta}}) = a^M \int\limits_{\xi_n<0} \frac{2\left|\xi_n{}'\right|}{\pi(2RT_w)^2}\, exp\left(-\frac{\xi'^2}{2RT_0}\right) h(\tilde{\boldsymbol{\zeta}}') d\tilde{\boldsymbol{\xi}}' + (1-a^M) h(\tilde{\boldsymbol{\zeta}}' - \mathbf{2}(\tilde{\boldsymbol{\zeta}}' \cdot \tilde{\mathbf{n}})\tilde{\mathbf{n}}) \qquad (2.25)$$

$$h(\tilde{\boldsymbol{\zeta}}) = \int_{\zeta_n<0} R_{ds}(-\tilde{\boldsymbol{\zeta}} \to -\tilde{\boldsymbol{\zeta}}')\, h(\tilde{\boldsymbol{\zeta}}')\, d\tilde{\boldsymbol{\zeta}}' \tag{2.46}$$

Equation (2.46) can be rewritten as

$$h^+ = Ah^- \tag{2.47}$$

which is the sort form of linearized eq. (1.11)

Next step is to introduce the projections (2.9) & (2.11) respectively and to solve for the walls of the duct. The procedure is presented only for the x-axis as the same steps are followed in y-axis, too.

Projection φ:

$$\phi^+\left(\pm\frac{1}{2}, y, \zeta_x, \zeta_y\right) = \frac{1}{\sqrt{\pi}} \int_{-\infty}^{+\infty} Ah^-\zeta_z \exp(-\zeta_z^2)\, d\zeta_z = \tag{2.48}$$

$$= \frac{1}{\sqrt{\pi}} \int_{-\infty}^{+\infty} \left[\iiint_{\zeta_n'<0} R_{ds}\left(-\tilde{\zeta} \to -\tilde{\zeta}'\right) h^-\left(\tilde{\boldsymbol{\zeta}}'\right) d\tilde{\boldsymbol{\zeta}}' \right] \zeta_z \exp(-\zeta_z^2)\, d\zeta_z = \tag{2.49}$$

$$= \frac{1}{\sqrt{\pi}} \iiint_{\zeta_n'<0} \left[\int_{-\infty}^{+\infty} R_{ds}\left(-\tilde{\boldsymbol{\zeta}} \to -\tilde{\boldsymbol{\zeta}}'\right) \zeta_z \exp(-\zeta_z^2) d\zeta_z \right] h^-\left(\tilde{\boldsymbol{\zeta}}'\right) d\tilde{\boldsymbol{\zeta}}' = \tag{2.50}$$

$$= \frac{1-a^M}{\sqrt{\pi}} \iiint_{\zeta_n'<0} \zeta_z{}' \exp\left(-\zeta_z'^2\right) h^-\left(\tilde{\boldsymbol{\zeta}}'\right) d\tilde{\boldsymbol{\zeta}}' \tag{2.51}$$

$$\phi^+\left(\pm\frac{1}{2}, y, \zeta_x, \zeta_y\right) = (1-a^M)\phi^-\left(\pm\frac{1}{2}, y, \zeta_x, \zeta_y\right) \tag{2.52}$$

Projection ψ:

$$\psi^+\left(\pm\frac{1}{2}, y, \zeta_x, \zeta_y\right) = \frac{1}{\sqrt{\pi}} \int Ah^-\zeta_z{}^3 \exp(-\zeta_z^2)\, d\zeta_z = \tag{2.53}$$

$$= \frac{1}{\sqrt{\pi}} \int \left[\iiint_{\zeta_n'<0} R_{ds}\left(-\tilde{\boldsymbol{\zeta}} \to -\tilde{\boldsymbol{\zeta}}'\right) h^-\left(\tilde{\zeta}'\right) d\tilde{\zeta}' \right] \zeta_z{}^3 \exp(-\zeta_z^2)\, d\zeta_z = \tag{2.54}$$

$$= \frac{1}{\sqrt{\pi}} \iiint_{\zeta_n' < 0} \left[\int R_{ds}(-\tilde{\boldsymbol{\zeta}} \to -\tilde{\boldsymbol{\zeta}}') {\zeta_z}^3 \exp(-\zeta_z^2) d\zeta_z \right] h^-(\tilde{\boldsymbol{\zeta}}') d\tilde{\boldsymbol{\zeta}}' = \tag{2.55}$$

$$= \frac{1 - a^M}{\sqrt{\pi}} \iiint_{\zeta_n' < 0} {\zeta_z}^3 \exp(-\zeta_z^2)\, h^-(\tilde{\boldsymbol{\zeta}}') d\tilde{\boldsymbol{\zeta}}' = \tag{2.56}$$

$$\psi^+\left(\pm\frac{1}{2}, y, \zeta_x, \zeta_y\right) = (1 - a^M)\psi^-\left(\pm\frac{1}{2}, y, \zeta_x, \zeta_y\right) \tag{2.57}$$

2.3.2 Cercignani-Lampis boundary conditions

Regarding the CL boundary conditions the same process is followed to linearize eq. (1.11), but now in eq. (2.38) the CL kernel is substituted and will result to

$$h(\tilde{\boldsymbol{\zeta}}) = \frac{1}{|\xi_n|} \int_{\zeta_n < 0} |{\xi_n}'| \frac{2\zeta_n}{\pi a_n a_t (2 - a_t)} \exp\left[\frac{{\zeta_n}^2 + (1 - a_n){\zeta_n}'^2}{a_n} - \frac{(\zeta_t - (1 - a_t){\zeta_t}')^2}{a_t(2 - a_t)} \right] \times$$
$$I_0\left(\frac{2\sqrt{1 - a_n}\zeta_n {\zeta_n}'}{a_n} \right) exp\left(\zeta^2 - {\zeta'}^2\right) h(\tilde{\boldsymbol{\zeta}}')\, d\tilde{\boldsymbol{\zeta}}' \tag{2.58}$$

$$h(\tilde{\boldsymbol{\zeta}}) = \int_{\zeta_n < 0} \frac{2{\zeta_n}'}{\pi a_n a_t (2 - a_t)} \exp\left[-\frac{{\zeta_n}'^2 + (1 - a_n){\zeta_n}^2}{a_n} \right.$$
$$\left. - \frac{({\zeta_t}' - (1 - a_t)\zeta_t)^2}{a_t(2 - a_t)} \right] I_0\left(\frac{2\sqrt{1 - a_n}\zeta_n {\zeta_n}'}{a_n} \right) h(\tilde{\boldsymbol{\zeta}}')\, d\tilde{\boldsymbol{\zeta}}' \tag{2.59}$$

which may be rewritten as

$$h(\tilde{\boldsymbol{\zeta}}) = \int_{\zeta_n < 0} R_{CL}(-\tilde{\boldsymbol{\zeta}} \to -\tilde{\boldsymbol{\zeta}}')\, h(\tilde{\boldsymbol{\zeta}}')\, d\tilde{\boldsymbol{\zeta}}' \tag{2.60}$$

Again, the projections φ, ψ are used to produce the equations for the boundary conditions. Projection φ:

$$\phi^+\left(\pm\frac{1}{2},y,\zeta_x,\zeta_y\right)=\frac{1}{\sqrt{\pi}}\int_{-\infty}^{+\infty}Ah^-\zeta_z\exp(-\zeta_z^2)\,d\zeta_z= \tag{2.61}$$

$$=\frac{1}{\sqrt{\pi}}\int_{-\infty}^{+\infty}\left[\iiint_{\zeta_n'<0}R_{CL}\left(-\tilde{\zeta}\to-\tilde{\zeta}'\right)h^-\left(\tilde{\boldsymbol{\zeta}}'\right)d\tilde{\boldsymbol{\zeta}}'\right]\zeta_z\exp(-\zeta_z^2)\,d\zeta_z= \tag{2.62}$$

$$=\frac{1}{\sqrt{\pi}}\iiint_{\zeta_n'<0}\left[\int_{-\infty}^{+\infty}R_{CL}\left(-\tilde{\boldsymbol{\zeta}}\to-\tilde{\boldsymbol{\zeta}}'\right)\zeta_z\exp(-\zeta_z^2)d\zeta_z\right]h^-\left(\tilde{\boldsymbol{\zeta}}'\right)d\tilde{\boldsymbol{\zeta}}' \tag{2.63}$$

$$=\frac{a}{\sqrt{\pi}}\iiint_{\zeta_n'<0}R_n(-\zeta_n\to-\zeta_n')R_y\left(-\zeta_y\to-\zeta_y'\right)\zeta_z'\exp\left(-\zeta_z'^2\right)h^-\left(\tilde{\boldsymbol{\zeta}}'\right)d\tilde{\boldsymbol{\zeta}}' \tag{2.64}$$

where $a=1-a_t$

$$\begin{aligned}&\phi^+\left(\pm\frac{1}{2},y,\zeta_x,\zeta_y\right)=\\&=\frac{2(1-a_t)}{a_n\sqrt{\pi a_t(2-a_t)}}\iint_{\zeta_n'<0}\phi^-\left(\pm\frac{1}{2},y,\zeta_x',\zeta_y'\right)\zeta_z'\exp\left[-\frac{\zeta_z'^2+(1-a_n)\zeta_n'^2}{a_n}\right.\\&\left.-\frac{\left((1-a_t)\zeta_y-\zeta_y'\right)^2}{a_t(2-a_t)}\right]I_0\left(\frac{2\sqrt{1-a_n}\zeta_n\zeta_n'}{a_n}\right)d\zeta_n'd\zeta_y'\end{aligned} \tag{2.65}$$

Projection ψ:

$$\psi^+\left(\pm\frac{1}{2},y,\zeta_x,\zeta_y\right)=\frac{1}{\sqrt{\pi}}\int Ah^-\zeta_z^{\,3}\exp(-\zeta_z^2)\,d\zeta_z= \tag{2.66}$$

$$=\frac{1}{\sqrt{\pi}}\int\left[\iiint_{\zeta_n'<0}R_{CL}\left(-\tilde{\boldsymbol{\zeta}}\to-\tilde{\boldsymbol{\zeta}}'\right)h^-\left(\tilde{\zeta}'\right)d\tilde{\zeta}'\right]\zeta_z^{\,3}\exp(-\zeta_z^2)\,d\zeta_z= \tag{2.67}$$

$$=\frac{1}{\sqrt{\pi}}\iiint_{\zeta_n'<0}\left[\int R_{CL}\left(-\tilde{\boldsymbol{\zeta}}\to-\tilde{\boldsymbol{\zeta}}'\right)\zeta_z^{\,3}\exp(-\zeta_z^2)d\zeta_z\right]h^-\left(\tilde{\boldsymbol{\zeta}}'\right)d\tilde{\boldsymbol{\zeta}}'= \tag{2.68}$$

$$= \frac{1}{\sqrt{\pi}} \iiint\limits_{\zeta_n'<0} R_n(-\zeta_n \to -\zeta_n')R_y(-\zeta_y \to -\zeta_y') \left[\zeta_z'^3 \exp(-\zeta_z'^2)\, a^3 + \zeta_z' \exp(-\zeta_z'^2) \frac{3}{2}\alpha(1-\alpha^2)\right] h^-(\tilde{\boldsymbol{\zeta}}')d\tilde{\boldsymbol{\zeta}}' \tag{2.69}$$

$$\psi^+ = \frac{(1-a_t)^3}{\sqrt{\pi}} \iint\limits_{\zeta_n'<0} R_n(-\zeta_n \to -\zeta_n')R_y(-\zeta_y \to -\zeta_y')\ \psi^-\left(\pm\frac{1}{2}, y, \zeta_x, \zeta_y\right) d\zeta_n' d\zeta_y' + \tag{2.70}$$

$$+ \frac{3a_t(1-a_t)}{2}\frac{(2-a_t)}{\sqrt{\pi}} \iint\limits_{\zeta_n'<0} R_n(-\zeta_n \to -\zeta_n')R_y(-\zeta_y \to -\zeta_y')\ \varphi^-\left(\pm\frac{1}{2}, y, \zeta_x, \zeta_y\right) d\zeta_n' d\zeta_y'$$

Concerning the temperature driven flow, by substituting the perturbed distribution (2.21) in (1.11), the linearized form will have the same form as eqs. (2.46) and (2.60). So, it is easy seen that when the perturbed function will be replaced in the projections φ & ψ the results will be the ones that have already been computed for both boundary conditions, eqs. (2.52), (2.57), (2.65) and (2.70). A more thorough description resulting in the linearized equations is presented in Appendix B.

2.4 Computation of mass flow rate

The numerical model was built in order to provide the dimensionless mass flow rates and heat fluxes. Although only the kinetic coefficients G_P and G_T were necessary since the comparison of the numerical with the experimental results concerns the mass flow rates as it will be discussed later. The kinetic coefficients depend on the aspect ratio *H/W*, rarefaction parameter δ and accommodation coefficients, i.e. $G_P(H/W, \delta, a_t, a_n)$, or in the case of Maxwell boundary conditions $G_P(H/W, \delta, a^M)$. Since the purpose of the diploma thesis is to match the experimental and numerical mass flow rates, it is obvious that the aspect ratio for the numerical model should be equal to the experimental one, i.e. only one ratio is needed. Thus, the desired kinetic coefficients were extracted for a wide range of δ, a_t and a_n values for CL boundary conditions, as well as for δ and a^M for Maxwell boundary conditions. The reason the non-dimensionalization is preferred, is because it gives the opportunity of forming

a database that later can be used for analyzing different gases, on different ducts regarding the dimensions and for different conditions, e.g. temperature.

In order to evaluate the net mass flow rate from the kinetic coefficients, the assumption of the fully developed flow, i.e. the pressure is constant on each cross section and only varies through the length, may be made since $H \ll L$. The fully developed flow in a duct is calculated by the first order ordinary differential equation.

$$\frac{dP}{dz} = -\frac{v_0(z)}{WH^2 G_P(\delta(z), a_t, a_n)}\dot{m} + \frac{G_T(\delta(z), a_t, a_n)}{G_P(\delta(z), a_t, a_n)}\frac{P(z)}{T(z)}\frac{dT}{dz} \qquad 2.71)$$

The above expression is only valid for CL boundary conditions. In case of Maxwell BCs the coefficients G_P and G_T are functions of δ and a^M. Regarding the aspect of the given problem eq. (2.71) can be used to calculate the mass flow rate, if the pressure on both ends is known. The solution of the equation requires an iterative process where an initial value for the mass flow is assumed. Equation (2.71) is integrated with initial condition the pressure on the one end, for simplicity is called $P(0)$ where $z \in [0, L]$, and the computed pressure is compared with the pressure on the other, $P(L)$. Then the mass flow is recalculated and the process is repeated until convergence is achieved. For the pressure driven flow the pressure on the two ends of the channel is different and the temperature throughout the channel is constant so the temperature gradient on the right hand side of (2.71) becomes zero and it can be rewritten as,

$$\frac{dP}{dz} = -\frac{v_0(z)}{WH^2 G_P(\delta(z), a_t, a_n)}\dot{m} \qquad 2.72)$$

For a temperature driven flow the pressure on both ends is equal but there is a pressure variation along the channel. In addition, the temperature varies linearly along the channel.

2.5 Experiment description

The experimental results which have been used in the present work have been kindly provided by the research group at the University of D'Aix-Marseille and are included in the Ph.D. thesis of Dr. R. Brancher [1]. It is useful, mainly for completeness purposes, to provide a brief description of the experimental setup. The experiment took place for four different monatomic gases (He, Ne, Ar, Kr) and Nitrogen and separately for pressure and temperature flows. The apparatus where the experiments were held consisted of two tanks connected with the micro-channel and due to their small volume, when needed, an additional reservoir was connected to each tank. The reservoirs were of the same volume but different for the pressure

and temperature gradient flows. Also, a secondary line linked the two tanks with a vacuum pump and the high-pressure gas bottles. Finally, valves were placed in the apparatus in order to control the flow of the gas. The material of the micro-channel was PEEK (PolyEtherEtherKetone), its dimensions: height $H = 0.24 \pm 0.01mm$, width $W = 1.0mm$, length $L = 72mm$ and the measured roughness: $113 \pm 19nm$. For the estimation of the mass flow two pressure gauges were attached, one on each tank. During the pressure gradient experiment there was no influence on the temperature of the gas and so room temperature (T=293.15K) was assumed. For the temperature gradient experiment an electrical heater was connected to one tank and water cooling to the other. It is noted that only the tank on the hot side was heated and not the reservoir, which is of greater volume. Because of that some discrepancies on the imposed temperatures may be expected. The measurement of the temperature was monitored with thermocouples and an infra-red camera. The temperature differences that were tested were two, namely ΔT=58K (T_{hot}=342.65K, T_{cold}=284.65K) and ΔT=67.5K (T_{hot}=352.15K, T_{cold}=284.65K).

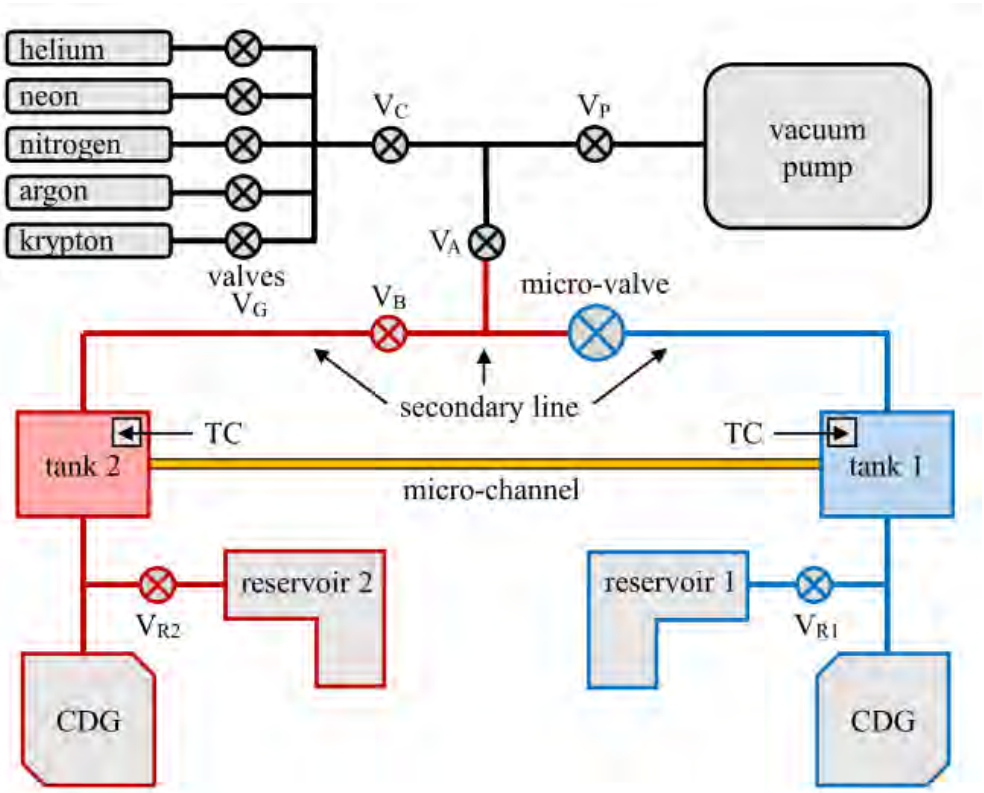

Figure 2.1: Experimental apparatus of [1]

Chapter 3 **KINETIC COEFFICIENTS**

Extensive tabulated results are provided for the dimensionless flow rates G_P and G_T in terms of the gas rarefaction parameters and the accommodation coefficients of the Maxwell and CL boundary conditions. The results are for the pressure and temperature gradient driven flows and for two aspect ratios of the rectangular cross section of the channel. More importantly, they are provided in the whole range of the involved parameters. These results are used in Chapters 4 and 5 to compute the corresponding mass flow rates and may be used as a reference point in future work. In addition, some validation of the implemented kinetic code is provided. The bulk of the computational work was performed on the Marconi supercomputer of the computing center CINECA.

3.1 Discretization and numerical parameters

Before gathering the data from the numerical model that would be later used for the evaluation of the mass flow rates it was requisite to check the mesh independence on the results, i.e. the percentage difference between the results for different discretization on molecular speed magnitudes and polar angles and physical space discretization intervals. The parameters during the tests were fixed at: *H/W=1, 0.24,* $\delta=10$, $a_t=a_n=0.75$. In the molecular velocity space the concluded discretization was: 40 magnitudes distributed according to Legendre polynomial roots, 200 polar angles equal distributed in $[0,2\pi]$ and in the physical space 50 intervals on both x and y axis. As can be seen from Tables 3.1 and 3.2 an increase on the polar angles or the intervals compared to the chosen ones, would result in a significant increase on solution time, but not on a notable difference between the kinetic coefficients. In the square channel *H/W=1* the number of nodes in x and y directions is the same, while in the rectangular one *H/W=0.24* varies according to the aspect ratio. This discretization was used for $\delta \leq 10$. Greater values of the gas rarefaction parameter imply the increase of the intermolecular collisions as the system tends to the hydrodynamic regime. In these cases a denser grid was applied in the physical space with a reduction to the polar angles (intervals x-axis=400, y-axis=200, polar angles=100). Furthermore, to prove the validity of the numerical

model the results were compared with other published results [4,9,10,15,16]. The gathered data refer to many aspect ratios for values of $\delta \in [0,50]$ and a wide range of values for the accommodation coefficients.

Table 3.1: Flow rates with various number of molecular velocities and physical nodes for H/W=1 and δ=10.

Velocities	Angles	X nodes	Y nodes	G_P	G_P Diff [%]	Time [hr]
40	100	101	101	1.6327	-0.110	6
40	200	101	101	1.6347	0.012	29
40	400	51	51	1.6354	0.058	58
40	200	51	51	1.6345		8

Table 3.2: Flow rates with various number of molecular velocities and physical nodes for H/W=0.24 and d=10.

Velocities	Angles	X nodes	Y nodes	G_P	G_P Diff [%]	Time [hr]
40	200	201	51	2.8952	3.454E-05	67
40	200	101	51	2.8952		41

It is noted that the computational times given in Tables 3.1 and 3.2 refer to single core calculations.

3.2 Flow rates with Maxwell boundary conditions

A large amount of work has been dedicated to the extraction of the kinetic coefficients and their dependence on the Maxwell accommodation coefficient through various capillaries by performing experiments and comparing the corresponding kinetic results in the whole range of gas rarefaction. In the present work the tabulated results refer to the specific aspect ratio *H/W=0.24*.

In Tables 3.3 and 3.4 the kinetic coefficients G_P and G_T are tabulated in for indicative values of δ from the free molecular limit up to the slip regime and in the whole range of the Maxwell accommodation coefficient α^M from zero to one for the pressure and temperature driven flows respectively. As it is seen in Table 3.3 for all values of the gas rarefaction parameter the dimensionless flow rate is decreased as the accommodation coefficient is increased and the gas surface interaction becomes more diffuse. It may be also observed that the well-known Knudsen minimum is always present in all values of the accommodation coefficient.

Table 3.3: Dimensionless flow rate G_P with Maxwell boundary conditions

H/W=0.24										
δ	a=0.1	0.2	0.3	0.4	0.5	0.6	0.7	0.8	0.9	1
0	24.7454	11.7551	7.4398	5.2932	4.0142	3.1689	2.5714	2.1287	1.7893	1.5221
0.1	16.0874	8.2785	5.5309	4.1021	3.2190	2.6167	2.1790	1.8464	1.5853	1.3752
1	14.2781	7.1083	4.7063	3.4983	2.7690	2.2797	1.9281	1.6628	1.4554	1.2886
5	14.7978	7.5932	5.1712	3.9514	3.2147	2.7208	2.3663	2.0992	1.8906	1.7230
10	15.6408	8.3652	5.9079	4.6668	3.9155	3.4106	3.0472	2.7727	2.5577	2.3844

Continuing with Table 3.4 it is seen that in the temperature driven flow the dimensionless flow rate is monotonically decreased as the accommodation coefficient is increased. It is noted that for $\alpha=1$ the reflection is purely diffuse. With regard to the gas rarefaction parameter it is seen that as δ is increased, i.e., the flow becomes less rarefied the dimensionless flow rate is monotonically decreased. This is a well-known trend and it is contributed to the fact that thermal creep is reduced as the flow approaches the continuum regime.

Table 3.4: Dimensionless flow rate G_T with Maxwell boundary conditions

H/W=0.24										
δ	a=0.1	0.2	0.3	0.4	0.5	0.6	0.7	0.8	0.9	1
0	12.3727	5.8776	3.7199	2.6466	2.0071	1.5844	1.2857	1.0644	0.8946	0.7610
0.1	3.4589	2.3458	1.7818	1.4311	1.1883	1.0088	0.8700	0.7592	0.6685	0.5929
1	0.6687	0.6047	0.5526	0.5090	0.4719	0.4398	0.4116	0.3867	0.3644	0.3443
5	0.1515	0.1528	0.1539	0.1548	0.1556	0.1563	0.1569	0.1575	0.1580	0.1585
10	0.0775	0.0800	0.0823	0.0844	0.0865	0.0885	0.0904	0.0923	0.0941	0.0958

3.3 Flow rates with Cercignani-Lampis boundary conditions

Tables 3.5 and 3.6 provide indicative values of the dimensionless flow rates for the pressure driven flow and Tables 3.7 and 3.8 the dimensionless flow rates for the temperature driven flow. The flow rates depend on δ, as well as on the tangential momentum and normal energy accommodation coefficients α_t and α_n respectively. Results are provided for two aspect ratios.

As it seen in Tables 3.5 and 3.6 the dimensionless flow rates depend strongly on the tangential momentum accommodation coefficient (TMAC) and very weakly on the normal energy accommodation coefficient (NEAC). More specifically for the same values of δ and α_t

the dimensionless flow rate G_P changes slightly with α_n. Regarding the rarefaction parameter as its value increases from zero to around one the flow rate is reduced and after that as δ is further increased G_P increases again. This is the so-called Knudsen minimum which is also present here. The tangential momentum accommodation coefficient reduces the flow as its value increases, i.e. as the scattering changes from specular to diffuse. For TMAC larger than unity the flow rate is further reduced due to back scattering. As pointed above, the normal energy accommodation coefficient is the parameter that slightly affects the flow rate. As δ increases the impact of a_n on the flow becomes even smaller. Also, for $a_t < 1$, an increase of a_n results on decreasing the value of G_P, while for $a_t > 1$ it has the opposite effect. In the case of $a_t = 1$, then the coefficient a_n doesn't affect the flow at all. All these remarks are the qualitatively the same for both aspect ratios. Quantitatively, as the aspect ratio is decreased the effect of a_n on the flow seems to increase slightly. Also, the decrease in the aspect ratio leads to an increase of the Poiseuille flow rates.

The dimensionless flow rate due to the temperature gradient is given in Tables 3.7 and 3.8. Now, the all three parameters, including the normal energy accommodation coefficient, affect the flow. As expected in thermal creep flows, as the gas rarefaction parameter is increased the flow rate is monotonically decreased, implying that the role of the temperature gradient on a flow in the hydrodynamic regime is insignificant. The effect of the tangential momentum accommodation coefficient remains the same as for the Poiseuille flow, i.e., as the TMAC is increased the flow rate is reduced. As for the normal energy accommodation coefficient it affects the flow in the same way as before, but only for $\delta < 3$. For greater values of δ, a_n has the opposite effect, meaning that for values of $a_t < 1$ an increase of a_n results also in an increase on thermal creep and for $a_t > 1$ the thermal creep flow is reduced as a_n increases. For $a_t = 1$ the flow rate is independent of the normal energy accommodation coefficient.

Table 3.5: Dimensionless flow rate G_P with Cercignani-Lampis boundary conditions (*H/W=1*)

H/W=1							
	a_t	a_n =0.1	0.2	0.4	0.6	0.8	1
δ=0	0.1	9.2114	8.9694	8.7352	8.6217	8.5569	8.5171
	0.2	4.6537	4.5630	4.4544	4.3917	4.3517	4.3251
	0.6	1.4776	1.4668	1.4512	1.4397	1.4308	1.4238
	1	0.8387	0.8387	0.8387	0.8387	0.8387	0.8387
	1.4	0.5321	0.5386	0.5483	0.5559	0.5626	0.5688
	1.8	0.2858	0.2993	0.3191	0.3352	0.3498	0.3643
	1.9	0.2109	0.2277	0.2526	0.2728	0.2912	0.3099
δ=0.1	0.1	8.6270	8.6205	8.6194	8.6187	8.6183	8.6182
	0.2	4.4736	4.4718	4.4703	4.4693	4.4687	4.4683
	0.6	1.5958	1.5952	1.5944	1.5938	1.5934	1.5931
	1	0.9971	0.9971	0.9971	0.9971	0.9971	0.9971
	1.4	0.7241	0.7246	0.7253	0.7257	0.7261	0.7263
	1.8	0.5561	0.5570	0.5583	0.5592	0.5599	0.5603
	1.9	0.5223	0.5233	0.5248	0.5258	0.5265	0.5270
δ=1	0.1	8.4673	8.4531	8.4357	8.4226	8.4121	8.4036
	0.2	4.2730	4.2667	4.2567	4.2486	4.2417	4.2360
	0.6	1.3693	1.3682	1.3662	1.3643	1.3626	1.3610
	1	0.7756	0.7756	0.7756	0.7756	0.7756	0.7756
	1.4	0.4990	0.4997	0.5012	0.5028	0.5043	0.5059
	1.8	0.3045	0.3062	0.3096	0.3131	0.3167	0.3206
	1.9	0.2575	0.2597	0.2641	0.2685	0.2731	0.2780
δ=5	0.1	8.6270	8.6205	8.6194	8.6187	8.6183	8.6182
	0.2	4.4736	4.4718	4.4703	4.4693	4.4687	4.4683
	0.6	1.5958	1.5952	1.5944	1.5938	1.5934	1.5931
	1	0.9971	0.9971	0.9971	0.9971	0.9971	0.9971
	1.4	0.7241	0.7246	0.7253	0.7257	0.7261	0.7263
	1.8	0.5561	0.5570	0.5583	0.5592	0.5599	0.5603
	1.9	0.5223	0.5233	0.5248	0.5258	0.5265	0.5270
δ=10	0.1	8.9761	8.9675	8.9630	8.9593	8.9552	8.9524
	0.2	4.8389	4.8354	4.8310	4.8273	4.8241	4.8213
	0.6	1.9391	1.9378	1.9357	1.9339	1.9323	1.9309
	1	1.3240	1.3240	1.3240	1.3240	1.3240	1.3240
	1.4	1.0438	1.0449	1.0468	1.0485	1.0501	1.0514
	1.8	0.8762	0.8783	0.8820	0.8854	0.8884	0.8911
	1.9	0.8435	0.8459	0.8501	0.8538	0.8572	0.8603

Table 3.6: Dimensionless flow rate G_P with Cercignani-Lampis boundary condition (*H/W=0.24*)

H/W=0.24							
	a_t	a_n =0.1	0.2	0.4	0.6	0.8	1
δ=0	0.1	15.6884	15.0879	14.5872	14.3718	14.2569	14.1894
	0.2	8.0392	7.7650	7.4837	7.3419	7.2594	7.2081
	0.6	2.6514	2.6073	2.5520	2.5166	2.4917	2.4735
	1	1.5219	1.5219	1.5219	1.5219	1.5219	1.5219
	1.4	0.9759	1.0016	1.0340	1.0563	1.0741	1.0897
	1.8	0.5690	0.6106	0.6617	0.6974	0.7269	0.7544
	1.9	0.4456	0.4892	0.5436	0.5823	0.6148	0.6457
δ=0.1	0.1	14.8321	14.5671	14.2900	14.1496	14.0682	14.0177
	0.2	7.5578	7.4150	7.2432	7.1455	7.0846	7.0450
	0.6	2.4538	2.4258	2.3868	2.3599	2.3401	2.3252
	1	1.3751	1.3751	1.3751	1.3751	1.3751	1.3751
	1.4	0.8584	0.8759	0.9002	0.9181	0.9330	0.9463
	1.8	0.4902	0.5195	0.5589	0.5880	0.6127	0.6363
	1.9	0.3905	0.4216	0.4636	0.4946	0.5212	0.5469
δ=1	0.1	14.0333	14.0119	13.9897	13.9725	13.9588	13.9481
	0.2	7.0294	7.0183	7.0012	6.9872	6.9759	6.9667
	0.6	2.2738	2.2704	2.2644	2.2591	2.2544	2.2503
	1	1.2885	1.2885	1.2885	1.2885	1.2885	1.2885
	1.4	0.8406	0.8430	0.8475	0.8519	0.8562	0.8604
	1.8	0.5632	0.5675	0.5758	0.5838	0.5918	0.6001
	1.9	0.5051	0.5099	0.5190	0.5277	0.5366	0.5459
δ=5	0.1	14.6273	14.6137	14.6088	14.6053	14.6027	14.6006
	0.2	7.5296	7.5255	7.5216	7.5187	7.5166	7.5149
	0.6	2.7199	2.7187	2.7169	2.7157	2.7147	2.7140
	1	1.7220	1.7220	1.7220	1.7220	1.7220	1.7220
	1.4	1.2816	1.2826	1.2842	1.2853	1.2861	1.2867
	1.8	1.0280	1.0300	1.0331	1.0353	1.0369	1.0382
	1.9	0.9800	0.9823	0.9856	0.9881	0.9900	0.9913
δ=10	0.1	15.4955	15.4776	15.4665	15.4573	15.4493	15.4422
	0.2	8.2638	8.2569	8.2469	8.2393	8.2325	8.2266
	0.6	3.3996	3.3969	3.3922	3.3884	3.3851	3.3821
	1	2.3801	2.3801	2.3801	2.3801	2.3801	2.3801
	1.4	1.9268	1.9293	1.9333	1.9369	1.9402	1.9433
	1.8	1.6650	1.6695	1.6772	1.6844	1.6908	1.6969
	1.9	1.6154	1.6202	1.6290	1.6370	1.6442	1.6511

Table 3.7: Dimensionless flow rate G_T with Cercignani-Lampis boundary conditions (*H/W=1*)

H/W=1							
	a_t	a_n =0.1	0.2	0.4	0.6	0.8	1
δ=0	0.1	1.7844	1.3757	0.9590	0.7503	0.6276	0.5496
	0.2	1.1201	0.9610	0.7605	0.6396	0.5598	0.5047
	0.6	0.5454	0.5252	0.4933	0.4683	0.4480	0.4312
	1	0.4193	0.4193	0.4193	0.4193	0.4193	0.4193
	1.4	0.3420	0.3530	0.3710	0.3869	0.4017	0.4164
	1.8	0.2375	0.2569	0.2883	0.3164	0.3442	0.3740
	1.9	0.1904	0.2130	0.2498	0.2828	0.3157	0.3519
δ=0.1	0.1	1.3839	1.1346	0.8375	0.6707	0.5662	0.4968
	0.2	0.9243	0.8150	0.6640	0.5659	0.4980	0.4495
	0.6	0.4713	0.4558	0.4301	0.4091	0.3916	0.3768
	1	0.3649	0.3649	0.3649	0.3649	0.3649	0.3649
	1.4	0.2984	0.3069	0.3219	0.3355	0.3486	0.3617
	1.8	0.2054	0.2203	0.2464	0.2706	0.2949	0.3213
	1.9	0.1642	0.1817	0.2121	0.2403	0.2691	0.3009
δ=1	0.1	0.5139	0.4865	0.4362	0.3964	0.3643	0.3383
	0.2	0.4296	0.4120	0.3804	0.3541	0.3321	0.3135
	0.6	0.2955	0.2916	0.2843	0.2774	0.2711	0.2652
	1	0.2557	0.2557	0.2557	0.2557	0.2557	0.2557
	1.4	0.2286	0.2311	0.2363	0.2415	0.2469	0.2524
	1.8	0.1807	0.1851	0.1942	0.2037	0.2139	0.2251
	1.9	0.1609	0.1659	0.1763	0.1873	0.1991	0.2122
δ=5	0.1	0.1446	0.1470	0.1496	0.1521	0.1545	0.1568
	0.2	0.1419	0.1434	0.1457	0.1480	0.1502	0.1523
	0.6	0.1360	0.1365	0.1376	0.1386	0.1397	0.1407
	1	0.1378	0.1378	0.1378	0.1378	0.1378	0.1378
	1.4	0.1405	0.1402	0.1394	0.1385	0.1377	0.1368
	1.8	0.1370	0.1364	0.1350	0.1336	0.1320	0.1304
	1.9	0.1345	0.1339	0.1324	0.1308	0.1291	0.1274
δ=10	0.1	0.0769	0.0794	0.0832	0.0868	0.0904	0.0938
	0.2	0.0784	0.0802	0.0834	0.0865	0.0896	0.0926
	0.6	0.0825	0.0833	0.0846	0.0860	0.0874	0.0888
	1	0.0878	0.0878	0.0878	0.0878	0.0878	0.0878
	1.4	0.0929	0.0924	0.0912	0.0900	0.0887	0.0874
	1.8	0.0959	0.0949	0.0928	0.0905	0.0881	0.0857
	1.9	0.0961	0.0950	0.0927	0.0902	0.0876	0.0849

Table 3.8: Dimensionless flow rate G_T with Cercignani-Lampis boundary conditions (*H/W=0.24*)

H/W=0.24							
	a_t	a_n 0.1	0.2	0.4	0.6	0.8	1
δ=0	0.1	3.0341	2.2577	1.5674	1.2489	1.0668	0.9515
	0.2	2.0055	1.6569	1.2797	1.0779	0.9532	0.8703
	0.6	1.0168	0.9634	0.8910	0.8409	0.8032	0.7739
	1	0.7610	0.7610	0.7610	0.7610	0.7610	0.7610
	1.4	0.6081	0.6366	0.6757	0.7058	0.7322	0.7571
	1.8	0.4500	0.4960	0.5585	0.6077	0.6529	0.6993
	1.9	0.3834	0.4325	0.5007	0.5557	0.6074	0.6617
δ=0.1	0.1	2.0274	1.6550	1.2371	1.0129	0.8749	0.7832
	0.2	1.4531	1.2579	1.0115	0.8643	0.7678	0.7012
	0.6	0.7884	0.7529	0.6998	0.6605	0.6300	0.6057
	1	0.5928	0.5928	0.5928	0.5928	0.5928	0.5928
	1.4	0.4715	0.4914	0.5214	0.5458	0.5678	0.5891
	1.8	0.3450	0.3777	0.4257	0.4655	0.5030	0.5419
	1.9	0.2973	0.3322	0.3843	0.4280	0.4699	0.5144
δ=1	0.1	0.5895	0.5655	0.5197	0.4838	0.4554	0.4329
	0.2	0.5244	0.5052	0.4711	0.4435	0.4210	0.4025
	0.6	0.3973	0.3913	0.3801	0.3700	0.3610	0.3529
	1	0.3443	0.3443	0.3443	0.3443	0.3443	0.3443
	1.4	0.3057	0.3097	0.3175	0.3252	0.3329	0.3408
	1.8	0.2578	0.2643	0.2773	0.2904	0.3041	0.3190
	1.9	0.2422	0.2492	0.2633	0.2775	0.2926	0.3091
δ=5	0.1	0.1510	0.1544	0.1587	0.1628	0.1668	0.1706
	0.2	0.1509	0.1530	0.1565	0.1599	0.1631	0.1663
	0.6	0.1534	0.1541	0.1555	0.1570	0.1584	0.1598
	1	0.1584	0.1584	0.1584	0.1584	0.1584	0.1584
	1.4	0.1632	0.1627	0.1615	0.1603	0.1591	0.1578
	1.8	0.1645	0.1635	0.1615	0.1593	0.1570	0.1546
	1.9	0.1639	0.1629	0.1607	0.1583	0.1557	0.1531
δ=10	0.1	0.0792	0.0820	0.0864	0.0907	0.0948	0.0989
	0.2	0.0808	0.0829	0.0866	0.0902	0.0937	0.0971
	0.6	0.0885	0.0894	0.0910	0.0926	0.0943	0.0959
	1	0.0956	0.0956	0.0956	0.0956	0.0956	0.0956
	1.4	0.1022	0.1015	0.1001	0.0986	0.0971	0.0955
	1.8	0.1076	0.1063	0.1037	0.1009	0.0980	0.0949
	1.9	0.1086	0.1072	0.1043	0.1013	0.0980	0.0946

Chapter 4 **EXTRACTION OF ACCOMMODATION COEFFICIENTS FOR PRESSURE DRIVEN FLOW**

The mass flow rate for specific flow setups is obtained. The imposed geometrical and operational data are the same with the ones implemented in the experimental work reported in [1]. Based on these data, as well as on the dimensionless kinetic coefficients tabulated in the previous chapter the mass flow rate is computed using the Maxwell and the Cercignani-Lampis boundary conditions. The values of the accommodation coefficients providing the best agreement between computed and measured mass flow rates are the ones which characterize the gas –surface interaction.

4.1 Mass flow rate parameters for pressure driven flow

According to the description in paragraph 2.4 the mass flow rate, based on (2.72) may be computed as

$$G_p = \dot{m}\frac{L\sqrt{2RT}}{H^2 W \Delta p} \tag{4.1}$$

where the geometrical parameters of the channel (H, W, L) as well as the physical properties (R, ω, μ) for all gases are known (Table 4.1). In addition, the appropriate database with the kinetic coefficients for various values of δ, a_t, a_n and a^M is available from the linearized kinetic model. The gas rarefaction parameter is computed as

$$\delta_m = \frac{p_m H}{\mu(T)\sqrt{2RT}} \tag{4.2}$$

based on the data from Tables A.1 and A.2 for each gas of [1] The temperatures of both the pressure and the temperature gradient experiments are also known. The room temperature is T=293.15K for the pressure driven flow and the temperature differences are ΔT=58K and ΔT=67.5K for the two temperature driven flows.

Table 4.1: Physical properties of gases

Gas	Helium	Neon	Nitrogen	Argon	Krypton
μ_{ref} [Pa s] 10^{-5}	1.865	2.975	1.656	2.117	2.328
ω [-]	0.66	0.66	0.74	0.81	0.8
R [J/lg K]	2078	412	296.8	208.1	99.22

The only unknown parameters are the pressures at the two channel ends for the various tests on each experimental setup. The inlet and outlet pressures for the pressure driven flow are evaluated by (4.1) and (4.2) following the procedure outlined in paragraph 2.4, based on the rarefaction parameter δ_m in [1]. Since in this case the unknowns of (4.1) and (4.2) were the pressure difference Δp and the mean pressure p_m respectively, as inputs of $G_P, \dot{m}$ and δ_m were used, given the tested gas, to extract the desired variables.

4.2 Maxwell accommodation coefficient for pressure driven flow

In the Maxwell boundary conditions there is only one free parameter, namely the Maxwell accommodation coefficient for characterizing the gas-surface interaction. This means that for the pressure and temperature gradient driven flows the value of the accommodation coefficient is not necessarily the same. Thus, the extraction of the accommodation coefficient for the pressure and temperature driven flow was performed separately. For the pressure driven flow to extract the value of the accommodation coefficient for each gas an attempt was made initially to match the numerical and experimental mass flow rates for the lower values of $\delta \in [6,20]$, because the coefficient has a more pronounced effect on the mass flow rates and thus leads to smaller uncertainties and errors. As a starting value for the AC the measured experimental one was used and was accordingly altered to obtain the best possible agreement between computations and measurements. An excellent agreement has been obtained for the tested values and the results are presented in Tables 4.2-4.4. The important outcome was that for each case on all gases the numerical value of the AC had a relative error compared to the experimental measured, [1], less than 4%, 4%, 3%, 3% and 5% for He, Ne, N_2, Ar and Kr, respectively.

To further clarify the agreement between the results, the Euclidian norm of the coefficient a_P^M was calculated for each gas based on the results from Tables 4.2-4.4. The deduced values along with two additional values in the range of ±0.05 were tested for all the given experimental data and are presented for all five gases in Figures 4.1-4.5. In these figures the error between the numerical and experimental mass flow rate, as well as the mass flow

rates are provided. It can be seen that the initial chosen value of AC produces the smallest error with the divergence from zero be less than 1%, while the other two produce an error of +5% for a lower value of AC and -5% for greater. As the value of δ increases ($\delta > 20$) the error curve for all three ACs starts to decreases numerically, i.e. the middle AC begins to deviate from zero, meaning that the effect of the coefficient on the flow is becoming less important as it moves to the hydrodynamic regime. Finally, the selected values of the Maxwell accommodation coefficient providing the best agreement between the computed and the measured flow rates are given in Table 4.5.

Table 4.2: Computed values of a_P^M for pressure driven flow for Helium and Neon

He (a_P^M [1]=0.773)				**Ne** (a_P^M [1]=0.763)			
δ	a_P^M	M [kg/s]	M Diff [%]	δ	a_P^M	M [kg/s]	M Diff [%]
6.03	0.8	1.47E-09	3.49	8.63	0.787	2.95E-10	3.15
8.58	0.788	2.39E-10	1.94	9.18	0.786	3.42E-10	3.01
9.31	0.788	1.37E-10	1.94	10	0.777	1.20E-09	1.83
9.71	0.797	1.78E-10	3.10	10.5	0.777	1.49E-09	1.83
10.3	0.802	1.35E-09	3.75	11.5	0.777	1.05E-09	1.83

Table 4.3: Computed values of a_P^M for pressure driven flow for Nitrogen and Argon

N_2 (a_P^M [1]=0.779)				**Ar** (a_P^M [1]=0.785)			
δ	a_P^M	M [kg/s]	M Diff [%]	δ	a_P^M	M [kg/s]	M Diff [%]
9.19	0.8	4.08E-10	2.70	9.11	0.805	2.65E-10	2.55
10.5	0.801	6.91E-10	2.82	9.79	0.798	6.12E-10	1.66
12.7	0.801	1.20E-09	2.82	11.3	0.801	8.43E-10	2.04
16.1	0.801	1.67E-09	2.82	13.3	0.797	1.24E-09	1.53
20.3	0.798	2.69E-09	2.44	15.9	0.79	1.89E-09	0.64

Table 4.4: Computed values of a_P^M for pressure driven flow for Krypton

Kr (a_P^M [1]=0.796)			
δ	a_P^M	M [kg/s]	M Diff [%]
8.89	0.833	5.07E-10	4.65
10.1	0.822	6.82E-10	3.27
11.7	0.82	1.87E-09	3.02
13.2	0.818	2.73E-09	2.76
15.6	0.82	2.05E-09	3.02

Table 4.5: Computed values of a_P^M over the whole range of gas rarefaction for all gases

Gas	Helium	Neon	Nitrogen	Argon	Krypton
a_P^M	0.795	0.781	0.8	0.798	0.823

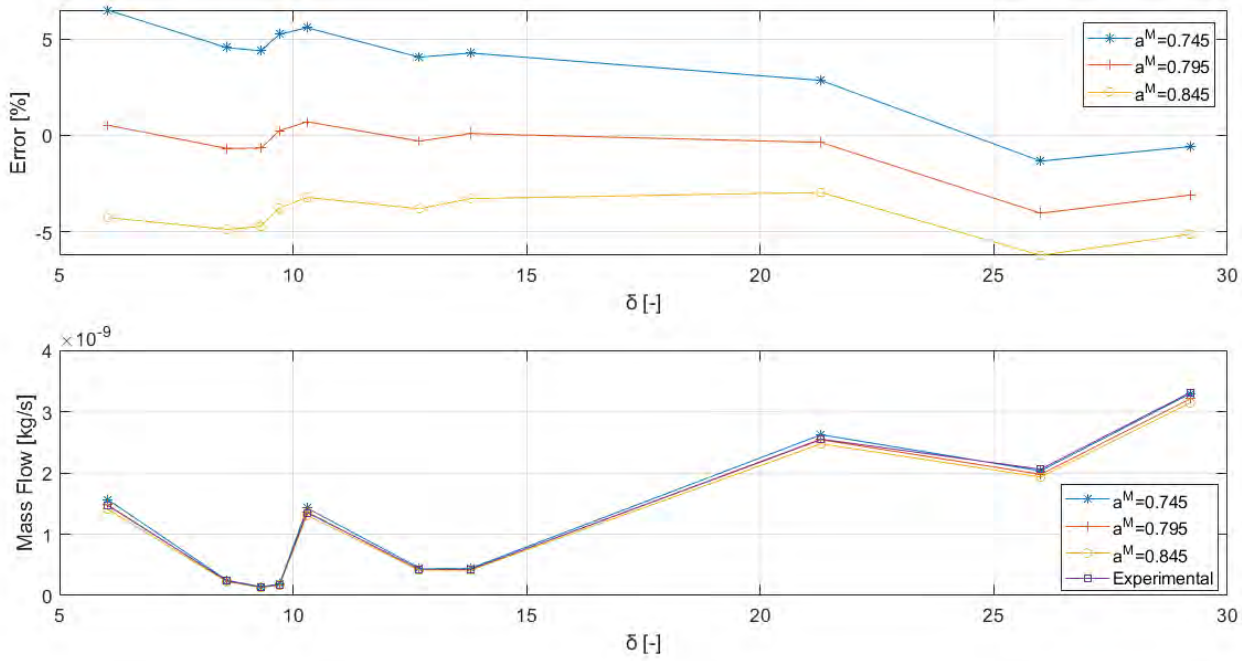

Figure 4.1: Comparison between computed and measured mass flow rates of He for the pressure driven flow based on the Maxwell boundary conditions (a_P^M)

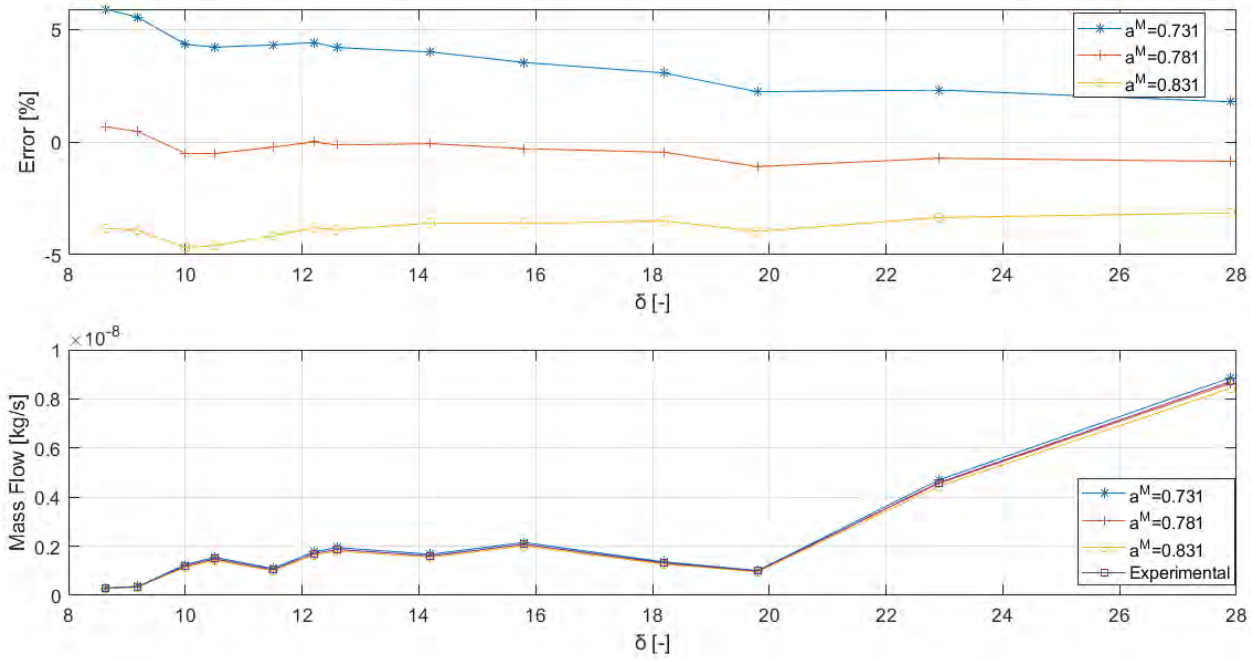

Figure 4.2: Comparison between computed and measured mass flow rates of Ne for the pressure driven flow based on the Maxwell boundary conditions (a_P^M)

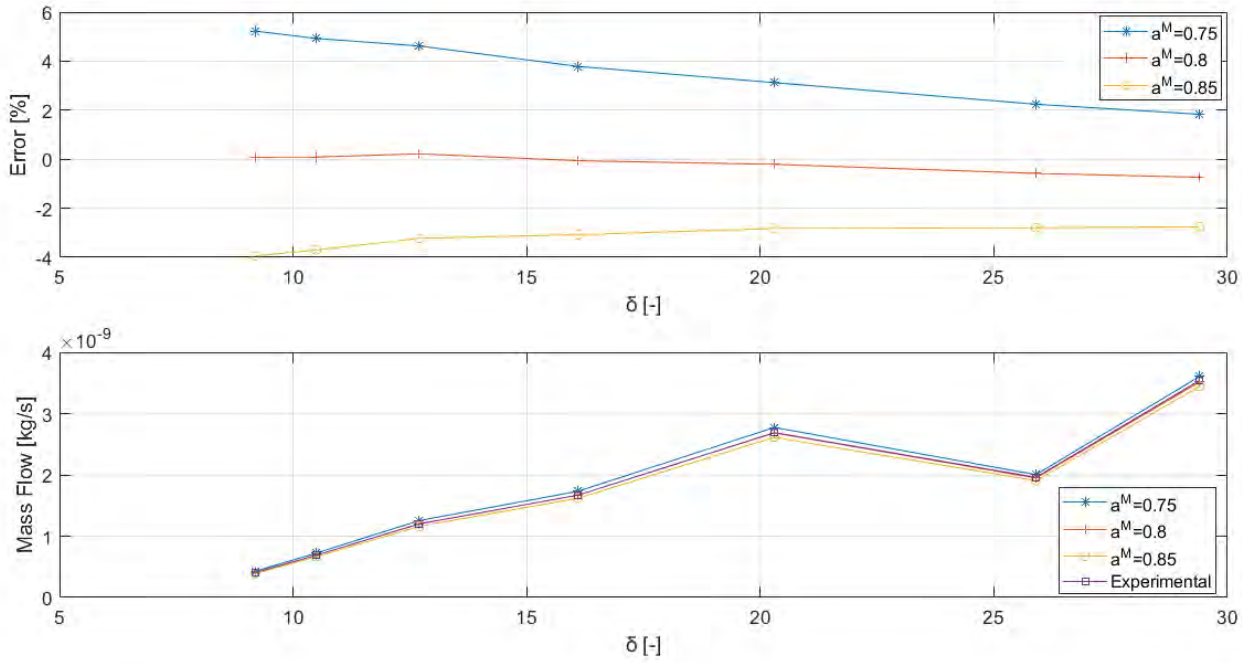

Figure 4.3: Comparison between computed and measured mass flow rates of N_2 for the pressure driven flow based on the Maxwell boundary conditions (a_P^M)

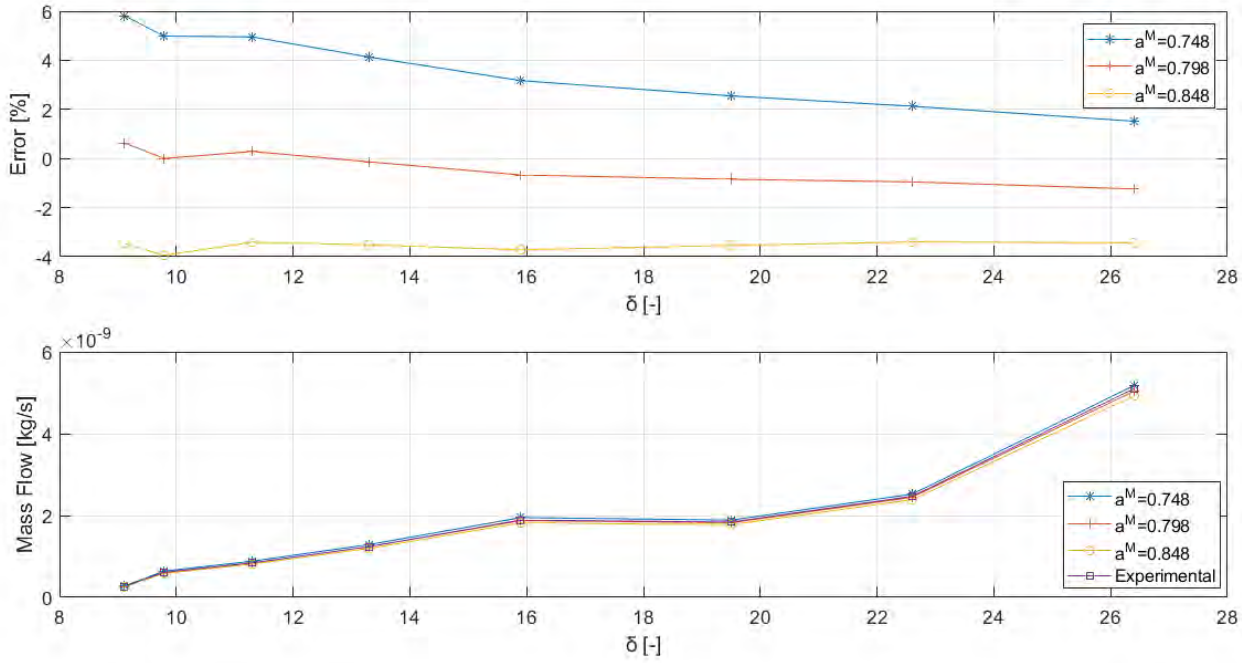

Figure 4.4: Comparison between computed and measured mass flow rates of Ar for the pressure driven flow based on the Maxwell boundary conditions (a_P^M)

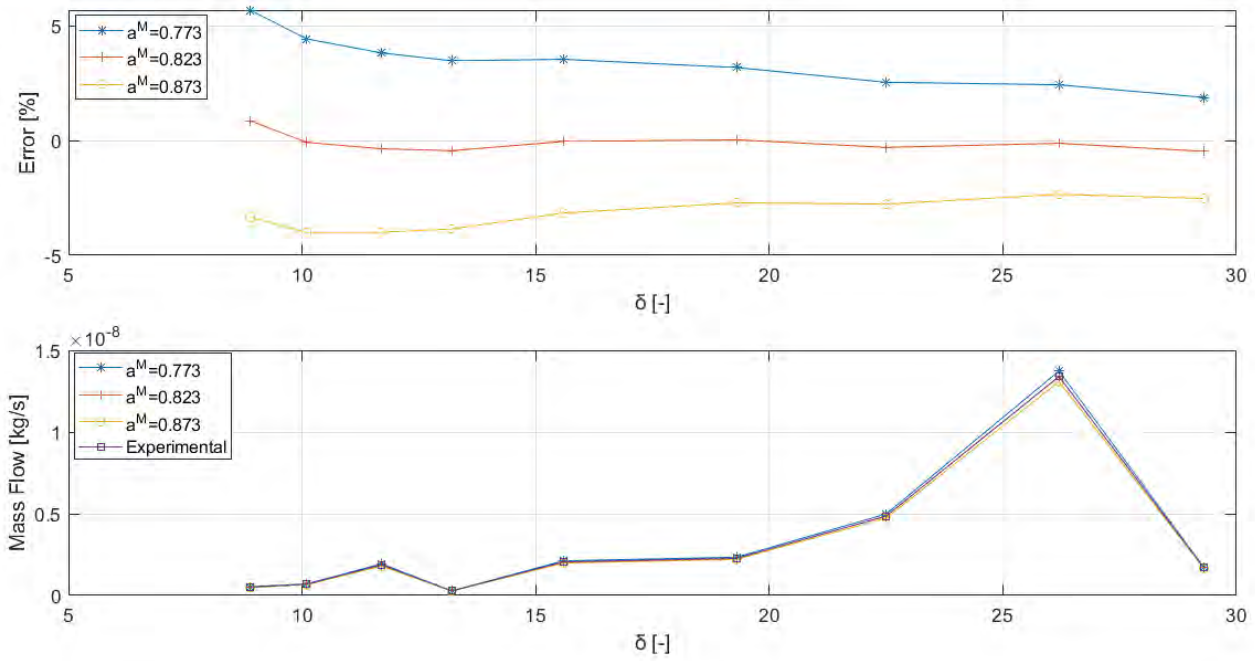

Figure 4.5: Comparison between computed and measured mass flow rates of Kr for the pressure driven flow based on the Maxwell boundary conditions (a_P^M)

4.3 Cercignani-Lampis tangential momentum accommodation coefficient for pressure driven flow

In the Cercignani-Lampis (CL) boundary conditions there are two free parameters, namely the CL tangential momentum (α_t) and normal energy (α_n) accommodation coefficients characterizing the gas-surface interaction. As discussed in Chapter 3, in the pressure driven flow the kinetic coefficient is almost independent of α_n and therefore is always set equal to one ($a_n = 1$). For estimating the tangential momentum accommodation coefficient, the pressure driven flow was employed by comparing the experimental with the numerical mass flow rates. More specifically, a_t was altered trying to match the results. The comparison at first was, also, performed for the experiments with the lower values of $\delta \in [6,20]$, beginning with the experimental values of the TMAC. The values of the coefficient α_t that resulted in the same mass flow rates as the experiments, while maintaining $\alpha_n = 1$, are presented in Tables 4.5-4.7 for all gases, along with the values of the mass flow rate as well as the values of α_t given in [1]. For all the gases the values of α_t obtained using the present methodology are very close with the ones reported in [1], having relative differences less than 5%, 5%, 4%, 4% and 6% for He, Ne, N_2, Ar and Kr, respectively.

In order to better judge the accuracy of the results, the Euclidean norm of the coefficient a_t was computed for each gas based on the results from Tables 4.6-4.8. To ensure that the chosen values were the ones that fit best a comparison was made with two additional values of a_t in the range of ±0.05 for each gas. The results are presented in Figures 4.6-4.10, where again the upper graph presents the error between the numerical and experimental results, while the lower graph the mass flow rates. Judging by the diagrams it is clear that the initially chosen values of the coefficient for each gas gives the best results for $\delta < 20$ with the error varying around zero in a range of ±2%. The error for the other two ACs is larger by 5% compared to the first value's error. As δ increases, i.e. the flow is moving to the hydrodynamic regime, the effect of the coefficient on the mass flow rate diminishes. Finally, the selected values of the CL TMAC providing the best agreement between the computed and the measured flow rates are given in Table 4.9. The results are relatively close to the ones reported in Table 4.5 for the Maxwell boundary conditions.

Table 4.6: Computed values of a_t for pressure driven flow for Helium and Neon

He (α_t [1]=0.763)				**Ne** (α_t [1]=0.752)			
a_n=1				a_n=1			
δ	α_t	M [kg/s]	M Diff %	δ	α_t	M [kg/s]	M Diff %
6.03	0.797	1.47E-09	4.46	8.63	0.784	2.95E-10	4.26
8.58	0.787	2.39E-10	3.15	9.18	0.782	3.42E-10	3.99
9.31	0.786	1.37E-10	3.01	10	0.774	1.20E-09	2.93
9.71	0.794	1.78E-10	4.06	10.5	0.772	1.49E-09	2.66
10.3	0.797	1.35E-09	4.46	11.5	0.773	1.05E-09	2.79

Table 4.7: Computed values of a_t for pressure driven flow for Nitrogen and Argon

N_2 (α_t [1]=0.768)				**Ar** (α_t [1]=0.775)			
a_n=1				a_n=1			
δ	α_t	M [kg/s]	M Diff %	δ	α_t	M [kg/s]	M Diff %
9.19	0.795	4.08E-10	3.52	9.11	0.799	2.65E-10	3.10
10.5	0.794	6.91E-10	3.39	9.79	0.793	6.12E-10	2.32
12.7	0.793	1.20E-09	3.26	11.3	0.795	8.43E-10	2.58
16.1	0.787	1.67E-09	2.47	13.3	0.786	1.24E-09	1.42
20.3	0.777	2.69E-09	1.17	15.9	0.779	1.89E-09	0.52

Table 4.8: Computed values of a_t for pressure driven flow for Krypton

Kr (α_t [1]=0.786)			
a_n=1			
δ	α_t	M [kg/s]	M Diff %
8.89	0.831	5.07E-10	5.73
10.1	0.817	6.82E-10	3.94
11.7	0.808	1.87E-09	2.80
13.2	0.805	2.73E-09	2.42
15.6	0.807	2.05E-09	2.67

Table 4.9: Computed values of a_t over the whole range of gas rarefaction for all gases

Gas	Helium	Neon	Nitrogen	Argon	Krypton
a_t	0.792	0.777	0.789	0.79	0.814

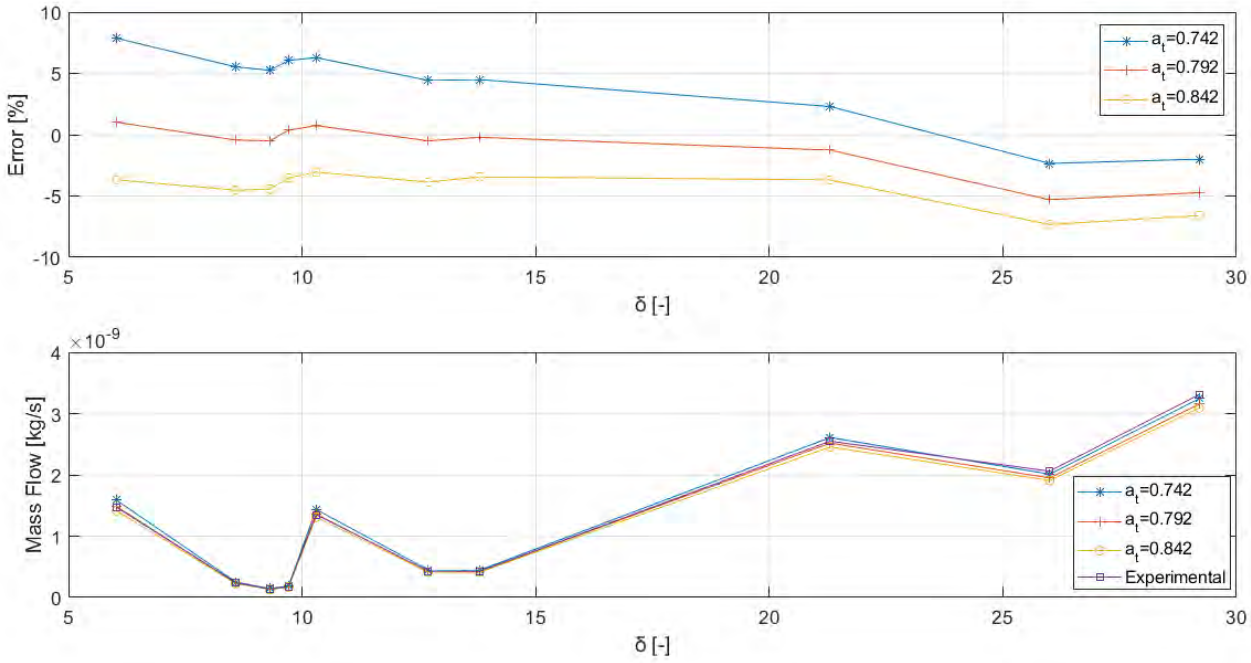

Figure 4.6: Comparison between computed and measured mass flow rates of He for the pressure driven flow based on the Cercignani-Lampis boundary conditions with various values of a_t and α_n=1

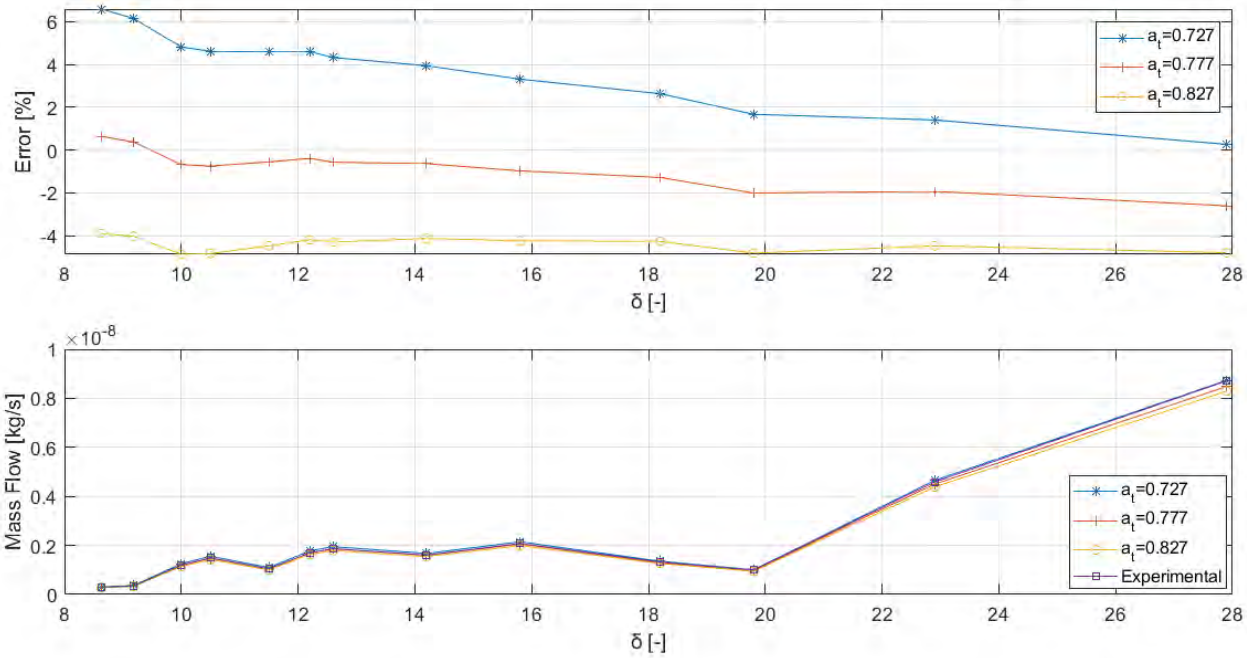

Figure 4.7: Comparison between computed and measured mass flow rates of Ne for the pressure driven flow based on the Cercignani-Lampis boundary conditions with various values of a_t and α_n=1

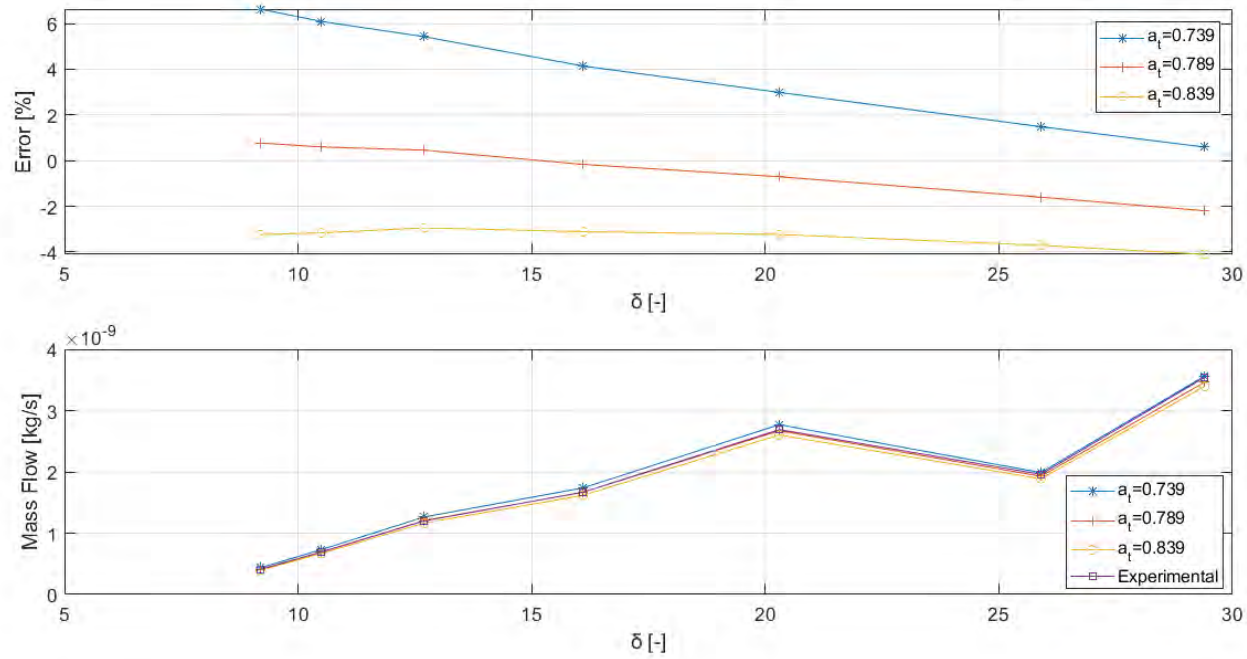

Figure 4.8: Comparison between computed and measured mass flow rates of N_2 for the pressure driven flow based on the Cercignani-Lampis boundary conditions with various values of a_t and α_n=1

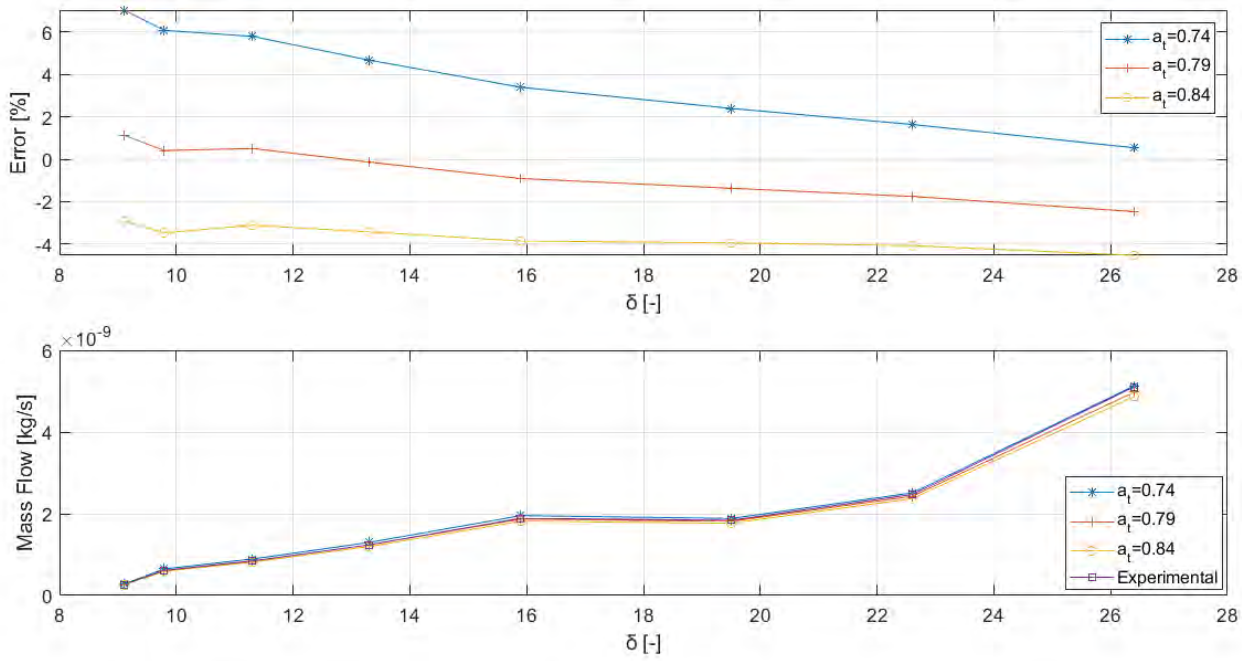

Figure 4.9: Comparison between computed and measured mass flow rates of Ar for the pressure driven flow based on the Cercignani-Lampis boundary conditions with various values of a_t and α_n=1

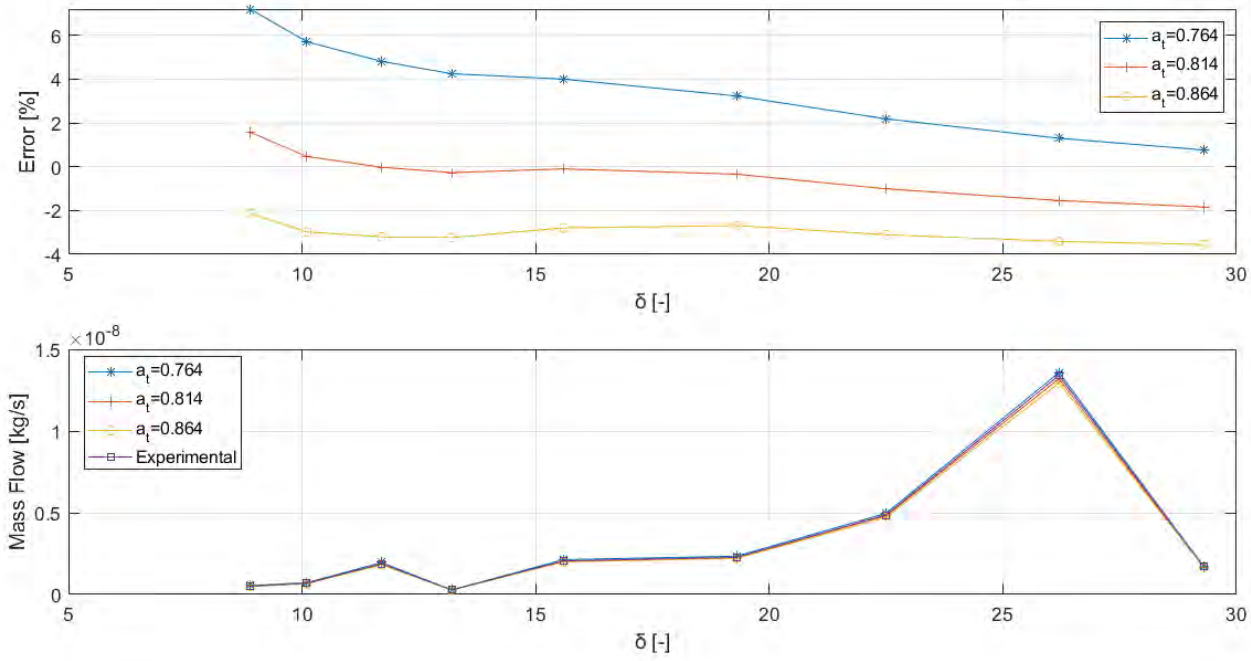

Figure 4.10: Comparison between computed and measured mass flow rates of Kr for the pressure driven flow based on the Cercignani-Lampis boundary conditions with various values of a_t and α_n=1

Chapter 5 **EXTRACTION OF ACCOMMODATION COEFFICIENTS FOR TEMPERATURE DRIVEN FLOW**

The mass flow rate for specific temperature driven flow setups is obtained. The imposed geometrical and operational data are the same with the ones implemented in the experimental work reported in [1]. Based on these data, as well as on the dimensionless kinetic coefficients tabulated in the Chapter 3, the mass flow rate is computed using the Maxwell and the Cercignani-Lampis boundary conditions. However, an identification of the value of the accommodation coefficients could not be done since large deviations exist between the computed and measured mass flow rates.

5.1 Mass flow rate for temperature driven flow

According to the description in paragraph 2.4 the mass flow rate, based on (2.71) may be computed as

$$M \approx G_T(\delta_m)\frac{2H^2W}{L}p_0\left(\frac{1}{\sqrt{2RT_1}}-\frac{1}{\sqrt{2RT_2}}\right) \tag{5.1}$$

where the geometrical parameters of the channel (*H, W, L*) as well as the physical properties (R, ω, μ) for all gases are known (Table 4.1). In addition, the appropriate database with the kinetic coefficients for various values of δ, a_t, a_n and a^M is available from the linearized kinetic model. The gas rarefaction parameter is computed as

$$\delta_m = \frac{p_0 H}{\mu(T_m)\sqrt{2RT_m}} \tag{5.2}$$

based on the data from Tables A.3-A.6 for each gas of [1]. As inputs for G_T and δ_m in eqs. (5.1) and (5.2) respectively the results from Tables A.3-A.6 of [1] were used in order to extract the pressure. The outcome from the two equations was very close most of the times with an average difference of 2%. Yet to avoid any uncertainties the measured pressure values from the experiment were used, although the average difference between the latter and the

former was 4%. The temperature differences for the two experiments are known and equal to ΔT=58K and ΔT=67.5K, while the pressure at the two ends of the channel is the same.

5.2 Maxwell accommodation coefficient for temperature driven flow

In the case of the temperature driven flow no exact match has been found between the experimental and numerical results. On the contrary significant differences have been observed, mainly at the lower values of δ where the discrepancies are maximized. For the lower values of δ the accommodation coefficient extracted from the experimental work [1] has been applied. Since there were no good agreement the experimental and numerical mass flow rates with their differences have been plotted for all available experimental data based on the experimental values of the accommodation coefficient. Moreover, an investigation is made using different values of the temperature difference than the reported experimental ones, in an effort to find the source of the large discrepancies. Results are reported for four different temperature differences (ΔT=45, 50, 55K as well as the experimental one ΔT=67.5K) because the numerical mass flow rate was always higher than the experimental for the lower values of δ. Then, due to the observed significant differences three additional values of a_T^M were tested, namely $a_T^M = 0.1, 0.5, 0.9$, in order to better understand the impact of the accommodation coefficient on the mass flow rate and find the most suitable values. This work has been performed for both experimental temperature differences since similar behavior was presented. Extensive results for ΔT=67.5K and ΔT=58K are displayed in Appendices C and D respectively.

Additional results are provided in Figures 5.1-5.10. Two figures are provided for each of the five gases. As seen in Figure 5.1, for He, the error is smaller than 10% in the range of $\delta \in [6,12]$. However, as δ decreases the error increases up to 150%. The error in this area is negligible at ΔT=50K and $a_T^M = 0.9$ (Figure 5.2). To continue with Ne, it is seen in Figures 5.3 and 5.4 that the error is in the range of 0-20% for $\delta \in [4,18]$ and it becomes smaller for $\delta \in [8,18]$, where the error is less than 10%. Concerning the lower values of δ the curve has a similar behavior as previously with the error keeps increasing as δ decreases. A decrease in the AC results to a smaller error in the range $\delta \in [6,18]$, while for a lower temperature difference, ΔT=55K and a higher AC could have the same outcome but for a greater range, $\delta \in [2,18]$. The discrepancies in the case of N_2, as shown in Figures 5.5 and 5.6 are filled with oscillations. Though in the range of $\delta \in [9,17]$ the error is almost constant and equal to 20%, at ΔT=55K the error approaches zero. For the initial temperature difference the error is

reduced if a more specular behavior of the gas is assumed, i.e. for a lower value of AC. In Figures 5.7 and 5.8 for Ar, it is seen that the error values concentrate near 40% for $\delta \in [2,4]$. In addition, a second area where the error is almost constant is observed in the range $\delta \in [7,16]$, where the error is equal to 20%. The former range is improved for a temperature difference between 45-50K while the latter one for ΔT=55K. At initial temperature difference the error in the second area can be reduced for a reduction in the AC. Finally, in Figures 5.9 and 5.10 for Kr the error becomes constant for $\delta \in [4,6]$ with error near 50%, for $\delta \in [6,12]$ with error near 37% and for $\delta \in [17,25]$ with error near 20%. The error approaches zero in the first case at ΔT=45K, in the second at ΔT=50K and in the third at ΔT=55K. The error in the third range also improves if the AC is decreased at the initial temperature difference. Unfortunately, no overall concluding remarks can be made. It seems that the Maxwell accommodation coefficient in the case of temperature driven flows depends on the gas rarefaction as well as on the imposed temperature difference.

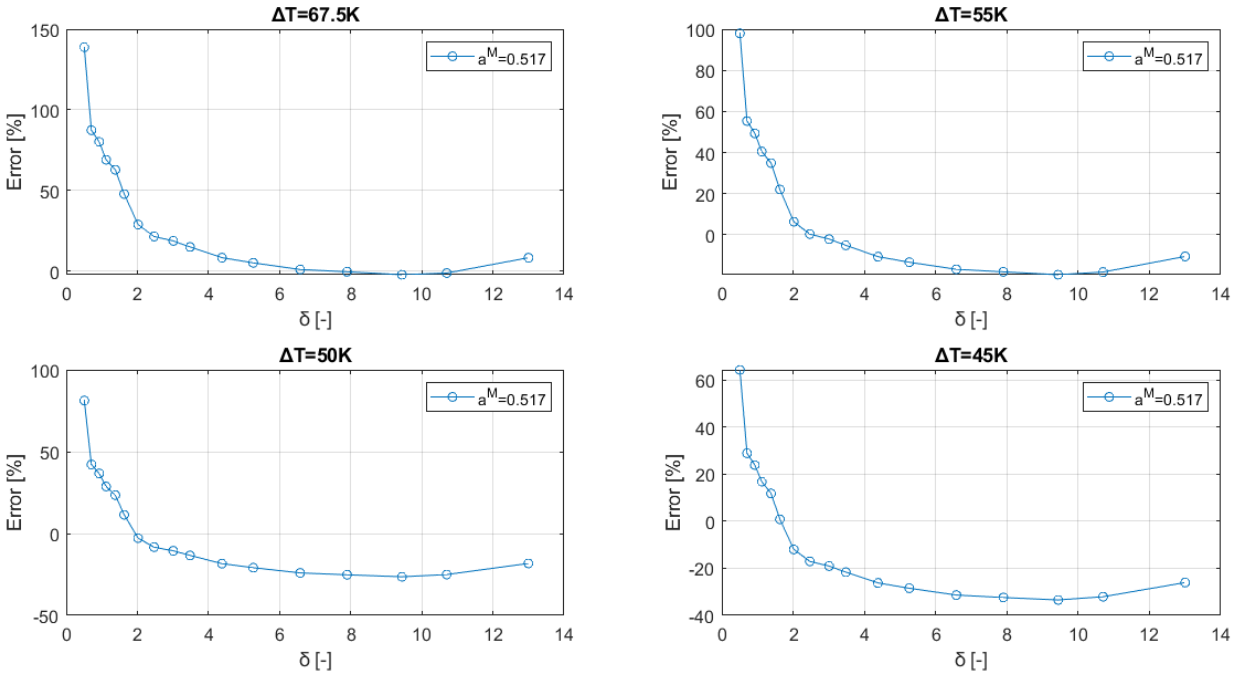

Figure 5.1: Relative difference between experimental and computational mass flow rates with Maxwell boundary conditions for various temperature differences in the case of He

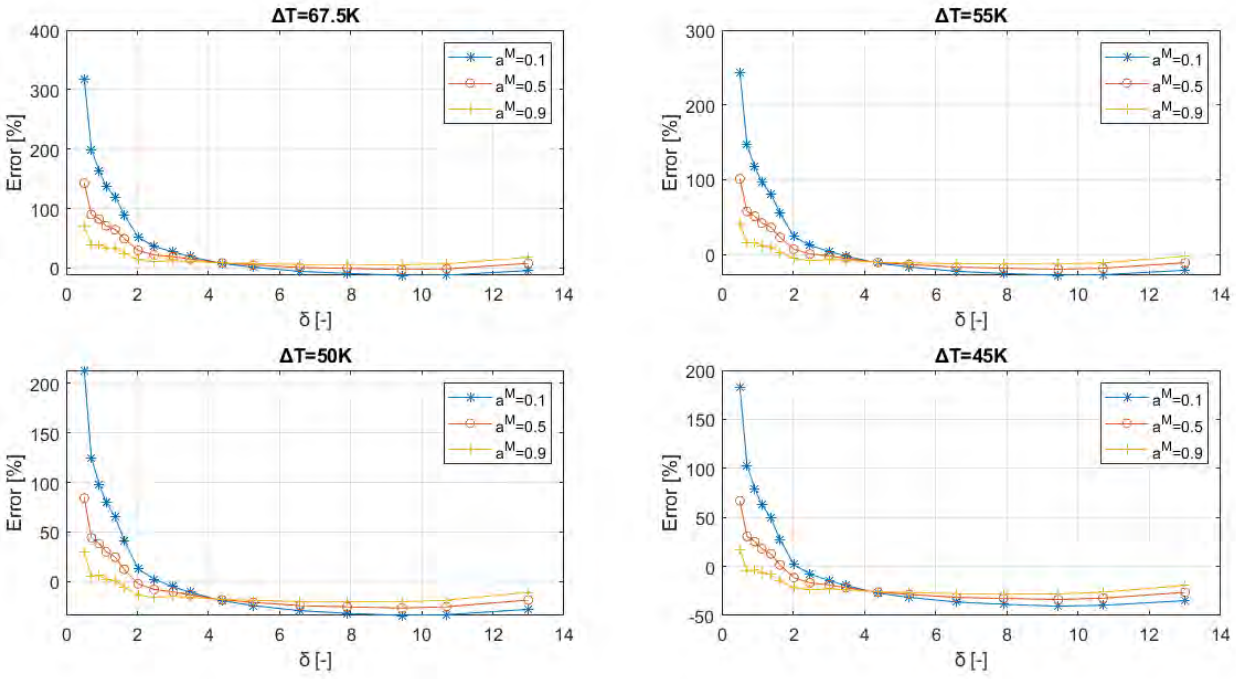

Figure 5.2: Relative difference between experimental and computational mass flow rates with Maxwell boundary conditions for various values of a_T^M and temperature differences in the case of He

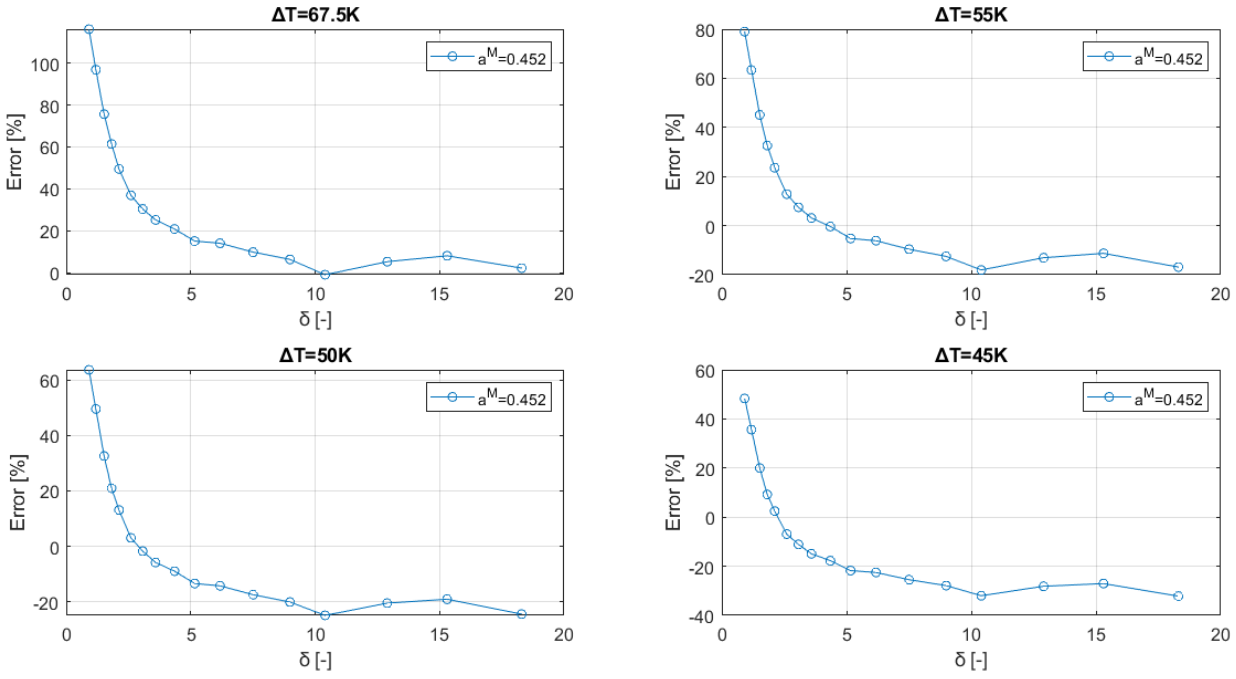

Figure 5.3: Relative difference between experimental and computational mass flow rates with Maxwell boundary conditions for various temperature differences in the case of Ne

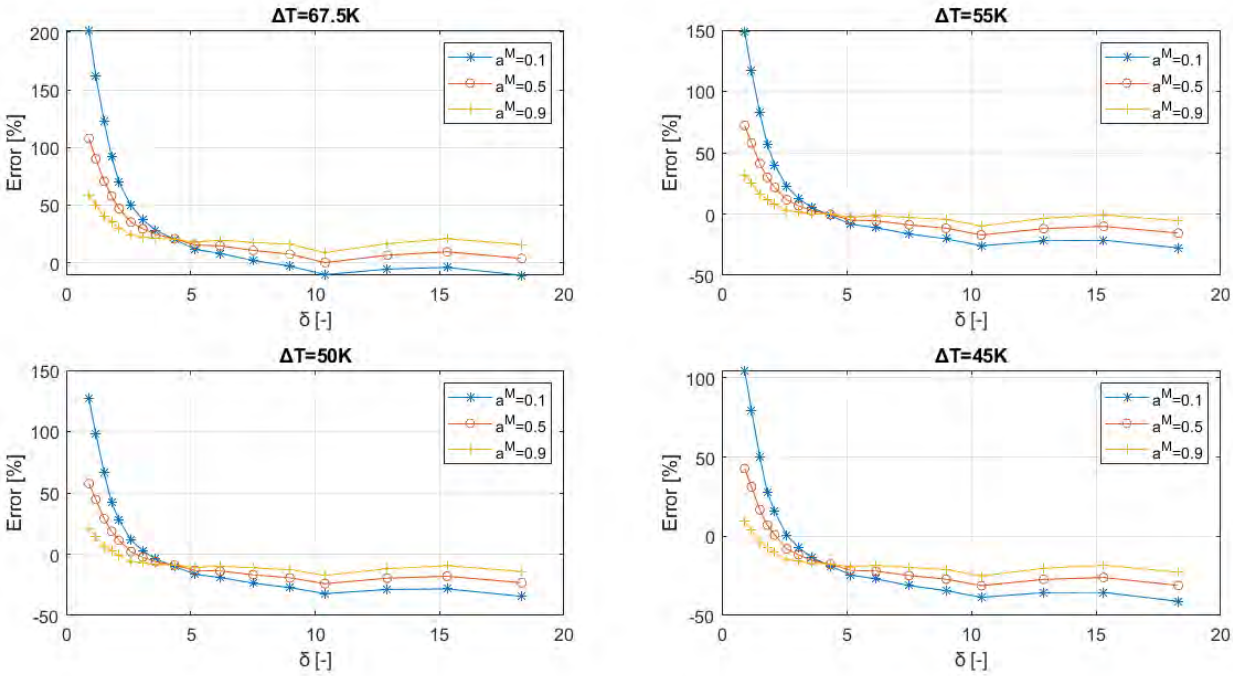

Figure 5.4: Relative difference between experimental and computational mass flow rates with Maxwell boundary conditions for various values of a_T^M and temperature differences in the case of Ne

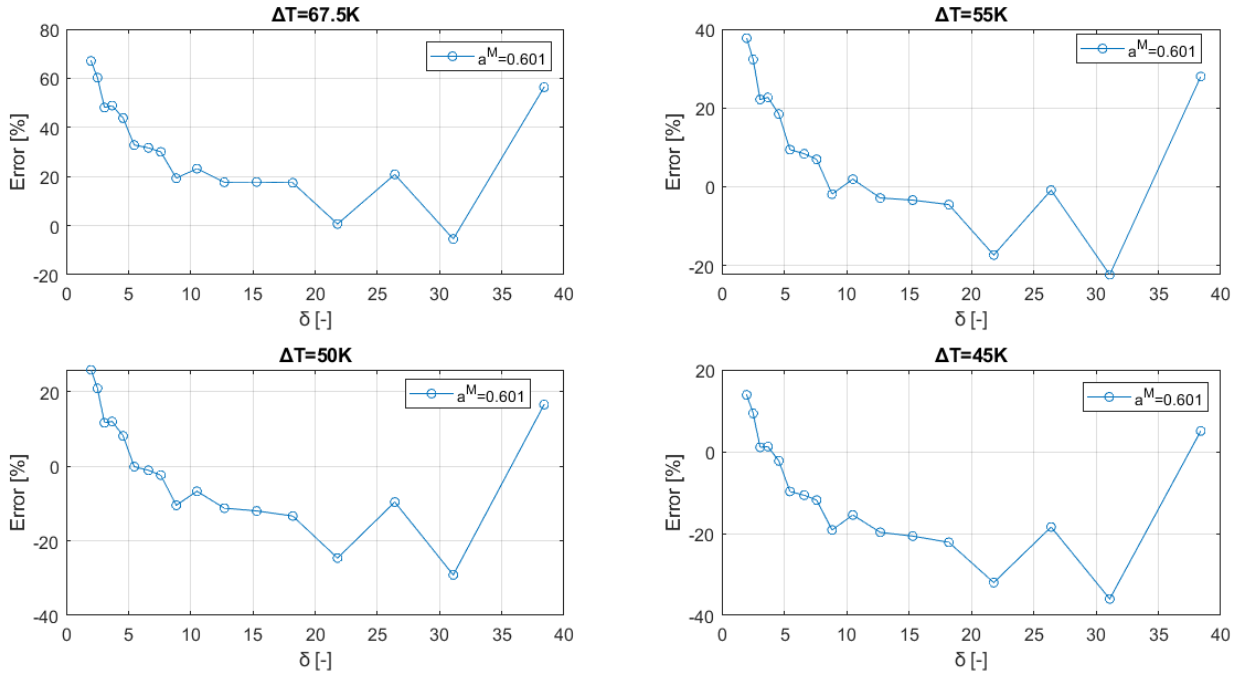

Figure 5.5: Relative difference between experimental and computational mass flow rates with Maxwell boundary conditions for various temperature differences in the case of N_2

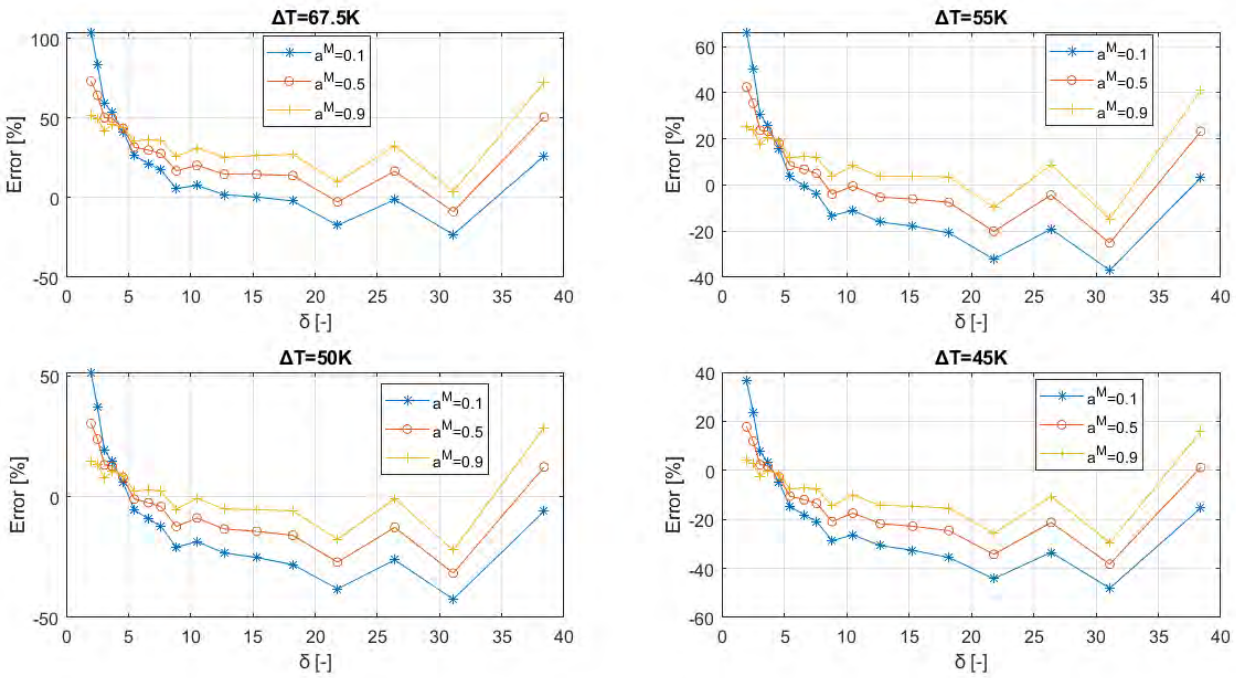

Figure 5.6: Relative difference between experimental and computational mass flow rates with Maxwell boundary conditions for various values of a_T^M and temperature differences in the case of N_2

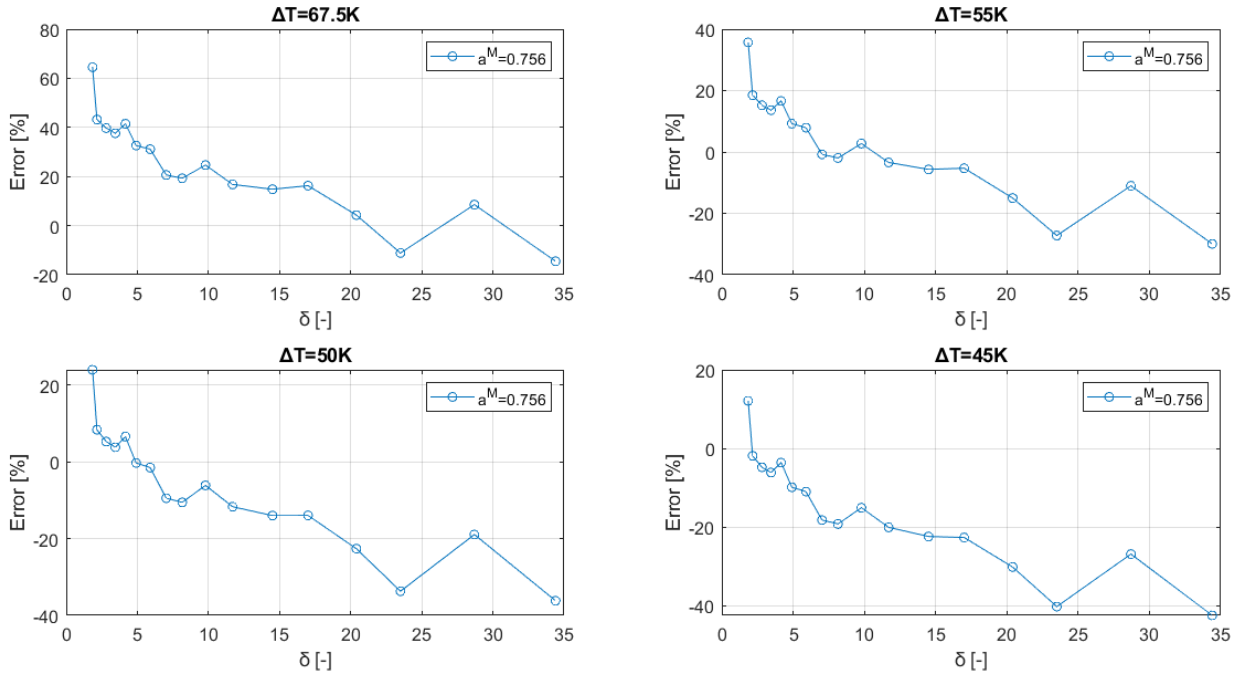

Figure 5.7: Relative difference between experimental and computational mass flow rates with Maxwell boundary conditions for various temperature differences in the case of Ar

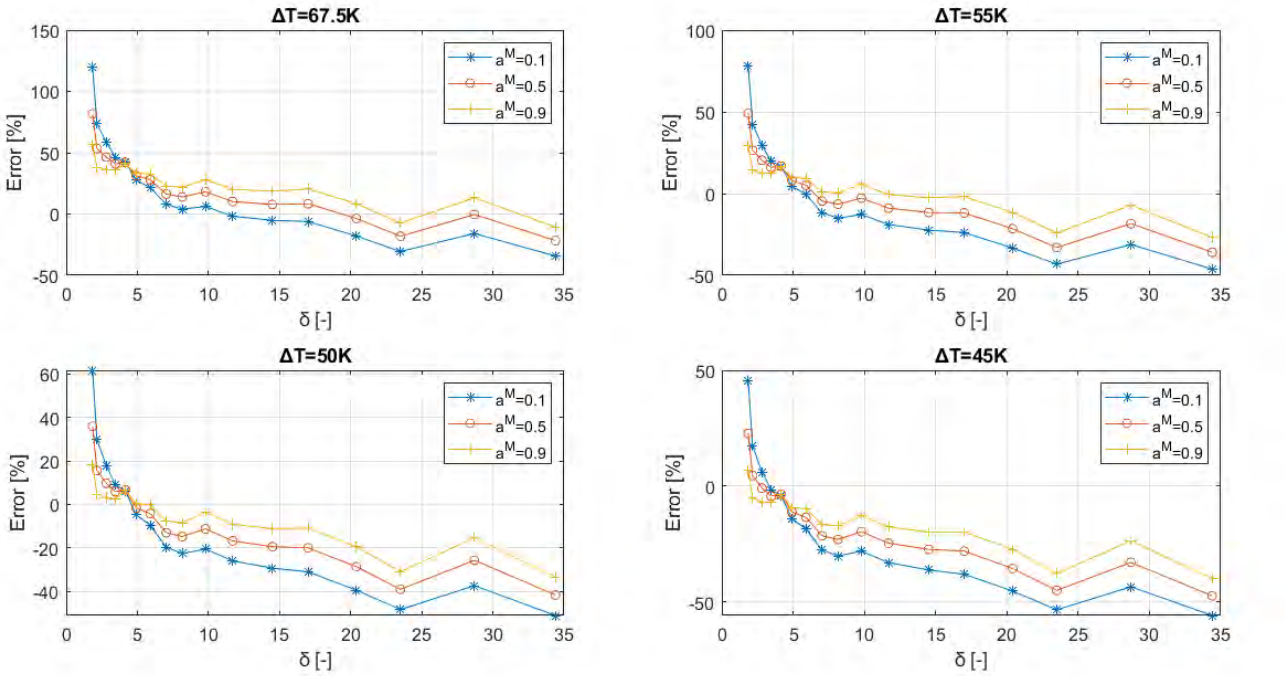

Figure 5.8: Relative difference between experimental and computational mass flow rates with Maxwell boundary conditions for various values of a_T^M and temperature differences in the case of Ar

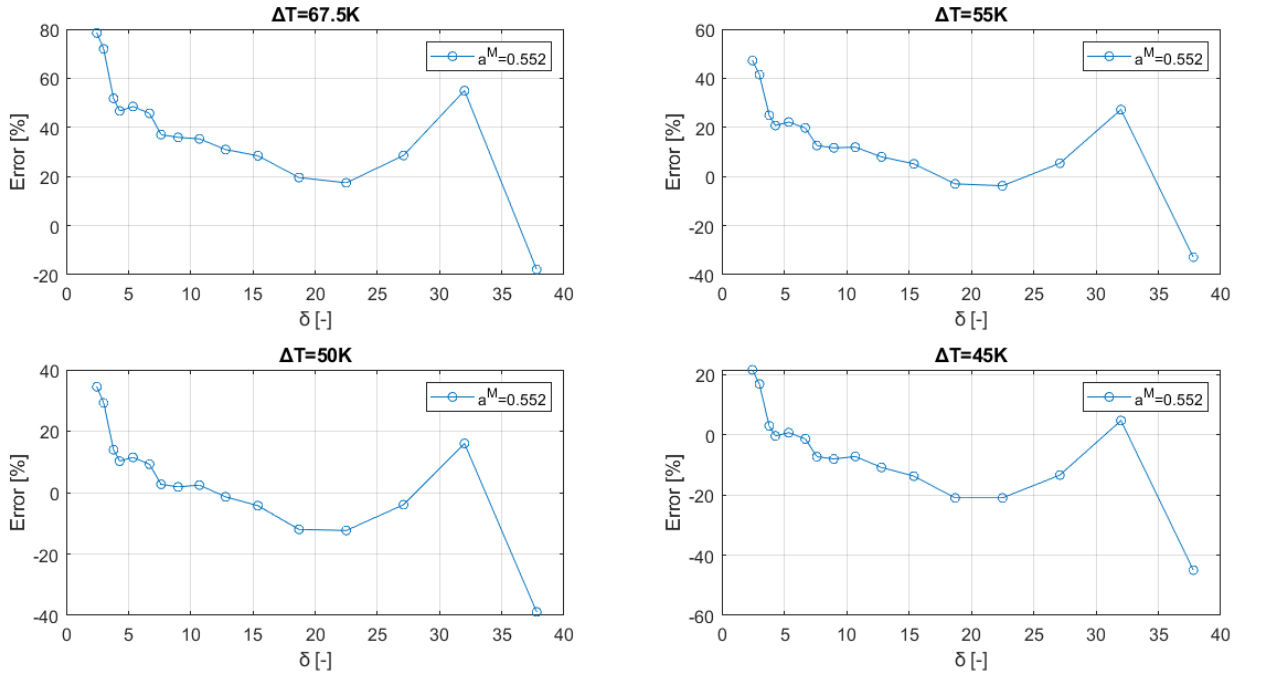

Figure 5.9: Relative difference between experimental and computational mass flow rates with Maxwell boundary conditions for various temperature differences in the case of Kr

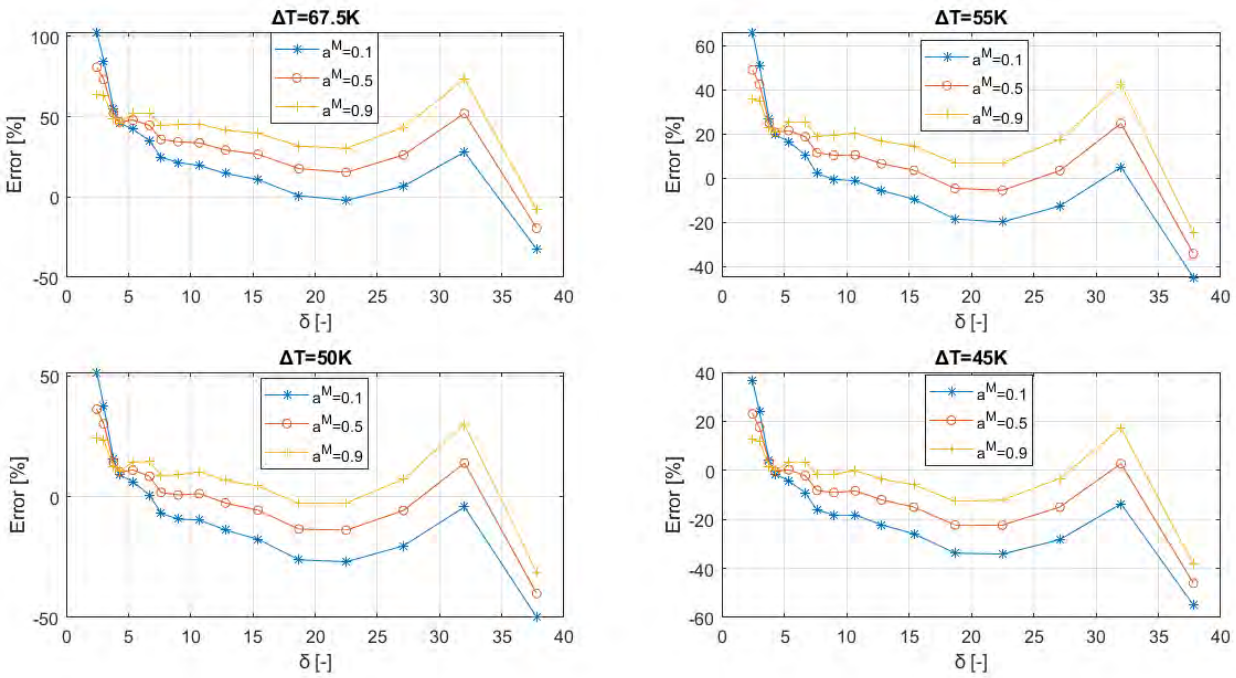

Figure 5.10: Relative difference between experimental and computational mass flow rates with Maxwell boundary conditions for various values of a_T^M and temperature differences in the case of Kr

5.3 Cercignani-Lampis normal energy accommodation coefficient for temperature driven flow

The tangential momentum accommodation coefficient a_t of the CL boundary conditions has already been specified in Section 4.3 for all five gases using the experimental data for the pressure driven flow. These values remain the same and here the objective is to find the values of the normal energy accommodation coefficient a_n in order to obtain the best match between the computed and measured mass flow rates using data regarding the temperature driven flow. The same process as before is followed but now a_t was kept constant and equal with the estimated value for each gas (see Table 4.8), while a_n was altered trying to match the mass flow rates. However, no good agreement is obtainεd even for various values of a_n, including the limiting values $a_n = 0.1$ and 1. The computed mass flow rate was always greater than the corresponding experimental one. Then the coefficient a_t was altered, while keeping $a_n = 1$ and even for the limiting values of a_t the outcome was the same as before (see Tables 5.1-5.5). It is noted that as the value of δ increases the difference between the experimental and numerical values decreases. For Helium the differences are 4.5% and 4% for $a_t = 1.9, a_n = 1\,, \delta = 3.01$ and $a_t = 0.792,\ a_n = 0.1\,, \delta = 7.9,$ respectively. Also, the

effect of a_n on the mass flow rate changes as δ is altered. More specifically, for $\delta < 3$ an increase of a_n results in a decrease of mass flow rate, while for $\delta > 3$ it has the opposite effect.

To gain a better insight of the discrepancies between the experimental and numerical values and in order to find their source, the error along with the mass flow rates for all the experimental values was produced for three different values of a_n, while a_t is equal to the estimated for each gas (Table 4.8) and for three additional temperature differences. In all cases the pressure remains constant and equal to the measured one. The additional temperature differences were all chosen to be smaller than the experimental ones (ΔT=55, 50, 45K) due to the fact that the numerical mass flow rate was always higher than the experimental and so a reduction of the former was necessary. In Figures 5.11-5.20 the respective plots are presented for the case of ΔT=67.5K, while for the other tested temperature difference the figures can be found in Appendix E.

The mass flow rate curves are quite similar to those with the Maxwell boundary conditions and as consequence the same applies for the error curves. The best results are for He not only due to the small deviations in error in the range of $\delta \in [2,12]$, but also because the error is smaller than 10% for $\delta \in [4,11]$ at ΔT=67.5K. For $\delta \approx 1$ the error varies around 35%, but at ΔT=50K this value becomes 3%. Concerning Ne two areas have small deviations in error. The first is for $\delta \in [3,7]$ with an error near 20% and the second one is for $\delta \in [10,18]$ with an error near 10%. The former error gives best results at ΔT=55K, while for the latter case a temperature difference slightly lower than 67.5K is the most suitable. Regarding N_2, again oscillations with small or large amplitudes are noted throughout the error curve. A stabilization of the error is achieved for $\delta \in [5,8]$ and it gets close to zero at ΔT=50K. Also, for $\delta \in [12,17]$ the error is almost constant and is improved at ΔT=55K. In the case of Ar the error varies around 10-15% in the range of $\delta \in [12,17]$ and it is minimized at a temperature difference a bit lower than 67.5K. Apart from this range the curve is filled with oscillations. In the case of Kr, the error stabilizes for $\delta \in [13,23]$ at 30% and approaches zero at a temperature difference between 50-55K. Similar to the Maxwell boundary conditions for the temperature driven flow no general remarks valid in the whole range of gas rarefaction and for any temperature difference can be drawn.

Table 5.1: Mass flow rate comparison at ΔT=67.5K for various values of δ, a_t , a_n for He

Helium									
ΔT=67.5K									
Experimental[1]:		M=2.16E-12		5.07E-12		8.62E-12		1.24E-11	
Numerical									
		δ=0.507		1.38		3.01		7.9	
a_t	a_n	M (kg/s)	M [%]	M (kg/s)	M [%]	M (kg/s)	M [%]	M (kg/s)	M [%]
0.792	0.1	3.73E-12	72.80	6.78E-12	33.76	9.62E-12	11.58	1.29E-11	4.08
0.792	1	3.42E-12	58.18	6.47E-12	27.55	9.6E-12	11.37	1.34E-11	7.81
1.9	1	3.01E-12	39.53	5.83E-12	15.03	9.01E-12	4.50	1.31E-11	5.84
1	1	3.4E-12	57.22	6.43E-12	26.80	9.56E-12	10.93	1.33E-11	7.65
0.1	1	4.42E-12	104.41	7.85E-12	54.87	1.07E-11	24.51	1.39E-11	12.22

Table 5.2: Mass flow rate comparison at ΔT=67.5K for various values of δ, a_t , a_n for Ne

Neon									
ΔT=67.5K									
Experimental[1]:		M=5.15E-12		1.01E-11		1.27E-11		1.76E-11	
Numerical									
		δ=0.914		2.12		3.07		7.51	
a_t	a_n	M (kg/s)	M [%]	M (kg/s)	M [%]	M (kg/s)	M [%]	M (kg/s)	M [%]
0.777	0.1	8.30E-12	61.18	1.32E-11	30.33	1.54E-11	21.60	2.03E-11	15.18
0.777	1	7.75E-12	50.42	1.29E-11	27.52	1.54E-11	21.51	2.10E-11	19.42
1.9	1	6.90E-12	33.92	1.18E-11	17.29	1.45E-11	14.07	2.06E-11	17.01
1	1	7.69E-12	49.30	1.28E-11	26.77	1.54E-11	20.94	2.10E-11	19.20
0.1	1	9.67E-12	87.74	1.49E-11	47.50	1.72E-11	35.47	2.19E-11	24.59

Table 5.3: Mass flow rate comparison at ΔT=67.5K for various values of δ, a_t , a_n for N_2

Nitrogen									
ΔT=67.5K									
Experimental[1]:		M=4.74E-12		6.46E-12		7.93E-12		8.61E-12	
Numerical									
		δ=1.99		3.69		5.46		7.6	
a_t	a_n	M (kg/s)	M [%]	M (kg/s)	M [%]	M (kg/s)	M [%]	M (kg/s)	M [%]
0.789	0.1	7.18E-12	51.44	9.33E-12	44.39	1.06E-11	33.26	1.15E-11	33.25
0.789	1	7.01E-12	47.80	9.40E-12	45.54	1.08E-11	36.53	1.19E-11	37.91
1.9	1	6.43E-12	35.61	8.92E-12	38.08	1.05E-11	32.12	1.16E-11	35.22
1	1	6.97E-12	47.03	9.37E-12	45.04	1.08E-11	36.20	1.19E-11	37.70
0.1	1	8.16E-12	72.25	1.03E-11	59.71	1.15E-11	45.22	1.24E-11	43.82

Table 5.4: Mass flow rate comparison at ΔT=67.5K for various values of δ, a_t , a_n for Ar

Argon									
ΔT=67.5K									
Experimental[1]: M=5.75E-12				7.32E-12		8.01E-12		1.21E-11	
Numerical									
		δ=1.85		2.16		2.81		7.03	
a_t	a_n	M (kg/s)	M [%]	M (kg/s)	M [%]	M (kg/s)	M [%]	M (kg/s)	M [%]
0.79	0.1	8.9E-12	54.75	9.54E-12	30.34	1.07E-11	34.07	1.45E-11	19.72
0.79	1	8.63E-12	50.10	9.34E-12	27.66	1.07E-11	33.13	1.49E-11	23.52
1.9	1	7.88E-12	37.05	8.6E-12	17.48	9.95E-12	24.24	1.46E-11	20.66
1	1	8.58E-12	49.29	9.3E-12	27.02	1.06E-11	32.56	1.49E-11	23.30
0.1	1	1.02E-11	76.90	1.08E-11	47.88	1.2E-11	50.29	1.57E-11	29.54

Table 5.5: Mass flow rate comparison at ΔT=67.5K for various values of δ, a_t , a_n for Kr

Krypton									
ΔT=67.5K									
Experimental[1]: M=6.9E-12				9.08E-12		9.99E-12		1.19E-11	
Numerical									
		δ=2.46		3.8		5.36		8.98	
a_t	a_n	M (kg/s)	M [%]	M (kg/s)	M [%]	M (kg/s)	M [%]	M (kg/s)	M [%]
0.814	0.1	1.12E-11	63.03	1.34E-11	47.35	1.50E-11	49.71	1.70E-11	42.46
0.814	1	1.11E-11	61.12	1.35E-11	48.54	1.53E-11	52.84	1.75E-11	47.35
1.9	1	1.03E-11	49.53	1.28E-11	41.25	1.48E-11	47.86	1.73E-11	45.30
1	1	1.11E-11	60.52	1.35E-11	48.14	1.52E-11	52.54	1.75E-11	47.21
0.1	1	1.27E-11	84.21	1.48E-11	62.70	1.63E-11	62.83	1.81E-11	52.50

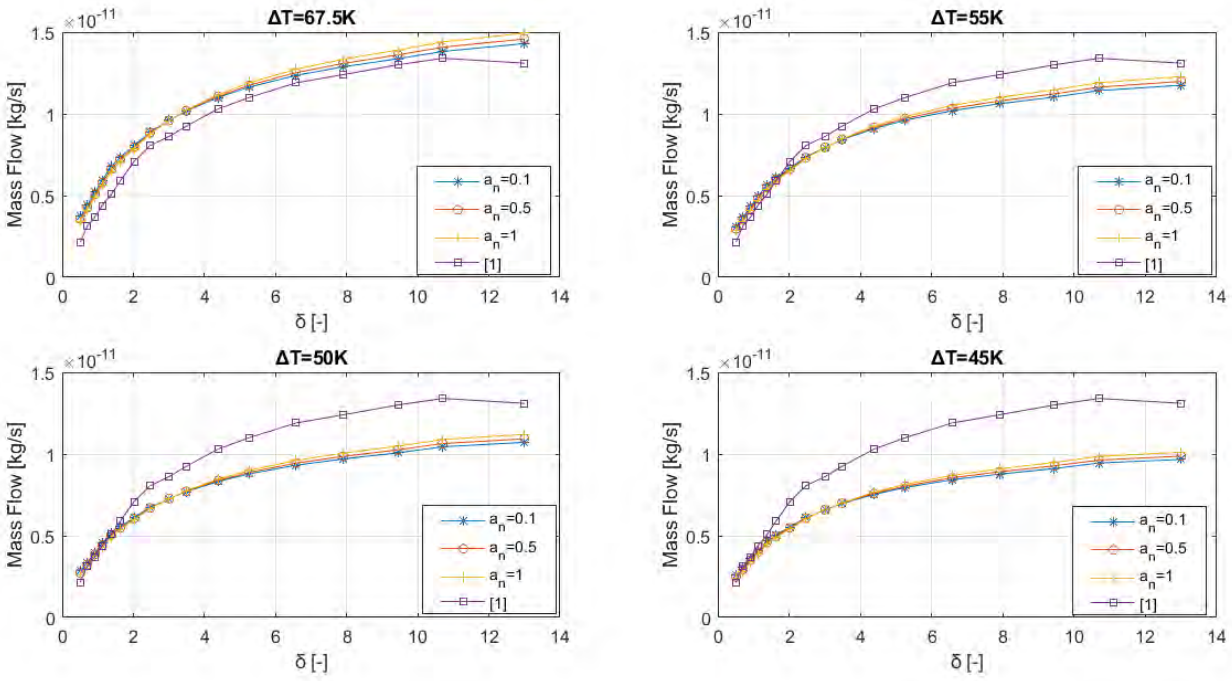

Figure 5.11: Computational and experimental mass flow rates with CL boundary conditions for various values of a_n and temperature differences in the case of He

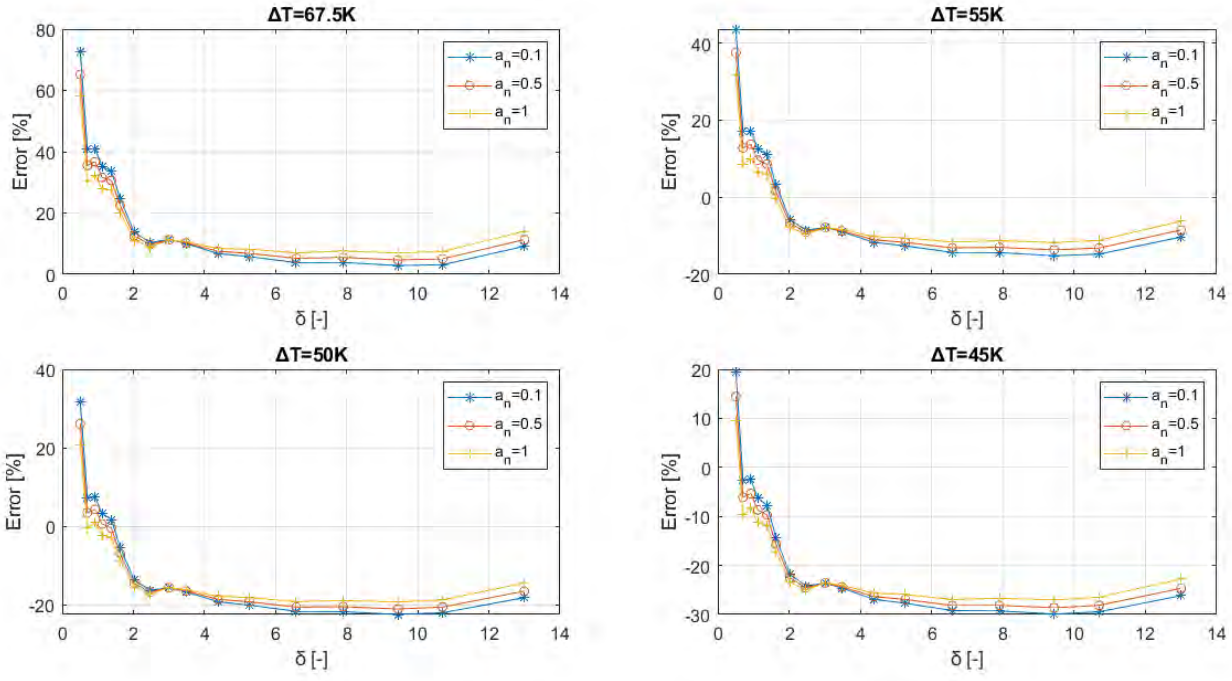

Figure 5.12: Relative difference between computational and experimental mass flow rates with CL boundary conditions for various values of a_n and temperature differences in the case of He

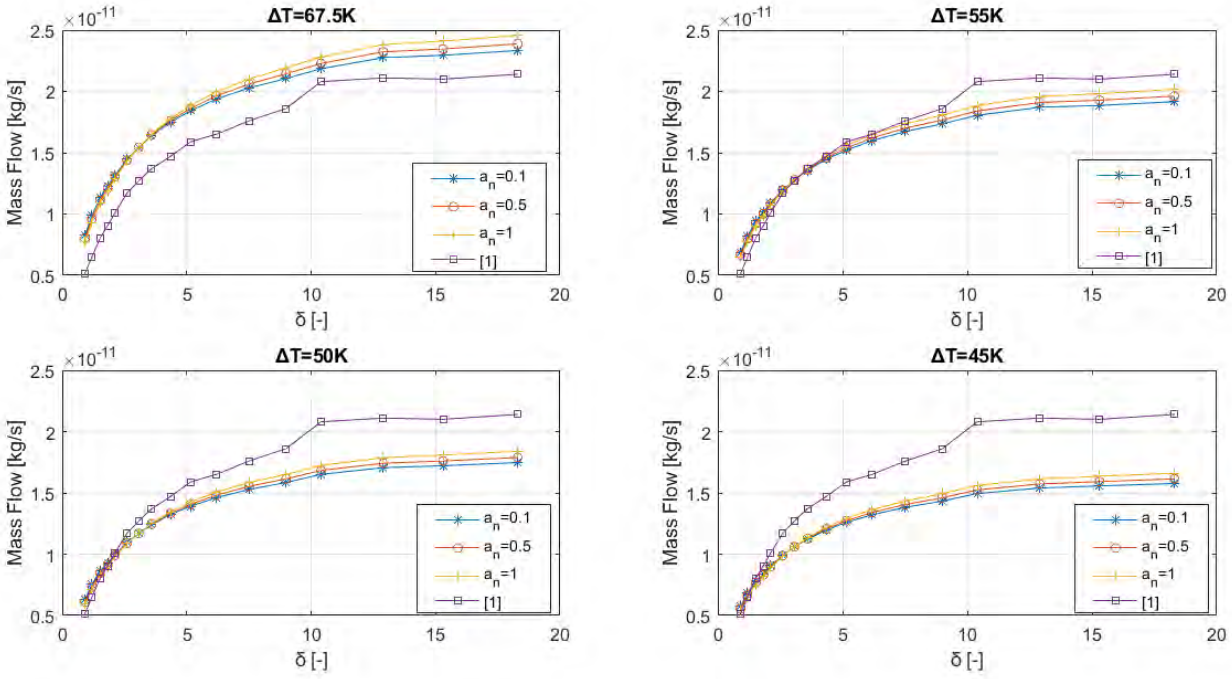

Figure 5.13: Computational and experimental mass flow rates with CL boundary conditions for various values of a_n and temperature differences in the case of Ne

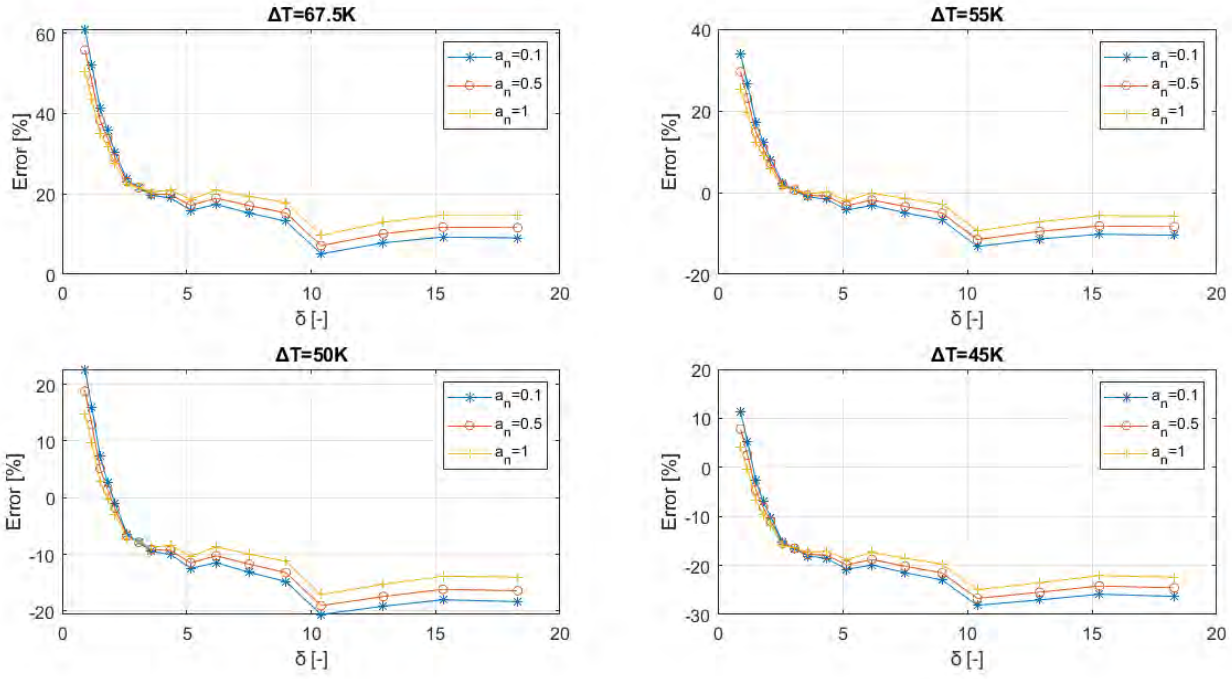

Figure 5.14: Relative difference between computational and experimental mass flow rates with CL boundary conditions for various values of a_n and temperature differences in the case of Ne

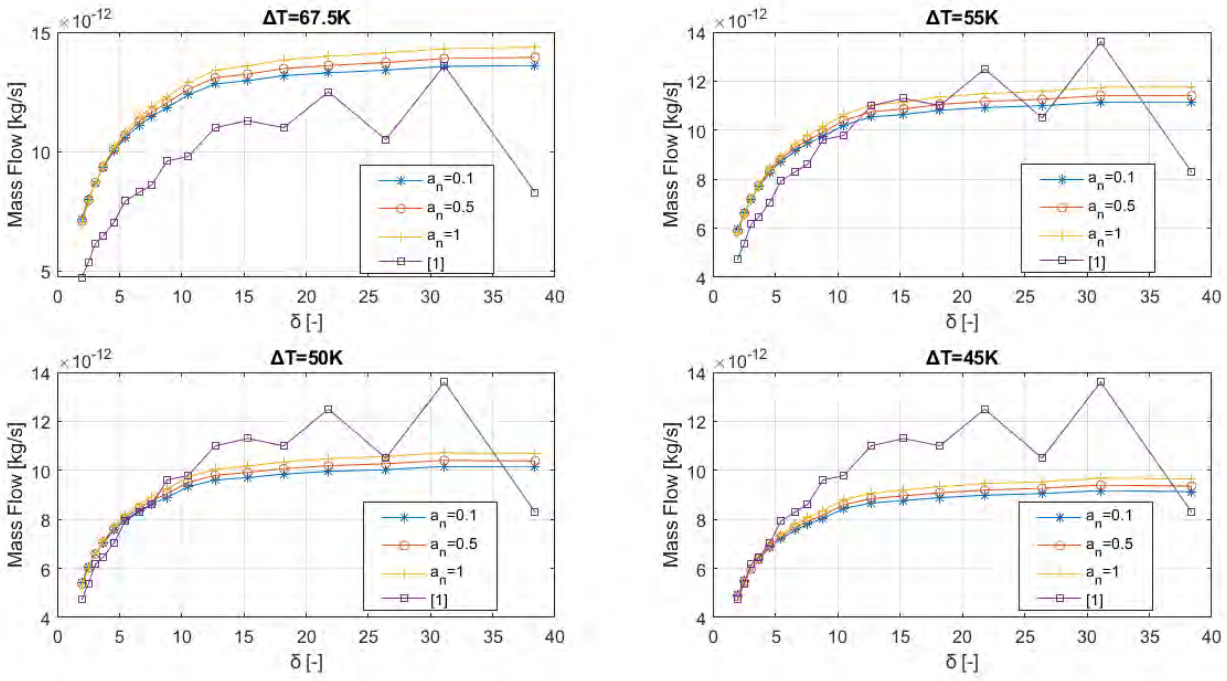

Figure 5.15: Computational and experimental mass flow rates with CL boundary conditions for various values of a_n and temperature differences in the case of N_2

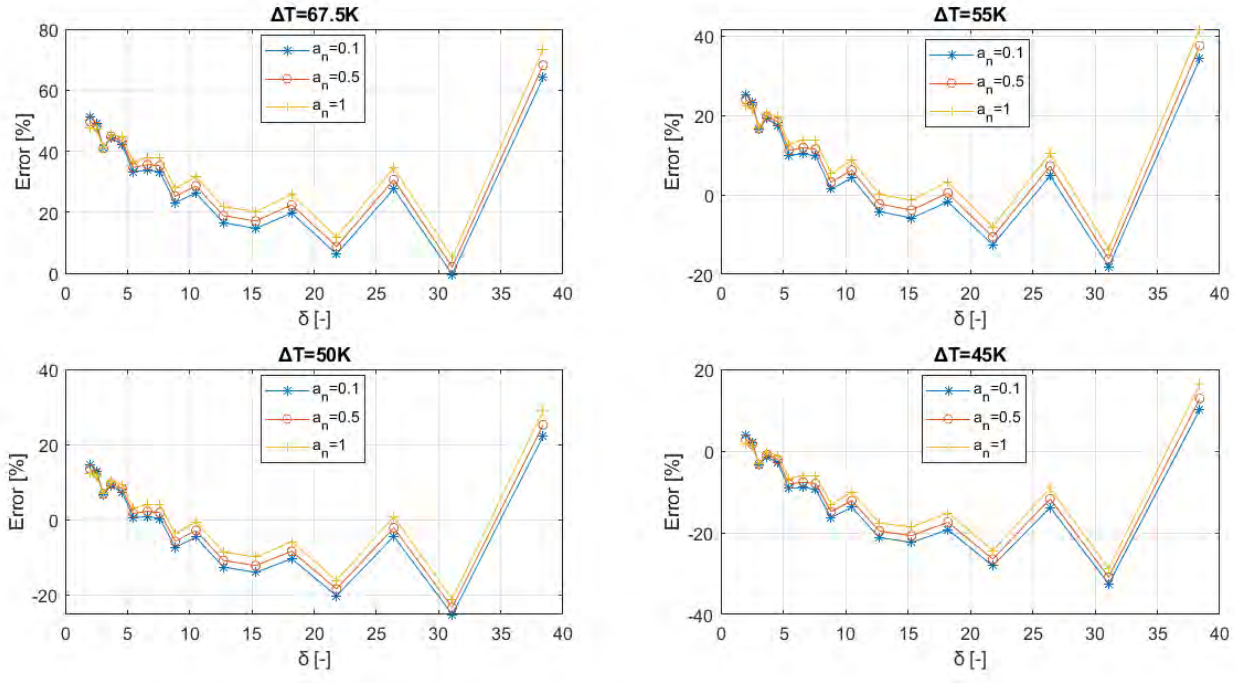

Figure 5.16: Relative difference between computational and experimental mass flow rates with CL boundary conditions for various values of a_n and temperature differences in the case of N_2

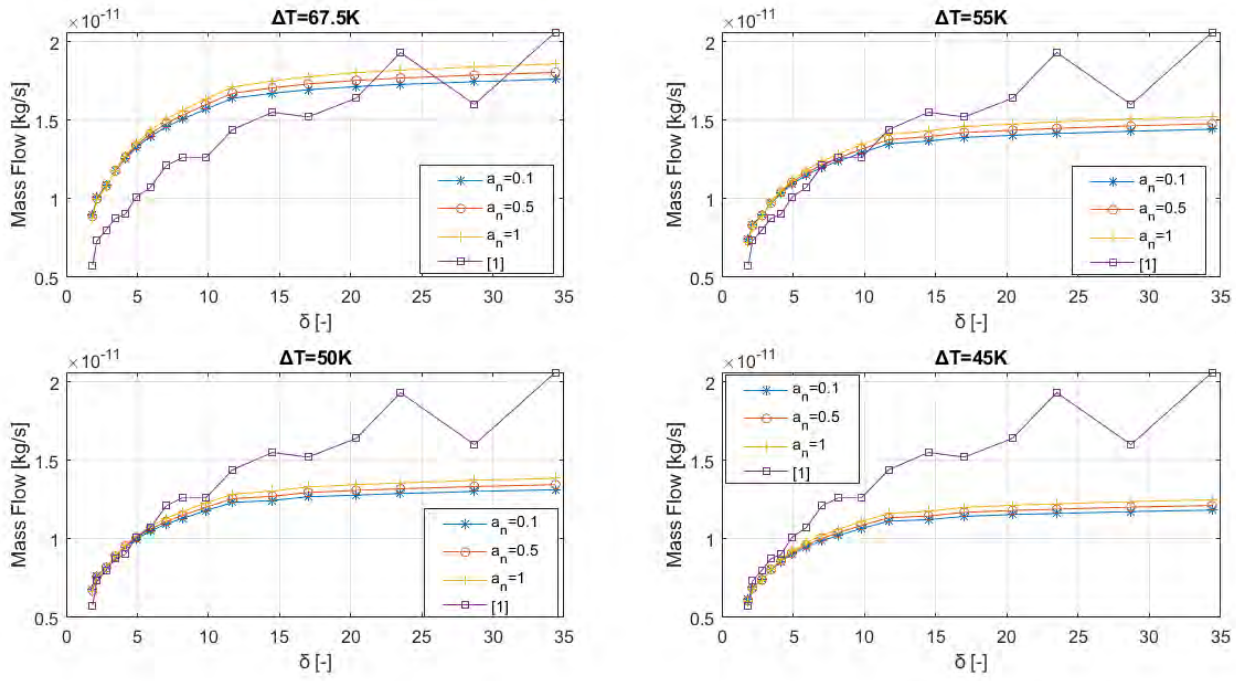

Figure 5.17: Computational and experimental mass flow rates with CL boundary conditions for various values of a_n and temperature differences in the case of Ar

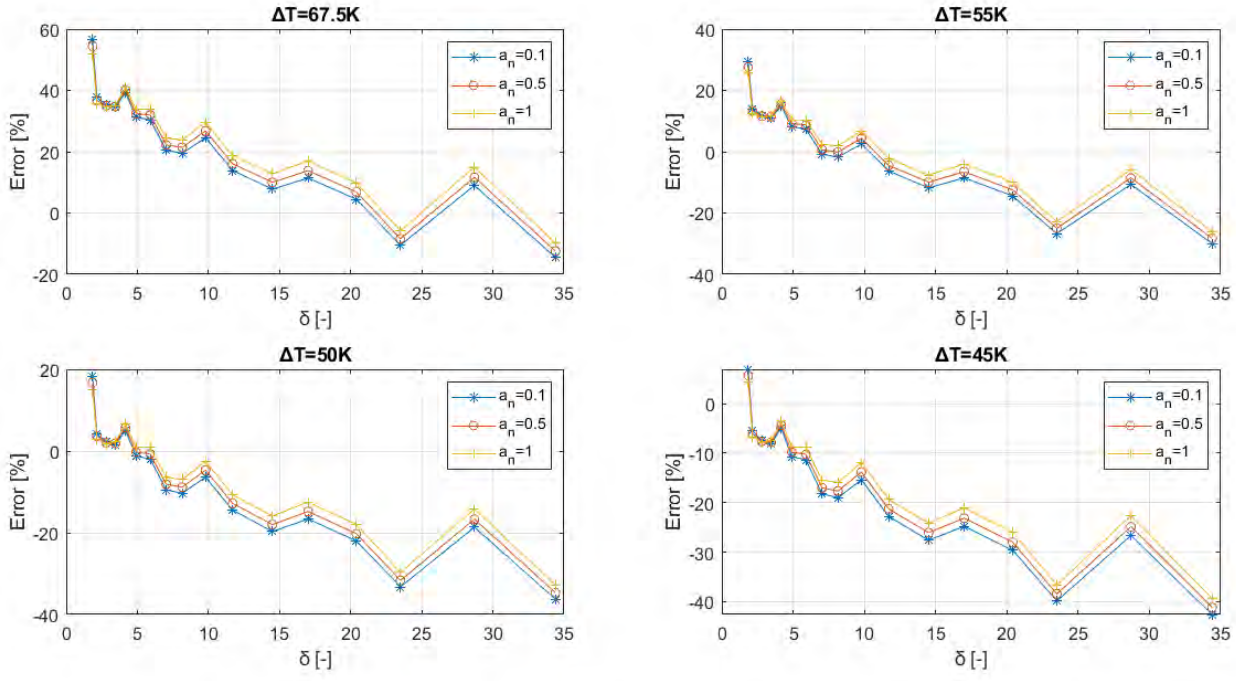

Figure 5.18: Relative difference between computational and experimental mass flow rates with CL boundary conditions for various values of a_n and temperature differences in the case of Ar

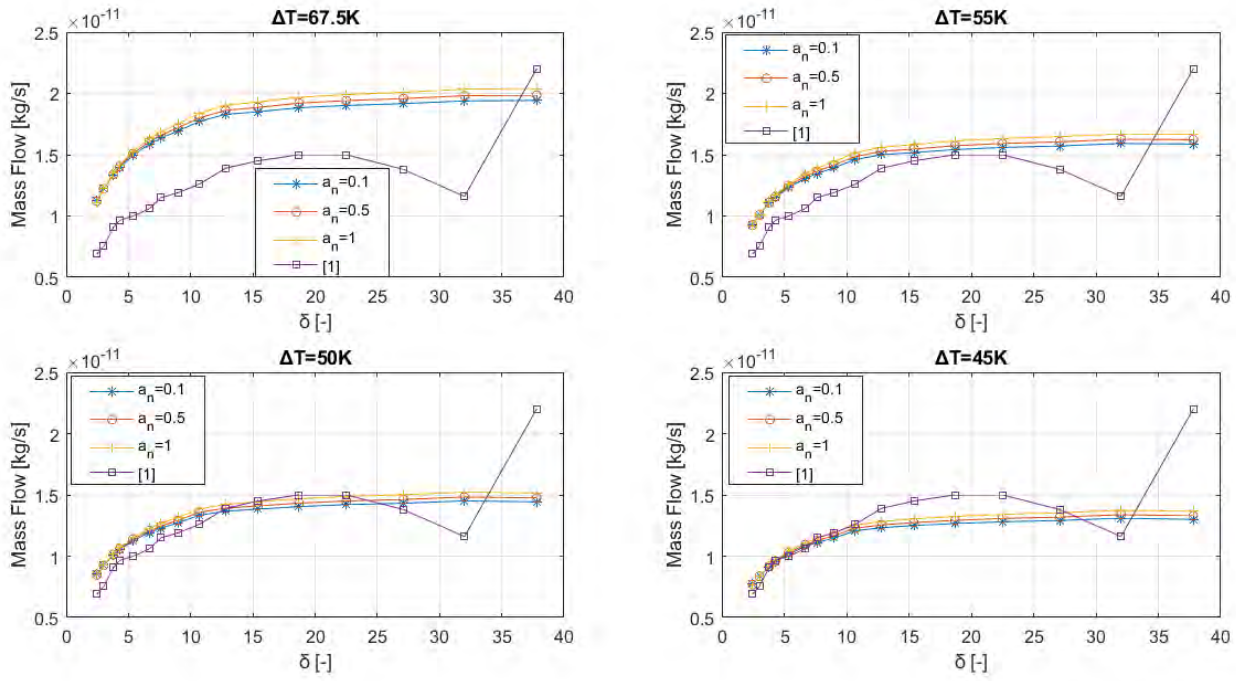

Figure 5.19: Computational and experimental mass flow rates with CL boundary conditions for various values of a_n and temperature differences in the case of Kr

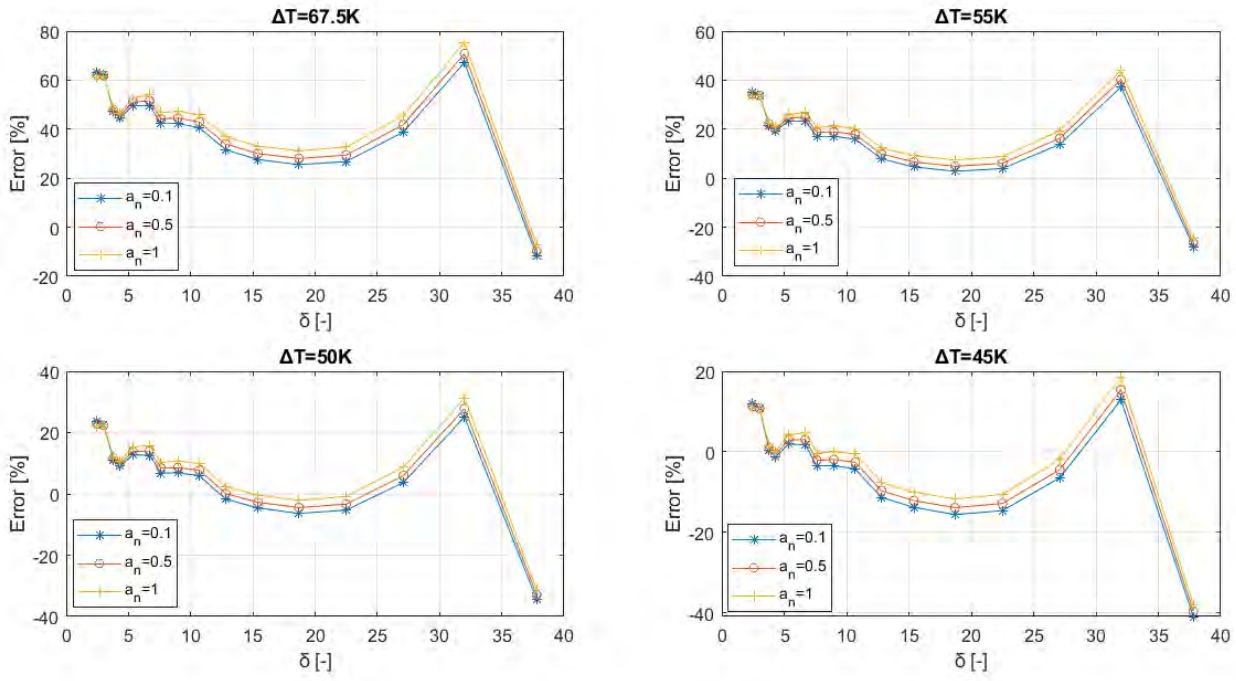

Figure 5.20: Relative difference between computational and experimental mass flow rates with CL boundary conditions for various values of a_n and temperature differences in the case of Kr

Chapter 6 **CONCLUDING REMARKS AND FUTURE WORK**

Summing up, the objective of the thesis is to identify the ACs for pressure and temperature driven flows through long capillaries utilizing experimental and numerical results. The task was partially accomplished since a value for the ACs providing good agreement between numerical and experimental mass flow rates was extracted only for the pressure driven flow for both boundary conditions. As the results showed, for low values of δ a deviation of error smaller than 2% is achieved, while moving to the hydrodynamic regime the effect of the AC gradually diminishes. Yet the lower tested value of δ in pressure driven flow is greater than 10^{-1} ($\delta_{min} = 6$) meaning that the flow takes place in the transition regime, where the number of collisions between molecules is the same order to the collisions between molecules and wall. It would be interesting to see if moving to the free molecular regime, i.e. the flow starts to depend more on the collisions between molecules and wall, the AC could still match the numerical mass flow rate with the respective experimental.

Concerning the temperature driven flow the results were not satisfying, as neither Maxwell or Cercignani-Lampis BCs manage to provide a value for the ACs that matches the numerical and experimental data. Some of the tested gases, Helium and Neon, offer better results than the others, i.e. the error is constant and close to zero for a tested range, but as δ decreases ($\delta < 4$) the error for all gases increases exponentially. This issue impedes the extraction of a value for Helium and Neon. A temperature driven flow experiment is much harder to be conducted since the mass flow rates are two order smaller than to the pressure driven flow, a counterflow due to the pressure difference is arisen and the temperatures on the apparatus must be monitored and controlled. As already mentioned in paragraph 2.5 discrepancies may be expected in temperatures since only the smaller in volume tank was heated. A non-heated reservoir could result in an actual lower temperature difference which would rationalize the lower measured mass flow rate compared to the numerical. Also, another reason for the mismatch between the results may be ought to the measuring time. For a long enough measuring time a counterflow due to pressure difference could have been developed which would result in a lower net mass flow rate. A procedure that could help in

narrowing down the reasons of mismatch and provide another dataset for future comparisons is the thermomolecular pressure difference phenomenon, where the pressure and temperature driven flows cancel each other resulting in a zero net mass flow rate. If the difference between these two was small (order of 10%) then the hypothesis of a smaller temperature difference could be neglected.

REFERENCES

[1]: R. Brancher (2019), Experimental and Numerical Analysis of Interaction between Gas and Solid Surface, PhD Thesis, Universite D'Aix-Marseille.
[2]: J. H. Ferziger, H.G. Kaper (1972), Mathematical theory of transport processes in gases, North-Holland publishing company – Amsterdam, London
[3]: F. Sharipov (2016), Rarefied Gas Dynamics, WILEY-VCH Verlag GmbH & Co. KGaA
[4]: S. Pantazis (2011), Simulation of transport phenomena in condtions far from thermodynamic equilibrium via kinetic theory with applications in vacuum technology and MEMS, PhD Thesis, University of Thessaly.
[5]: F. Sharipov, Application of the Cercignani-Lampis scattering kernel to calculations of rarefied gas flows. I. Plane flow between two parallel plates. European Journal of Mechanics B/Fluids 21 (2002) 113–123
[6]: F. Sharipov, Application of the Cercignani-Lampis scattering kernel to calculations of rarefied gas flows. II. Slip and jump coefficients. European Journal of Mechanics B/Fluids 22 (2003) 133–143
[7]: F. Sharipov, Application of the Cercignani-Lampis scattering kernel to calculations of rarefied gas flows. III. Poiseuille flow and thermal creep through a long tube. European Journal of Mechanics B/Fluids 22 (2003) 145–154
[8]: G. Lopez Quesada, G. Tatsios, D. Valougeorgis, M. Rojas-Cardenas, L. Baldas, C. Barrot and S. Colin (2019), Design Guidelines for Thermally Driven Micropumps of Different Architectures Based on Target Applications via Kinetic Modeling and Simulations.
[9]: S. Pantazis, D. Valougeorgis (2009), The Cercignani-Lampis Boundary Conditions in Rectangular Micro-Channel Flows.
[10]: I. Graur, M.T. Ho (2013), Rarefied gas flow through a long rectangular channel of variable cross section. Vacuum 101 (2014) 328-332
[11]: C. Cercignani & M. Lampis (1971), Kinetic models for gas-surface interactions, Transport Theory and Statistical Physics, 1:2, 101-114
[12]: F. Sharipov, Onsager-Casimir reciprocity relations for open gaseous systems at arbitrary rarefaction. I. General theory for single gas, Physica A 203 (1994) 437-456
[13]: F. Sharipov, Onsager-Casimir reciprocity relations for open gaseous systems at arbitrary rarefaction. II. Application of the theory for single gas, Physica A 203 (1994) 457-485
[14]: S.K. Loyalka, Kinetic theory of thermal transpiration and mechanocaloric effect. I, J. Chem. Phys. 55, 4497 (1971)
[15]: F. Sharipov, Non-isothermal gas flow through rectangular microchannels, J. Micromech. Microeng. 1999;9(4):394e401.
[16]: S. Pantazis, S. Varoutis, V. Hauer, C. Day, D. Valougeorgis, Gas-surface scattering effect on vacuum gas flows through rectangular channels. Vacuum 85 (2011) 1161-1164
[17]: I. Kuščer, Reciprocity in scattering of gas molecules by surfaces. Surface Science 25 (1971) 225-237
[18]: L. Wu, H. Struchtrup, Assessment and development of the gas kinetic boundary condition for the Boltzmann equation. J. Fluid Mech. (2017), vol. 823, pp. 511–537

[19]: M. Epstein, A model of the wall boundary condition in kinetic theory. AIAA J. 5, 1797–1800 (1967)
[20]: T. Klinc, I. Kuščer, Slip coefficients for general gas-surface interaction. The Physics of Fluids 15, 1018 (1972)
[21]: H. Struchtrup, Maxwell boundary condition and velocity dependent accommodation coefficient
[22]: R.G. Lord, Some extensions to the Cercignani-Lampis gas-surface scattering kernel. Physics of Fluids A: Fluid Dynamics 3, 706 (1991)
[23]: K. Ritos, Y. Lihnaropoulos, S. Naris & D. Valougeorgis (2011), Pressure- and Temperature-Driven Flow Through Triangular and Trapezoidal Microchannels, Heat Transfer Engineering, 32:13-14, 1101-1107
[24]: F. Sharipov, V. Seleznev, Data on internal rarefied gas flow. Journal of Physical and Chemical Reference Data 27, 657 (1998)
[25]: T. Edmonds, G.P. Hobson, A study of thermal transpiration using ultrahigh-vacuum techniques, J. Vac. Sci. Technol. 2 (1965) 182–197.
[26]: B.T. Porodnov, P.E. Suetin, S.F. Borisov, V.D. Akinshin, Experimental investigation of rarefied gas flow in different channels, J. Fluid Mech. 64 (1974) 417–437.

APPENDICES

Appendix A. Linearization of Shakhov model

The non-linear model after the assumption of a steady flow is given by,

$$\xi_x \frac{\partial f}{\partial x'} + \xi_y \frac{\partial f}{\partial y'} + \xi_z \frac{\partial f}{\partial z'} = \frac{P}{\mu}(f^S - f) \tag{A.1}$$

To continue, in the non-linear model VDF is replaced by the perturbed distribution

$$\tilde{\xi} \frac{\partial \left[f_0 \left(1 + h x_p + x_p \frac{z'}{H} \right) \right]}{\partial \tilde{r}} = \frac{P}{\mu} \left(f^S - f^0 \left(1 + h x_p + x_p \frac{z'}{H} \right) \right) \Rightarrow \tag{A.3}$$

$$\begin{aligned} \Rightarrow \zeta_x v_0 \frac{x_P}{H} f^0 \frac{\partial h}{\partial x} + \zeta_y v_0 \frac{x_P}{H} f^0 \frac{\partial h}{\partial y} + \zeta_z v_0 \frac{x_P}{H} f^0 = \\ = \frac{P}{\mu} f^0 \left[1 + \frac{N - N_0}{N_0} + \frac{2\tilde{\xi}\tilde{u}}{2RT_0} + \frac{T - T_0}{T_0} \left(\left(\frac{\xi}{\sqrt{2RT_0}} \right)^2 - \frac{3}{2} \right) \right. \\ \left. + \frac{2}{15} \frac{m}{N_0 (k_B T)^2} \tilde{\xi} \tilde{Q} \left(\left(\frac{\xi}{\sqrt{2RT_0}} \right)^2 - \frac{5}{2} \right) - 1 - h x_p - x_p \frac{z'}{H} \right] \Rightarrow \end{aligned} \tag{A.4}$$

$$\begin{aligned} \zeta_x \frac{\partial h}{\partial x} + \zeta_y \frac{\partial h}{\partial y} = \frac{PH}{\mu v_0} \left[\frac{N - N_0}{N_0 x_P} + \frac{2\tilde{\xi}\tilde{u}}{2RT_0 x_P} + \frac{T - T_0}{T_0 x_P} \left(\left(\frac{\xi}{\sqrt{2RT_0}} \right)^2 - \frac{3}{2} \right) \right. \\ \left. + \frac{2}{15} \frac{m}{N_0 (k_B T)^2} \tilde{\xi} \tilde{Q} \left(\left(\frac{\xi}{\sqrt{2RT_0}} \right)^2 - \frac{5}{2} \right) - h - \frac{z'}{H} \right] - \zeta_z \Rightarrow \end{aligned} \tag{A.5}$$

$$\zeta_x \frac{\partial h}{\partial x} + \zeta_y \frac{\partial h}{\partial y} = \delta \left[2\zeta_z v_z + \frac{4}{15} \zeta_z q_z \left(\zeta^2 - \frac{5}{2} \right) - h \right] - \zeta_z \tag{A.6}$$

where: $x = \frac{x'}{H}$, $y = \frac{y'}{H}$, $\zeta = \frac{\xi}{v_0}$, $v_0 = \sqrt{2RT_0}$, $\rho = \frac{N-N_0}{N_0 x_P} = \frac{z'}{H}$, $\tau = \frac{T-T_0}{T_0 x_P} = 0$,

$$v = (0,0,v_z),\ \ q = (0,0,q_z),\ \ v_z = \frac{u_z}{v_0 x_p},\ \ q_z = \frac{Q_z}{v_0 P_0 x_p}$$

Projections

Inserting projections (A.6) & (A.16) to eq. (A.5)

$$\varphi = \frac{1}{\sqrt{\pi}} \int_{-\infty}^{+\infty} \zeta_z\, h e^{-{\zeta_z}^2} d\zeta_z \tag{A.7}$$

$$\zeta_x \frac{\partial \varphi}{\partial x} + \zeta_y \frac{\partial \varphi}{\partial y} = \frac{1}{\sqrt{\pi}} \int_{-\infty}^{+\infty} \zeta_z \left[\delta \left(2\zeta_z v_z + \frac{4}{15} \zeta_z q_z \left(\zeta^2 - \frac{5}{2} \right) - h \right) - \zeta_z \right] e^{-{\zeta_z}^2} d\zeta \tag{A.8}$$

For simplicity the integral is broken in four parts

$$I_1 = \frac{1}{\sqrt{\pi}} \int_{-\infty}^{+\infty} \zeta_z\, 2\zeta_z v_z e^{-{\zeta_z}^2} d\zeta_z = \frac{2v_z}{\sqrt{\pi}} \int_{-\infty}^{+\infty} {\zeta_z}^2\, e^{-{\zeta_z}^2} d\zeta_z = v_z \tag{A.9}$$

$$I_2 = \frac{1}{\sqrt{\pi}} \int_{-\infty}^{+\infty} \zeta_z \frac{4}{15} \zeta_z q_z \left(\zeta^2 - \frac{5}{2} \right) e^{-{\zeta_z}^2} d\zeta_z = \tag{A.10}$$

$$= \frac{4q_z}{15\sqrt{\pi}} \int_{-\infty}^{+\infty} \left({\zeta_z}^2 {\zeta_x}^2 + {\zeta_z}^2 {\zeta_y}^2 + {\zeta_z}^4 - {\zeta_z}^2 \frac{5}{2} \right) e^{-{\zeta_z}^2} d\zeta_z \Rightarrow \tag{A.11}$$

$$I_2 = \frac{2}{15} q_z ({\zeta_x}^2 + {\zeta_y}^2 - 1) \tag{A.12}$$

$$I_3 = \frac{1}{\sqrt{\pi}} \int_{-\infty}^{+\infty} \zeta_z\, h e^{-{\zeta_z}^2} d\zeta = \varphi \tag{A.13}$$

$$I_4 = \frac{1}{\sqrt{\pi}} \int_{-\infty}^{+\infty} \zeta_z\, \zeta_z e^{-{\zeta_z}^2} d\zeta = \frac{1}{2} \tag{A.14}$$

The deduced equation is

$$\zeta_x \frac{\partial \varphi}{\partial x} + \zeta_y \frac{\partial \varphi}{\partial y} = \delta[I_1 + I_2 + I_3] - I_4 \Rightarrow \quad \text{(A.15)}$$

$$\zeta_x \frac{\partial \varphi}{\partial x} + \zeta_y \frac{\partial \varphi}{\partial y} = \delta\left[v_z + \frac{2}{15} q_z\left({\zeta_x}^2 + {\zeta_y}^2 - 1\right) - \varphi\right] - \frac{1}{2} \quad \text{(A.16)}$$

Same steps are followed for the other projection

$$\psi = \frac{1}{\sqrt{\pi}} \int_{-\infty}^{+\infty} {\zeta_z}^3 h e^{-{\zeta_z}^2} d\zeta_z \quad \text{(A.17)}$$

$$\zeta_x \frac{\partial \psi}{\partial x} + \zeta_y \frac{\partial \psi}{\partial y} = \frac{1}{\sqrt{\pi}} \int_{-\infty}^{+\infty} {\zeta_z}^3 \left[\delta\left(2\zeta_z v_z + \frac{4}{15}\zeta_z q_z\left(\zeta^2 - \frac{5}{2}\right) - h\right) - \zeta_z\right] e^{-{\zeta_z}^2} d\zeta_z \quad \text{(A.18)}$$

Calculating the integrals,

$$I_1 = \frac{1}{\sqrt{\pi}} \int_{-\infty}^{+\infty} {\zeta_z}^3 2\zeta_z v_z e^{-{\zeta_z}^2} d\zeta_z = \frac{2v_z}{\sqrt{\pi}} \int_{-\infty}^{+\infty} {\zeta_z}^5 e^{-{\zeta_z}^2} d\zeta_z = \frac{3}{2} v_z \quad \text{(A.19)}$$

$$I_2 = \frac{1}{\sqrt{\pi}} \int_{-\infty}^{+\infty} {\zeta_z}^3 \frac{4}{15}\zeta_z q_z \left(\zeta^2 - \frac{5}{2}\right) e^{-{\zeta_z}^2} d\zeta_z = \quad \text{(A.20)}$$

$$= \frac{4q_z}{15\sqrt{\pi}} \int_{-\infty}^{+\infty} \left({\zeta_z}^4 {\zeta_x}^2 + {\zeta_z}^4 {\zeta_y}^2 + {\zeta_z}^6 - {\zeta_z}^4 \frac{5}{2}\right) e^{-{\zeta_z}^2} d\zeta_z \Rightarrow \quad \text{(A.21)}$$

$$I_2 = \frac{1}{5} q_z ({\zeta_x}^2 + {\zeta_y}^2) \quad \text{(A.22)}$$

$$I_3 = \frac{1}{\sqrt{\pi}} \int_{-\infty}^{+\infty} {\zeta_z}^3 h e^{-{\zeta_z}^2} d\zeta_z = \psi \quad \text{(A.23)}$$

$$I_4 = \frac{1}{\sqrt{\pi}} \int_{-\infty}^{+\infty} {\zeta_z}^3 \zeta_z e^{-{\zeta_z}^2} d\zeta_z = \frac{3}{4} \quad \text{(A.24)}$$

The deduced equation is

$$\zeta_x \frac{\partial \psi}{\partial x} + \zeta_y \frac{\partial \psi}{\partial y} = \delta[I_1 + I_2 + I_3] - I_4 \tag{A.25}$$

$$\zeta_x \frac{\partial \psi}{\partial x} + \zeta_y \frac{\partial \psi}{\partial y} = \delta\left[\frac{3}{2} v_z + \frac{1}{5} q_z\left({\zeta_x}^2 + {\zeta_y}^2\right) - \psi\right] - \frac{3}{4} \tag{A.26}$$

Macroscopic Velocity

The macroscopic velocity is given by

$$u_z = \frac{1}{N} \iiint_{-\infty}^{+\infty} \xi_z f d\tilde{\boldsymbol{\xi}} \tag{A.27}$$

The VDF is substituted by the perturbed distribution

$$u_z = \frac{1}{N} \iiint_{-\infty}^{+\infty} \xi_z f_0 \left(1 + h x_p + x_p \frac{z'}{H}\right) d\tilde{\boldsymbol{\xi}} \tag{A.28}$$

Again, the integral is broken

$$I_1 = \frac{1}{N} \iiint_{-\infty}^{+\infty} \xi_z \frac{N_0}{(2\pi RT)^{3/2}} \, exp\left[-\frac{\xi^2}{2RT_0}\right] d\tilde{\boldsymbol{\xi}} = 0 \tag{A.29}$$

$$I_2 = \frac{1}{N} \iiint_{-\infty}^{+\infty} \xi_z \, h x_p \frac{N_0}{(2\pi RT)^{\frac{3}{2}}} \, exp\left[-\frac{\xi^2}{2RT_0}\right] d\tilde{\boldsymbol{\xi}} = \tag{A.30}$$

$$= \frac{1}{N} \frac{N_0}{(2\pi RT)^{\frac{3}{2}}} x_p \iiint_{-\infty}^{+\infty} \xi_z \, h \, exp\left[-\frac{\xi^2}{2RT_0}\right] d\tilde{\boldsymbol{\xi}} \Rightarrow \tag{A.31}$$

$$I_2 = \frac{v_0 x_p}{\pi^{3/2}} \int_{-\infty}^{+\infty} \zeta_z \, h e^{-\zeta^2} d\tilde{\boldsymbol{\zeta}} \tag{A.32}$$

$$I_3 = \frac{1}{N} \iiint_{-\infty}^{+\infty} \xi_z \frac{N_0}{(2\pi RT)^{3/2}} \, exp\left[-\frac{\xi^2}{2RT_0}\right] x_p \frac{z'}{H} d\tilde{\boldsymbol{\xi}} = 0 \tag{A.33}$$

The bulk velocity becomes

$$u_z = I_1 + I_2 + I_3 = \frac{v_0 x_p}{\pi^{\frac{3}{2}}} \iiint_{-\infty}^{+\infty} \zeta_z \, h e^{-\zeta^2} d\tilde{\boldsymbol{\zeta}} \tag{A.34}$$

The dimensionless macroscopic velocity v_z is introduced

$$v_z = \frac{u_z}{v_0 x_p} = \frac{1}{\pi^{3/2}} \iiint_{-\infty}^{+\infty} \zeta_z \, h e^{-\zeta^2} d\tilde{\boldsymbol{\zeta}} \tag{A.35}$$

$$v_z = \frac{1}{\pi} \iint_{-\infty}^{+\infty} \left[\frac{1}{\sqrt{\pi}} \int_{-\infty}^{+\infty} \zeta_z \, h e^{-{\zeta_z}^2} d\zeta_z \right] e^{-{\zeta_x}^2} e^{-{\zeta_y}^2} d\zeta_x d\zeta_y \tag{A.35}$$

$$v_z = \frac{1}{\pi} \iint_{-\infty}^{+\infty} \varphi \, e^{-{\zeta_x}^2} e^{-{\zeta_y}^2} d\zeta_x d\zeta_y \tag{A.36}$$

Heat Flux

The heat flux is given by

$$Q_z = \frac{m}{2} \iiint_{-\infty}^{+\infty} (\xi_z - u_z) \left(\tilde{\boldsymbol{\xi}} - \tilde{\boldsymbol{u}} \right)^2 f d\tilde{\boldsymbol{\xi}} \tag{A.37}$$

The VDF is substituted by the perturbed distribution

$$Q_z = \frac{m}{2} \iiint_{-\infty}^{+\infty} (\xi_z - u_z) \left(\tilde{\boldsymbol{\xi}} - \tilde{\boldsymbol{u}} \right)^2 f_0 (1 + h x_P + x_P) d\tilde{\boldsymbol{\xi}} \tag{A.38}$$

$$Q_z = \frac{m}{2} \iiint_{-\infty}^{+\infty} (\xi_z - u_z) \left(\tilde{\xi} - \tilde{u} \right)^2 \frac{N_0}{(2\pi RT)^{\frac{3}{2}}} \, exp\left(-\frac{\xi^2}{2RT_0} \right) \left(1 + h x_P + x_P \frac{z'}{H} \right) d\tilde{\boldsymbol{\xi}} \tag{A.39}$$

$$\begin{aligned} Q_z = \frac{m}{2} \frac{N_0}{(2\pi RT_0)^{\frac{3}{2}}} \iiint_{-\infty}^{+\infty} (\xi_z - v_z v_0 x_P) \left[{\xi_x}^2 + {\xi_y}^2 \right. \\ \left. + (\xi_z - v_z v_0 x_P)^2 \right] exp\left(-\frac{\xi^2}{2RT_0} \right) \left(1 + h x_P + x_P \frac{z'}{H} \right) d\tilde{\boldsymbol{\xi}} \end{aligned} \tag{A.40}$$

$$Q_z = \frac{m}{2}\frac{N_0}{(2\pi R T_0)^{\frac{3}{2}}} {v_0}^6 \iiint_{-\infty}^{+\infty} (\zeta_z - v_z x_P)\left[{\zeta_x}^2 + {\zeta_y}^2 + (\zeta_z - v_z x_P)^2\right] exp[-\zeta^2]\left(1 + h x_P + x_P \frac{z'}{H}\right) d\tilde{\boldsymbol{\zeta}} \tag{A.41}$$

Manipulating the integrals,

$$I_1 = \iiint_{-\infty}^{+\infty} (\zeta_z - v_z x_P)\left[{\zeta_x}^2 + {\zeta_y}^2 + (\zeta_z - v_z x_P)^2\right] exp(-\zeta^2) d\tilde{\boldsymbol{\zeta}} = \tag{A.42}$$

$$= \iiint_{-\infty}^{+\infty} (\zeta_z - v_z x_P)\left[{\zeta_x}^2 + {\zeta_y}^2 + {\zeta_z}^2 - 2\zeta_z v_z x_P + {v_z}^2 {x_P}^2\right] exp(-\zeta^2) d\tilde{\boldsymbol{\zeta}} = \tag{A.43}$$

$$= \iiint_{-\infty}^{+\infty} \zeta_z\left({\zeta_x}^2 + {\zeta_y}^2 + {\zeta_z}^2\right) - 2\zeta_z v_z x_P - v_z x_P\left({\zeta_x}^2 + {\zeta_y}^2 + {\zeta_z}^2\right) + 2\zeta_z {v_z}^2 {x_P}^2\, exp(-\zeta^2) d\tilde{\boldsymbol{\zeta}} \Rightarrow \tag{A.44}$$

$$I_1 = -\frac{5}{2}\pi^{3/2} v_z x_P \tag{A.45}$$

$$I_2 = \iiint_{-\infty}^{+\infty} (\zeta_z - v_z x_P)\left[{\zeta_x}^2 + {\zeta_y}^2 + (\zeta_z - v_z x_P)^2\right] h x_P\, exp(-\zeta^2) d\tilde{\boldsymbol{\zeta}} = \tag{A.46}$$

$$= \iiint_{-\infty}^{+\infty} (\zeta_z x_P - v_z {x_P}^2)\left({\zeta_x}^2 + {\zeta_y}^2 + {\zeta_z}^2 - 2\zeta_z v_z x_P + {v_z}^2 {x_P}^2\right) h\, exp(-\zeta^2) d\tilde{\boldsymbol{\zeta}} = \tag{A.47}$$

$$= \iiint_{-\infty}^{+\infty} \zeta_z x_P\left({\zeta_x}^2 + {\zeta_y}^2 + {\zeta_z}^2 - 2\zeta_z v_z x_P\right) h\, exp(-\zeta^2) d\tilde{\boldsymbol{\zeta}} = \tag{A.48}$$

$$= \iiint_{-\infty}^{+\infty} \zeta_z\left[\left({\zeta_x}^2 + {\zeta_y}^2 + {\zeta_z}^2\right) x_P - 2\zeta_z v_z {x_P}^2\right] h\, exp(-\zeta^2) d\tilde{\boldsymbol{\zeta}} \Rightarrow \tag{A.49}$$

$$I_2 = \iiint_{-\infty}^{+\infty} \zeta_z x_P \left({\zeta_x}^2 + {\zeta_y}^2 + {\zeta_z}^2\right) h\, exp(-\zeta^2) d\tilde{\boldsymbol{\zeta}} \tag{A.50}$$

$$I_3 = \iiint_{-\infty}^{+\infty} (\zeta_z - v_z x_P) \left[{\zeta_x}^2 + {\zeta_y}^2 + (\zeta_z - v_z x_P)^2\right] x_T \frac{z'}{H}\, exp(-\zeta^2) d\tilde{\boldsymbol{\zeta}} = \tag{A.51}$$

$$= \iiint_{-\infty}^{+\infty} (\zeta_z x_P - v_z {x_P}^2) \left({\zeta_x}^2 + {\zeta_y}^2 + {\zeta_z}^2 - 2\zeta_z v_z x_P + {v_z}^2 {x_P}^2\right) \frac{z'}{H}\, exp(-\zeta^2) d\tilde{\boldsymbol{\zeta}} \tag{A.52}$$

$$= \iiint_{-\infty}^{+\infty} \zeta_z \left[\left({\zeta_x}^2 + {\zeta_y}^2 + {\zeta_z}^2\right) x_P - 2\zeta_z v_z {x_P}^2\right] \frac{z'}{H}\, exp(-\zeta^2) d\tilde{\boldsymbol{\zeta}} = \tag{A.53}$$

$$= \iiint_{-\infty}^{+\infty} \zeta_z x_P \left({\zeta_x}^2 + {\zeta_y}^2 + {\zeta_z}^2\right) \frac{z'}{H}\, exp(-\zeta^2) d\tilde{\boldsymbol{\zeta}} \Rightarrow \tag{A.54}$$

$$I_3 = 0 \tag{A.55}$$

The heat flux becomes

$$Q_z = \frac{m}{2} \frac{N_0}{(2\pi RT)^{\frac{3}{2}}} {v_0}^6 (I_1 + I_2 + I_3) \tag{A.56}$$

$$Q_z = \frac{m}{2} \frac{N_0}{(2\pi RT_0)^{\frac{3}{2}}} {v_0}^6 x_P \left[-\frac{5}{2}\pi^{\frac{3}{2}} v_z + \iiint_{-\infty}^{+\infty} \zeta_z \left({\zeta_x}^2 + {\zeta_y}^2 + {\zeta_z}^2\right) h\, exp(-\zeta^2) d\tilde{\boldsymbol{\zeta}}\right] = \tag{A.57}$$

$$= \frac{m}{2} \frac{N_0}{(2\pi RT_0)^{\frac{3}{2}}} {v_0}^6 x_P \left[-\frac{5}{2} \iiint_{-\infty}^{+\infty} \zeta_z\ h\, exp(-\zeta^2) d\zeta + \iiint_{-\infty}^{+\infty} \zeta_z\, \zeta^2\, h\, exp(-\zeta^2) d\tilde{\boldsymbol{\zeta}}\right] \Rightarrow \tag{A.58}$$

$$Q_z = \frac{m}{2} \frac{N_0}{(2\pi RT_0)^{\frac{3}{2}}} {v_0}^6 x_P \iiint_{-\infty}^{+\infty} \zeta_z \left(\zeta^2 - \frac{5}{2}\right) h\, exp(-\zeta^2) d\tilde{\boldsymbol{\zeta}} \tag{A.59}$$

$$Q_z = \frac{P_0 v_0 x_P}{\pi^{\frac{3}{2}}} \iiint_{-\infty}^{+\infty} \zeta_z \left(\zeta^2 - \frac{5}{2}\right) h\, exp(-\zeta^2) d\tilde{\boldsymbol{\zeta}} \tag{A.60}$$

where,

$$\frac{m}{2}\frac{N_0}{(2\pi RT_0)^{\frac{3}{2}}}{v_0}^6 x_P = \frac{m}{2}\frac{P_0}{k_B T_0 (2RT_0)^{\frac{3}{2}}}\frac{{v_0}^6}{\pi^{3/2}}x_P = \frac{P_0}{2RT_0(2RT_0)^{\frac{3}{2}}}\frac{{v_0}^6}{\pi^{3/2}}x_P = \frac{P_0 v_0 x_P}{\pi^{3/2}} \quad 2.60)$$

Inserting the dimensionless heat flux,

$$q_z = \frac{Q_z}{P_0 v_0 x_P} = \frac{1}{\pi^{\frac{3}{2}}}\iiint_{-\infty}^{+\infty} \zeta_z \left(\zeta^2 - \frac{5}{2}\right) h\, exp(-\zeta^2) d\tilde{\boldsymbol{\zeta}} \Rightarrow \quad \text{(A.61)}$$

$$q_z = \frac{1}{\pi}\iint_{-\infty}^{+\infty} \left[\psi + \left({\zeta_x}^2 + {\zeta_y}^2 - \frac{5}{2}\right)\varphi\right] exp(-\zeta^2) d\zeta_x d\zeta_y \quad \text{(A.62)}$$

For the temperature driven flow the same steps are followed for the other perturbed distribution.

Appendix B. Linearization of Cercignani-Lampis boundary conditions

Projection φ

$$\phi^{+}\left(\pm\frac{1}{2}, y, \zeta_x, \zeta_y\right) = \frac{1}{\sqrt{\pi}}\int Ah^{-}\zeta_z \exp(-\zeta_z^2)\, d\zeta_z = \tag{B.1}$$

$$= \frac{1}{\sqrt{\pi}}\int \left[\iiint\limits_{\zeta_n{}'<0} R\left(-\tilde{\boldsymbol{\zeta}} \to -\tilde{\boldsymbol{\zeta}}'\right) h^{-}\left(\tilde{\boldsymbol{\zeta}}'\right) d\tilde{\zeta}'\right] \zeta_z \exp(-\zeta_z^2)\, d\zeta_z = \tag{B.2}$$

$$= \frac{1}{\sqrt{\pi}} \iiint\limits_{\zeta_n{}'<0} \left[\int R\left(-\tilde{\boldsymbol{\zeta}} \to -\tilde{\boldsymbol{\zeta}}'\right)\zeta_z \exp(-\zeta_z^2) d\zeta_z\right] h^{-}\left(\tilde{\zeta}'\right) d\tilde{\boldsymbol{\zeta}}' = \tag{B.3}$$

$$= \frac{1}{\sqrt{\pi}} \iiint\limits_{\zeta_n{}'<0} E\left(\tilde{\boldsymbol{\zeta}}' \to \tilde{\boldsymbol{\zeta}}\right) h^{-}\left(\tilde{\boldsymbol{\zeta}}'\right) d\tilde{\boldsymbol{\zeta}}' \tag{B.4}$$

To simplify the equation the internal integral $E\left(\tilde{\boldsymbol{\zeta}}' \to \tilde{\boldsymbol{\zeta}}\right)$ is manipulated

$$E\left(\tilde{\boldsymbol{\zeta}}' \to \tilde{\boldsymbol{\zeta}}\right) = \int R\left(-\tilde{\boldsymbol{\zeta}} \to -\tilde{\boldsymbol{\zeta}}'\right)\zeta_z \exp(-\zeta_z^2) d\zeta_z \tag{B.5}$$

$$E\left(\tilde{\boldsymbol{\zeta}}' \to \tilde{\boldsymbol{\zeta}}\right) = R_n(-\zeta_n \to -\zeta_n{}')R_y\left(-\zeta_y \to -\zeta_y{}'\right) \int R_z(-\zeta_z \to -\zeta_z{}')\, \zeta_z \exp(-\zeta_z^2) d\zeta_z \tag{B.6}$$

$$I = \frac{E\left(\tilde{\zeta}' \to \zeta_p\right)}{R_n(-\zeta_n \to -\zeta_n{}')R_y\left(-\zeta_y \to -\zeta_y{}'\right)} = \int R_z(-\zeta_z \to -\zeta_z{}')\, \zeta_z \exp(-\zeta_z^2) d\zeta_z \tag{B.7}$$

$$I = \frac{1}{\sqrt{\pi(1-a^2)}}\int exp\left[-\frac{(a\zeta_z - \zeta_z{}')^2}{1-a^2}\right]\zeta_z \exp(-\zeta_z^2)\, d\zeta_z \tag{B.8}$$

$$I = \frac{1}{\sqrt{\pi(1-a^2)}}\int exp\left[-\frac{a^2{\zeta_z}^2 - 2a\zeta_z\zeta_z{}' + \zeta_z{}'^2 + {\zeta_z}^2(1-a^2)}{1-a^2}\right]\zeta_z d\zeta_z \tag{B.9}$$

$$I = \frac{1}{\sqrt{\pi(1-a^2)}}\int exp\left[-\frac{{\zeta_z}^2 - 2a\zeta_z\zeta_z{}' + \zeta_z{}'^2}{1-a^2}\right]\zeta_z d\zeta_z \tag{B.10}$$

$$I = \frac{1}{\sqrt{\pi(1-a^2)}} \exp\left(-\zeta_z'^2\right) \int exp\left[-\frac{\zeta_z{}^2 - 2a\zeta_z\zeta_z{}' + a\zeta_z{}'^2}{1-a^2}\right] \zeta_z d\zeta_z \qquad \text{(B.11)}$$

$$I = \frac{1}{\sqrt{\pi(1-a^2)}} \exp\left(-\zeta_z'^2\right) \int exp\left[-\frac{(\zeta_z - a\zeta_z{}')^2}{1-a^2}\right] \zeta_z d\zeta_z \qquad \text{(B.12)}$$

Consider,

$$\zeta_z{}^* = \frac{\zeta_z}{\sqrt{1-a^2}}, \qquad \zeta_z{}^{**} = \zeta_z{}^* - a\zeta_z{}'^*, \qquad a = (1-a_t), \qquad \text{(B.13)}$$

And substitute into eq. (B.12)

$$I = \frac{\sqrt{(1-a^2)}}{\sqrt{\pi}} \exp\left(-\zeta_z'^2\right) \int exp[-(\zeta_z{}^* - a\zeta_z{}'^*)^2]\, \zeta_z{}^* d\zeta_z{}^* = \qquad \text{(B.14)}$$

$$= \frac{\sqrt{(1-a^2)}}{\sqrt{\pi}} \exp\left(-\zeta_z'^2\right) \int exp\left[-\zeta_z{}^{**2}\right] (\zeta_z{}^{**} + a\zeta_z{}'^*) d\zeta_z{}^{**} \Rightarrow \qquad \text{(B.15)}$$

$$I = a\zeta_z{}' \exp\left(-\zeta_z'^2\right) \qquad \text{(B.16)}$$

The deduced equation is

$$\phi^+ = \frac{a}{\sqrt{\pi}} \iiint\limits_{\zeta_n{}'<0} R_n(-\zeta_n \to -\zeta_n{}') R_y\left(-\zeta_y \to -\zeta_y{}'\right) \zeta_z{}' \exp\left(-\zeta_z'^2\right) h^-\left(\tilde{\zeta}'\right) d\tilde{\zeta}' = \qquad \text{(B.17)}$$

$$= \frac{2a}{a_n\sqrt{\pi a_t(2-a_t)}} \iint\limits_{\zeta_n{}'<0} \phi^-\left(\pm\frac{1}{2}, y, \zeta_x{}', \zeta_y{}'\right) \zeta_z{}' \exp\left[-\frac{\zeta_z'^2 + (1-a_n)\zeta_n{}^2}{a_n} - \frac{\left(a\zeta_y - \zeta_y{}'\right)^2}{1-\alpha^2}\right] I_0\left(\frac{2\sqrt{1-a_n}\zeta_n\zeta_n{}'}{a_n}\right) d\zeta_n{}' d\zeta_y{}' \Rightarrow \qquad \text{(B.18)}$$

$$\phi^{+}=\frac{2(1-a_t)}{a_n\sqrt{\pi a_t(2-a_t)}}\iint\limits_{\zeta_n{}'<0}\phi^{-}\left(\pm\frac{1}{2},y,\zeta_x{}',\zeta_y{}'\right)\zeta_z{}'\exp\left[-\frac{\zeta_z{}'^2+(1-a_n)\zeta_n{}^2}{a_n}\right.$$
$$\left.-\frac{\left((1-a_t)\zeta_y-\zeta_y{}'\right)^2}{a_t(2-a_t)}\right]I_0\left(\frac{2\sqrt{1-a_n}\zeta_n\zeta_n{}'}{a_n}\right)d\zeta_n{}'d\zeta_y{}' \tag{B.19}$$

Projection ψ

$$\psi^{+}\left(\pm\frac{1}{2},y,\zeta_x,\zeta_y\right)=\frac{1}{\sqrt{\pi}}\int Ah^{-}\zeta_z{}^3\exp(-\zeta_z^2)\,d\zeta_z= \tag{B.20}$$

$$=\frac{1}{\sqrt{\pi}}\int\left[\iiint\limits_{\zeta_n{}'<0}R\left(-\tilde{\boldsymbol{\zeta}}\rightarrow-\tilde{\boldsymbol{\zeta}}'\right)h^{-}\left(\tilde{\boldsymbol{\zeta}}'\right)d\tilde{\boldsymbol{\zeta}}'\right]\zeta_z{}^3\exp(-\zeta_z^2)\,d\zeta_z= \tag{B.21}$$

$$=\frac{1}{\sqrt{\pi}}\iiint\limits_{\zeta_n{}'<0}\left[\int R\left(-\tilde{\boldsymbol{\zeta}}\rightarrow-\tilde{\boldsymbol{\zeta}}'\right)\zeta_z{}^3\exp(-\zeta_z^2)d\zeta_z\right]h^{-}\left(\tilde{\boldsymbol{\zeta}}'\right)d\tilde{\boldsymbol{\zeta}}'= \tag{B.22}$$

$$=\frac{1}{\sqrt{\pi}}\iiint\limits_{\zeta_n{}'<0}E\left(\tilde{\boldsymbol{\zeta}}'\rightarrow\tilde{\boldsymbol{\zeta}}\right)h^{-}\left(\tilde{\boldsymbol{\zeta}}'\right)d\tilde{\boldsymbol{\zeta}}' \tag{B.23}$$

Again $E\left(\tilde{\boldsymbol{\zeta}}'\rightarrow\tilde{\boldsymbol{\zeta}}\right)$, is manipulated first.

$$E\left(\tilde{\boldsymbol{\zeta}}'\rightarrow\tilde{\boldsymbol{\zeta}}\right)=\int R\left(-\tilde{\boldsymbol{\zeta}}\rightarrow-\tilde{\boldsymbol{\zeta}}'\right)\zeta_z{}^3\exp(-\zeta_z^2)d\zeta_z= \tag{B.24}$$

$$=R_n(-\zeta_n\rightarrow-\zeta_n{}')R_y\left(-\zeta_y\rightarrow-\zeta_y{}'\right)\int R_z(-\zeta_z\rightarrow-\zeta_z{}')\,\zeta_z{}^3\exp(-\zeta_z^2)d\zeta_z \tag{B.25}$$

$$I=\frac{E\left(\tilde{\boldsymbol{\zeta}}'\rightarrow\tilde{\boldsymbol{\zeta}}\right)}{R_n(-\zeta_n\rightarrow-\zeta_n{}')R_y\left(-\zeta_y\rightarrow-\zeta_y{}'\right)}=\int R_z(-\zeta_z\rightarrow-\zeta_z{}')\,\zeta_z{}^3\exp(-\zeta_z^2)d\zeta_z \tag{B.26}$$

$$I=\frac{1}{\sqrt{\pi(1-a^2)}}\int exp\left[-\frac{(a\zeta_z-\zeta_z{}')^2}{1-a^2}\right]\zeta_z{}^3\exp(-\zeta_z^2)\,d\zeta_z \tag{B.27}$$

$$I = \frac{1}{\sqrt{\pi(1-a^2)}} \int exp\left[-\frac{a^2{\zeta_z}^2 - 2a\zeta_z\zeta_z' + \zeta_z'^2 + {\zeta_z}^2(1-a^2)}{1-a^2}\right] {\zeta_z}^3 d\zeta_z \quad \text{(B.28)}$$

$$I = \frac{1}{\sqrt{\pi(1-a^2)}} \int exp\left[-\frac{{\zeta_z}^2 - 2a\zeta_z\zeta_z' + \zeta_z'^2}{1-a^2}\right] {\zeta_z}^3 d\zeta_z \quad \text{(B.29)}$$

$$I = \frac{1}{\sqrt{\pi(1-a^2)}} \exp\left(-\zeta_z'^2\right) \int exp\left[-\frac{{\zeta_z}^2 - 2a\zeta_z\zeta_z' + a\zeta_z'^2}{1-a^2}\right] {\zeta_z}^3 d\zeta_z \quad \text{(B.30)}$$

$$I = \frac{1}{\sqrt{\pi(1-a^2)}} \exp\left(-\zeta_z'^2\right) \int exp\left[-\frac{(\zeta_z - a\zeta_z')^2}{1-a^2}\right] {\zeta_z}^3 d\zeta_z \quad \text{(B.31)}$$

Consider,

$$\zeta_z{}^* = \frac{\zeta_z}{\sqrt{1-a^2}}, \qquad \zeta_z{}^{**} = \zeta_z{}^* - a\zeta_z'^*, \qquad a = (1-a_t) \quad \text{(B.34)}$$

And substitute in eq. (B.31)

$$I = \frac{\left(\sqrt{(1-a^2)}\right)^3}{\sqrt{\pi}} \exp\left(-\zeta_z'^2\right) \int exp\left[-\zeta_z{}^{**2}\right] (\zeta_z{}^{**} + a\zeta_z'^*)^3 d\zeta_z{}^{**} \quad \text{(B.35)}$$

$$I = \zeta_z'^3 \exp\left(-\zeta_z'^2\right) a^3 + \zeta_z' \exp\left(-\zeta_z'^2\right) \frac{3}{2} \alpha(1-\alpha^2) \quad \text{(B.36)}$$

The deduced equation is

$$\psi^+ = \frac{1}{\sqrt{\pi}} \iiint\limits_{\zeta_n'<0} R_n(-\zeta_n \to -\zeta_n') R_y\left(-\zeta_y \to -\zeta_y'\right) \left[\zeta_z'^3 \exp\left(-\zeta_z'^2\right) a^3 + \zeta_z' \exp\left(-\zeta_z'^2\right) \frac{3}{2} \alpha(1-\alpha^2)\right] h^-(\tilde{\zeta}') d\tilde{\zeta}' \quad \text{(B.37)}$$

$$\psi^+ = \frac{a^3}{\sqrt{\pi}} \iint\limits_{\zeta_n'<0} R_n(-\zeta_n \to -\zeta_n') R_y\left(-\zeta_y \to -\zeta_y'\right) \psi^-\left(\pm\frac{1}{2}, y, \zeta_x, \zeta_y\right) d\zeta_n' d\zeta_y' + \quad \text{(B.38)}$$

$$+ \frac{3}{2} \frac{\alpha(1-\alpha^2)}{\sqrt{\pi}} \iint\limits_{\zeta_n'<0} R_n(-\zeta_n \to -\zeta_n') R_y\left(-\zeta_y \to -\zeta_y'\right) \varphi^-\left(\pm\frac{1}{2}, y, \zeta_x, \zeta_y\right) d\zeta_n' d\zeta_y'$$

$$\psi^{+} = \frac{(1-a_t)^3}{\sqrt{\pi}} \iint\limits_{\zeta_n{}'<0} R_n(-\zeta_n \to -\zeta_n{}')R_y(-\zeta_y \to -\zeta_y{}')\ \psi^{-}\left(\pm\frac{1}{2}, y, \zeta_x, \zeta_y\right) d\zeta_n{}' d\zeta_y{}' +$$

(B.39)

$$+\frac{3a_t(1-a_t)}{2}\frac{(2-a_t)}{\sqrt{\pi}} \iint\limits_{\zeta_n{}'<0} R_n(-\zeta_n \to -\zeta_n{}')R_y(-\zeta_y \to -\zeta_y{}')\ \varphi^{-}\left(\pm\frac{1}{2}, y, \zeta_x, \zeta_y\right) d\zeta_n{}' d\zeta_y{}'$$

For the temperature driven flow the same procedure is followed.

Appendix C. Results for the Maxwell mass flow rate graphs (ΔT=67.5K)

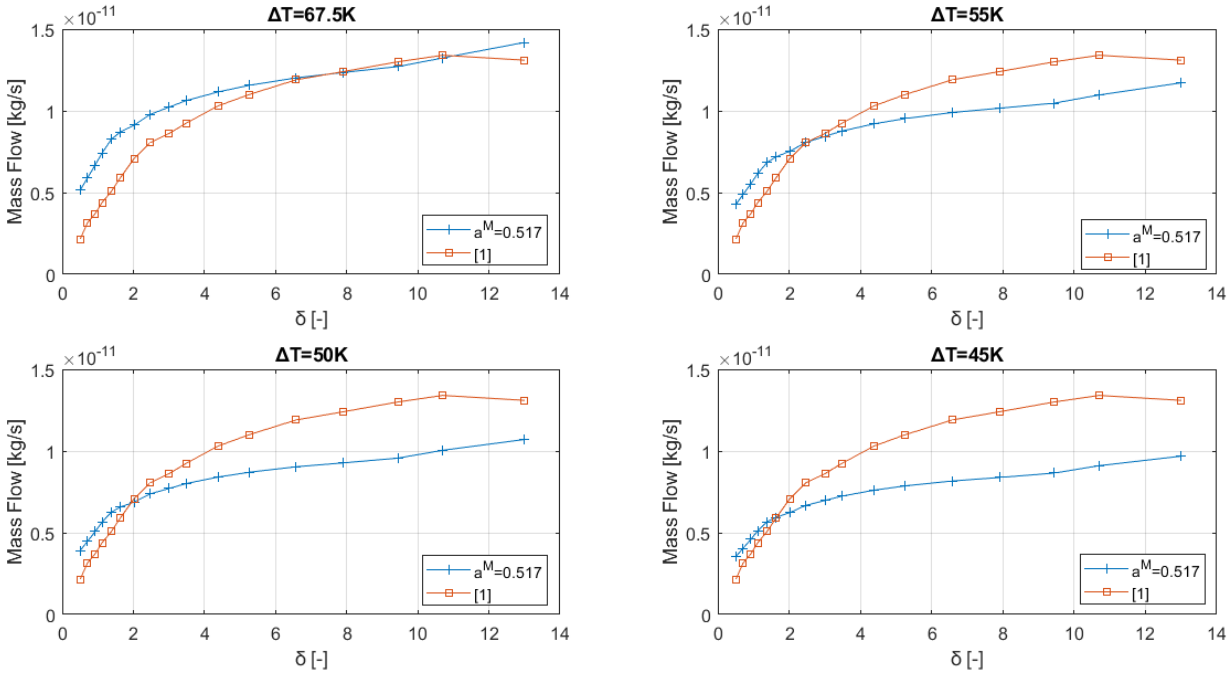

Figure C.1: Computational and experimental mass flow rates with Maxwell boundary conditions for various temperature differences in the case of He

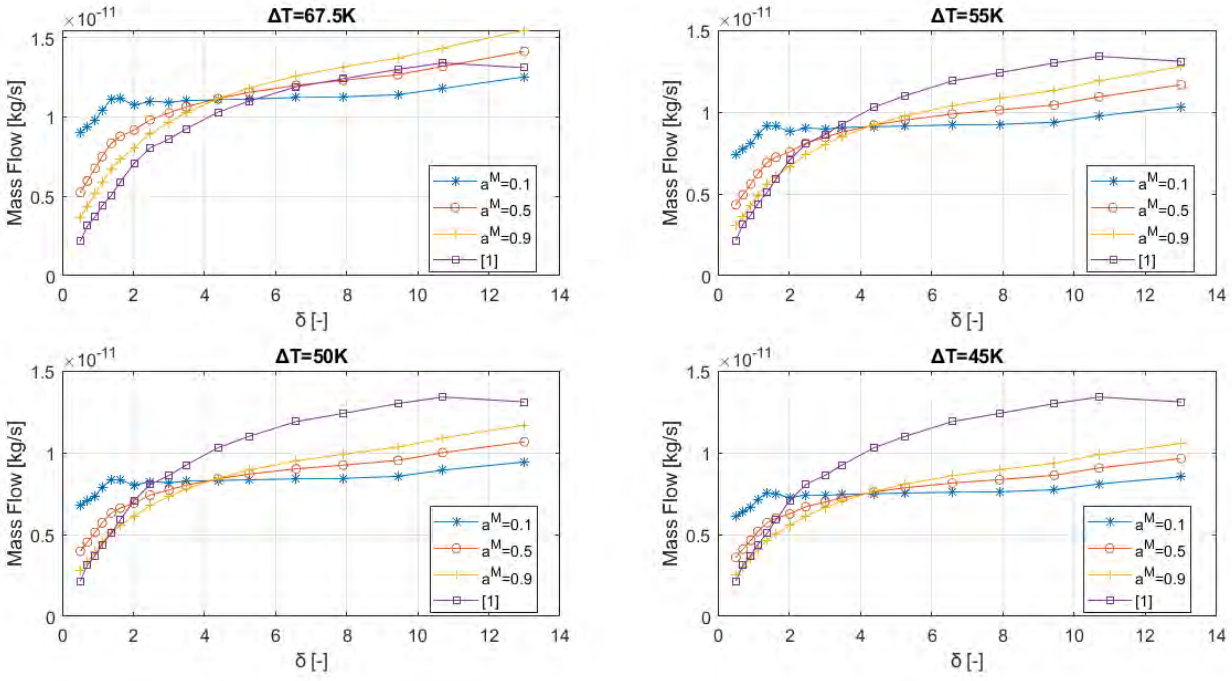

Figure C.2: Computational and experimental mass flow rates with Maxwell boundary conditions for various values of a_T^M and temperature differences in the case of He

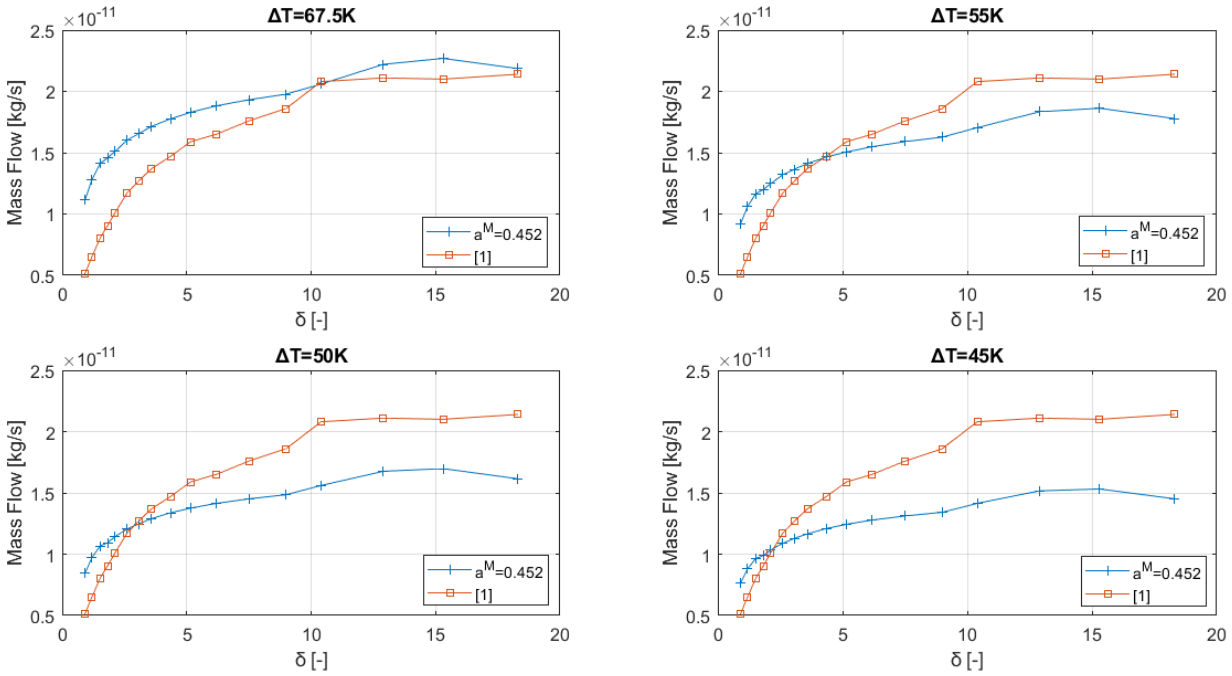

Figure C.3: Computational and experimental mass flow rates with Maxwell boundary conditions for various temperature differences in the case of Ne

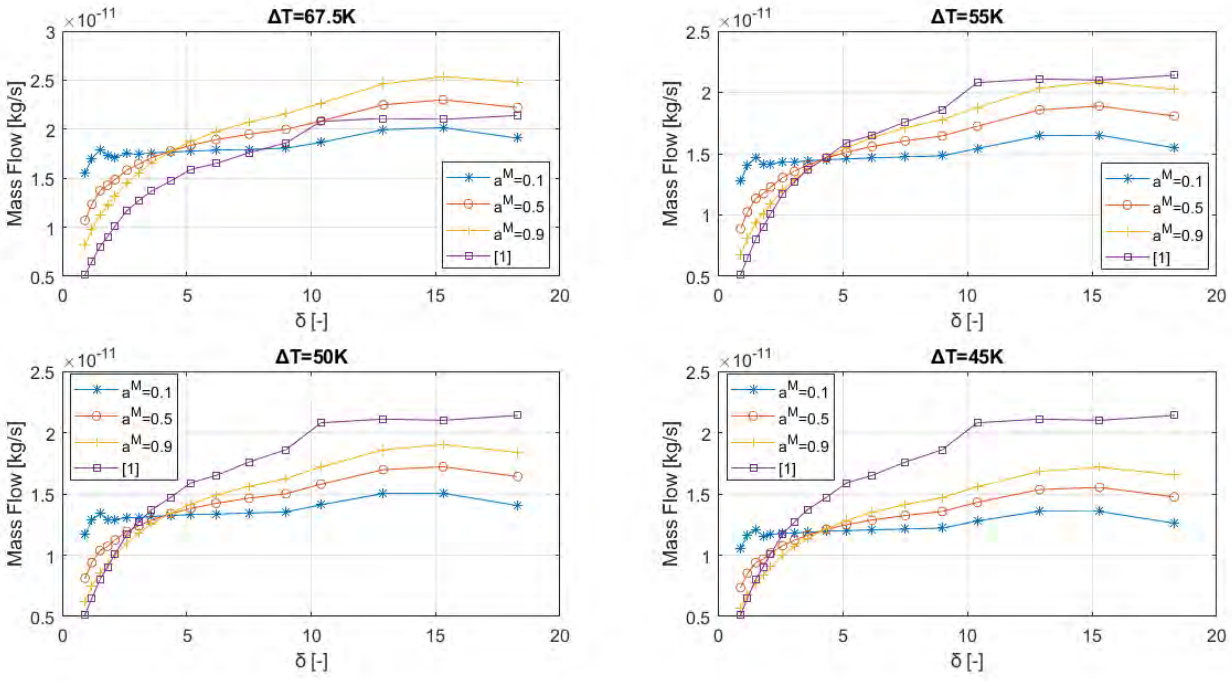

Figure C.4: Computational and experimental mass flow rates with Maxwell boundary conditions for various values of a_T^M and temperature differences in the case of Ne

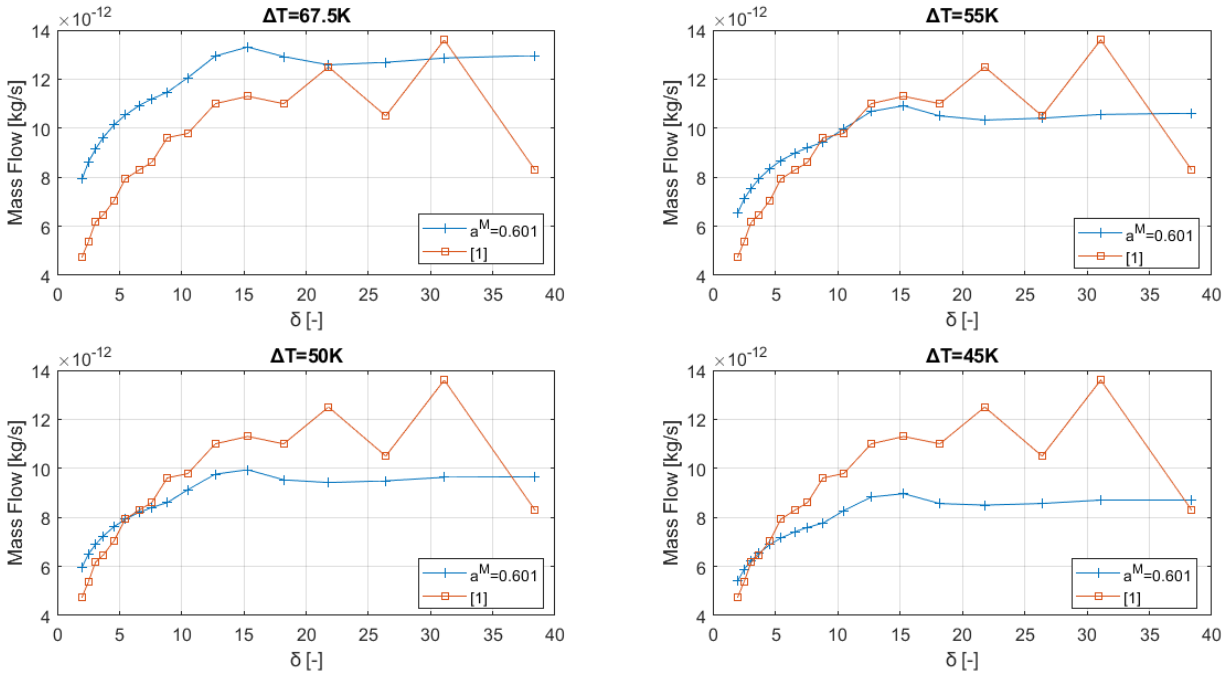

Figure C.5: Computational and experimental mass flow rates with Maxwell boundary conditions for various temperature differences in the case of N_2

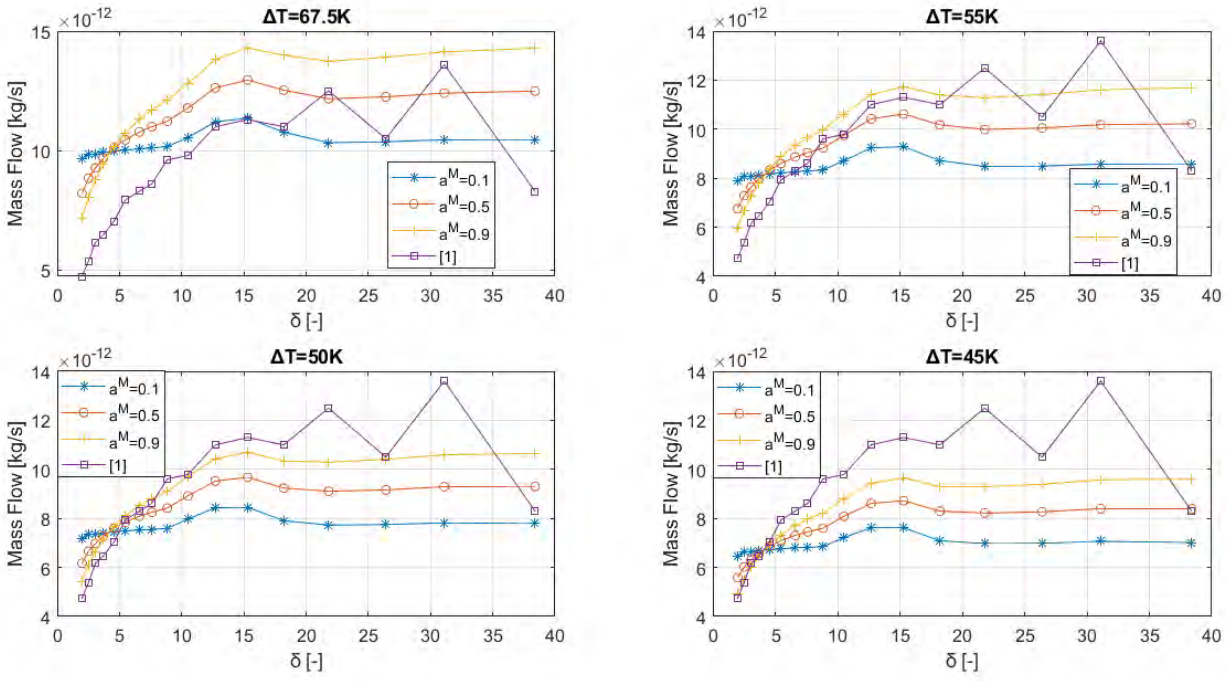

Figure C.6: Computational and experimental mass flow rates with Maxwell boundary conditions for various values of a_T^M and temperature differences in the case of N_2

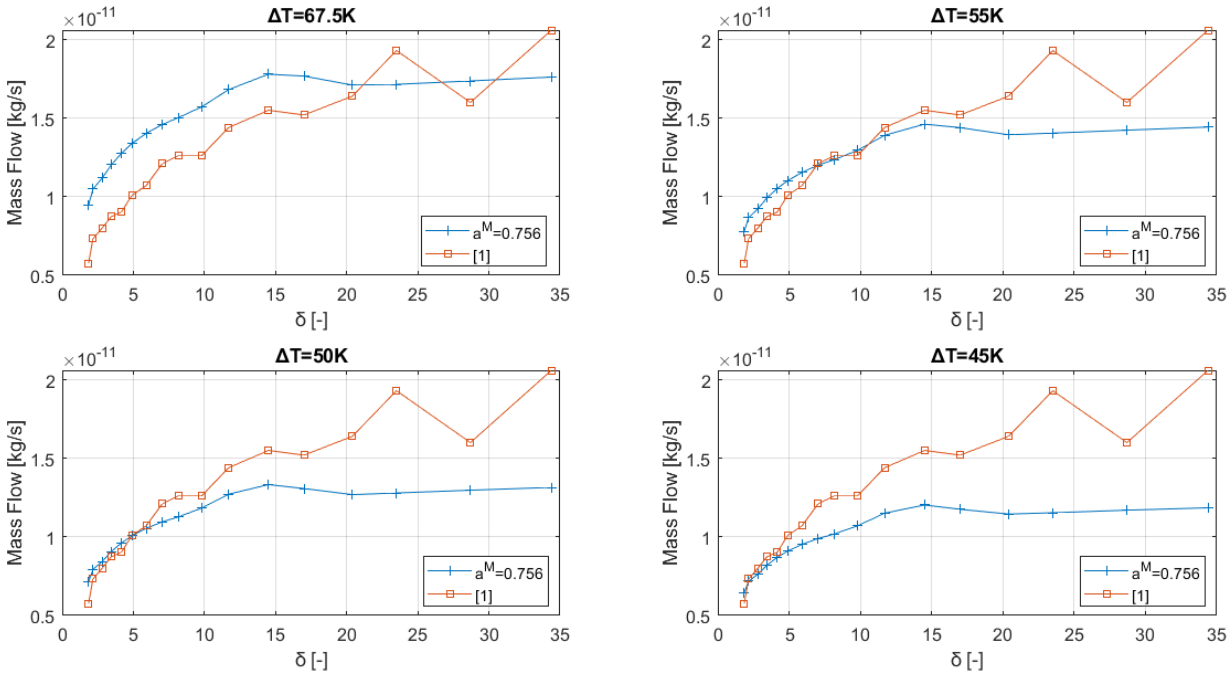

Figure C.7: Computational and experimental mass flow rates with Maxwell boundary conditions for various temperature differences in the case of Ar

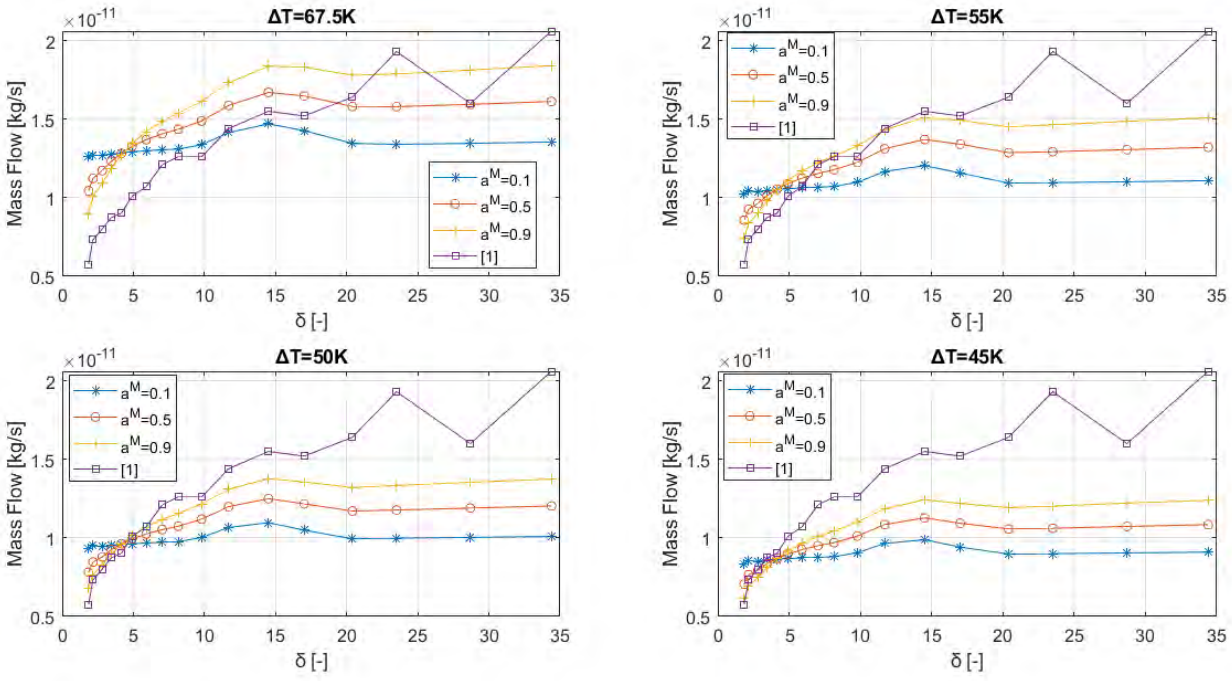

Figure C.8: Computational and experimental mass flow rates with Maxwell boundary conditions for various values of a_T^M and temperature differences in the case of Ar

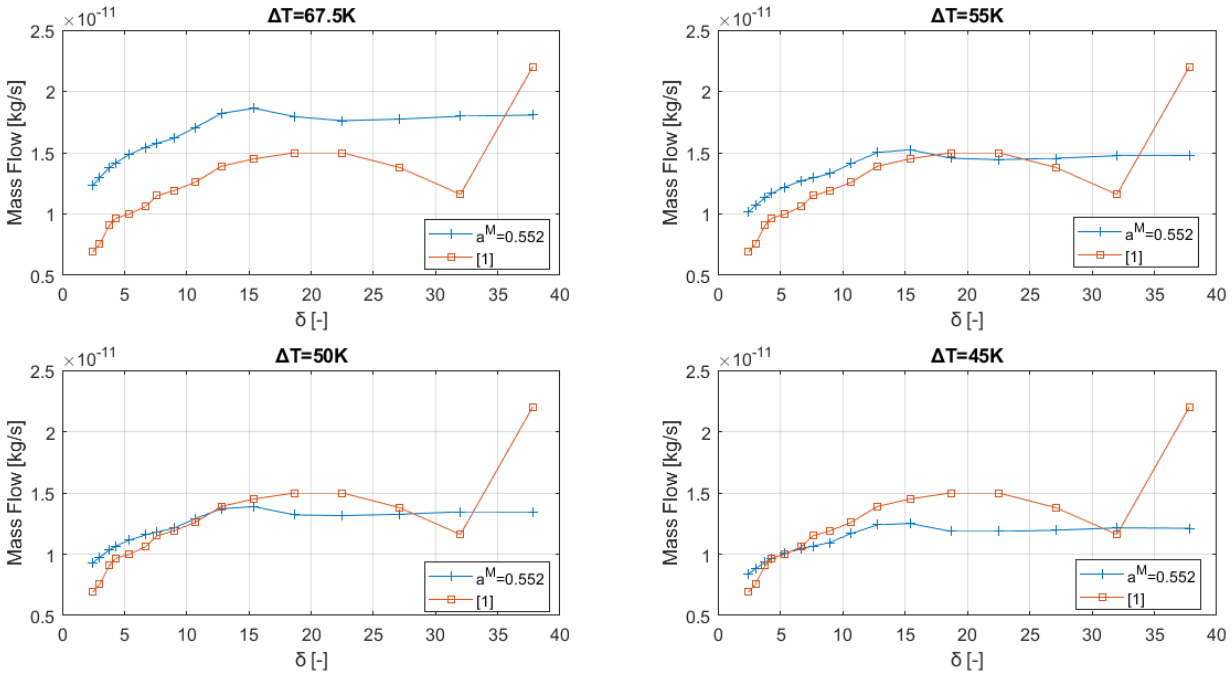

Figure C.9: Computational and experimental mass flow rates with Maxwell boundary conditions for various temperature differences in the case of Kr

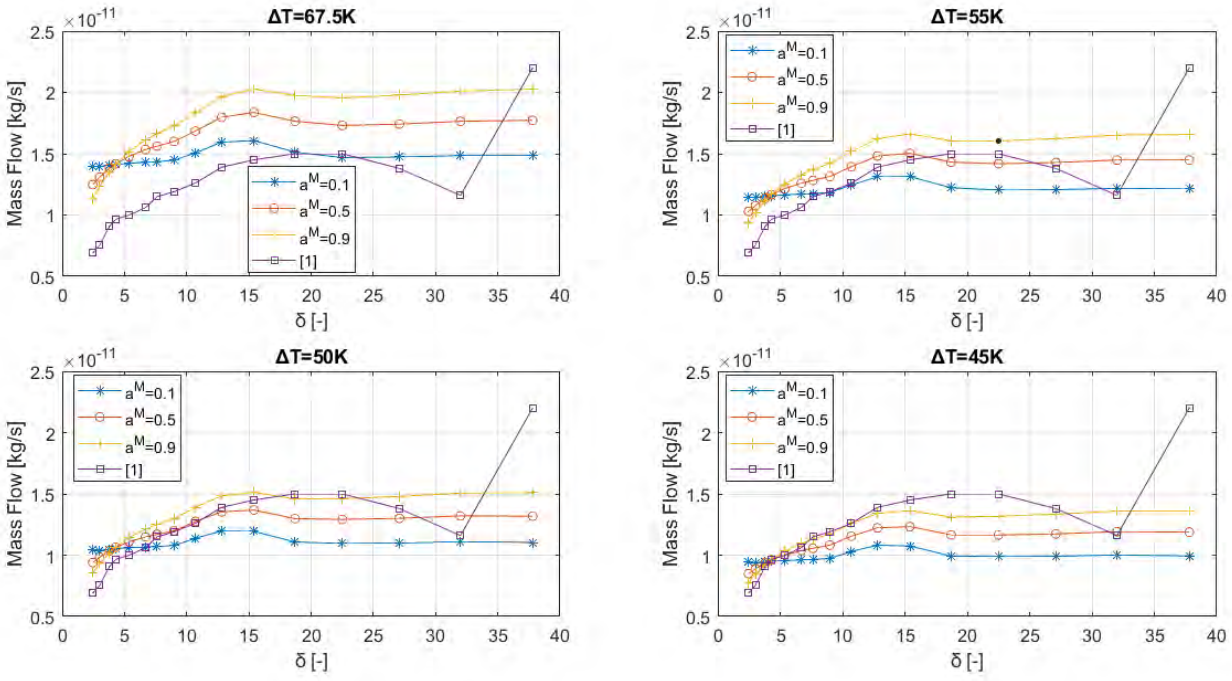

Figure C.10: Computational and experimental mass flow rates with Maxwell boundary conditions for various values of a_T^M and temperature differences in the case of Kr

Appendix D. Results for the temperature driven flow with Maxwell boundary conditions (ΔT=58K)

The results that occurred for the two temperature differences are quite similar for each gas, e.g. Helium presents good results, but in Argon oscillations exist. More specific:

- Helium: For the lower values of δ the error starts from a maximum value of 90% and starts decreasing. In the range of $\delta \in [6,12]$ the error is almost constant and smaller than 10%
- Neon: Similarly, Neon's error for the lower values of δ starts from a maximum error of 90% and decrease to 20% at $\delta = 4$. For $\delta \in [4,16]$ the error ranges between 15-20%. In the case of ΔT=50K the error in this range is near zero.
- Nitrogen: Presents oscillations in error through the graph with an average value around 25%, if the lower values are neglected where the error starts from 60% and decreases. For ΔT=45K the error gives the best results. For lower value of the coefficient, near $a_T^M = 0.1$, the error is greatly improved at ΔT=58K.
- Argon: In the range of $\delta \in [5,15]$ the error varies between 0-15%. In the rest values a greater error is presented or wider oscillations. The error in the range $\delta \in [5,15]$ seems to improve at $\Delta T \in [50,55]K$. For a lower value of the coefficient, $a_T^M \approx 0.5$, the error range approaches zero at ΔT=58K.
- Krypton: The error curve has a constant decreasing course as value of δ increases. A stabilization in the value seems to appear in the range of $\delta \in [5,12]$ with an average value of 30%. This value approaches zero at ΔT=45K.

Error graphs

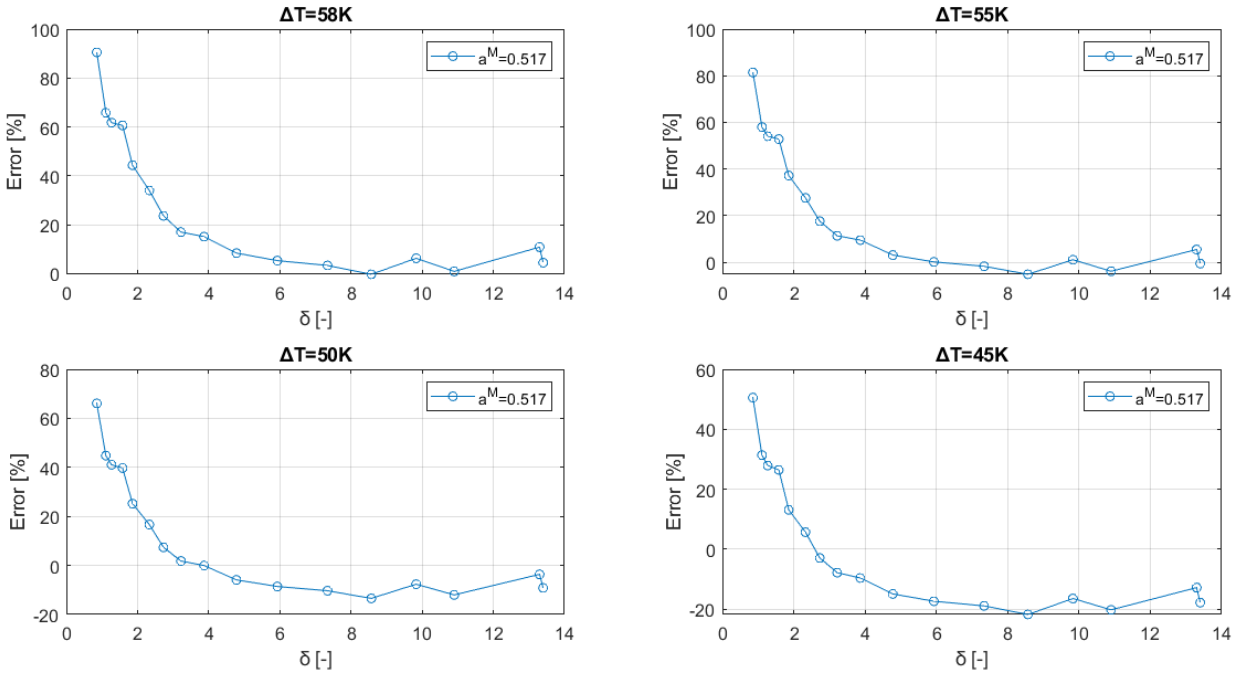

Figure D.1: Relative difference between experimental and computational mass flow rates with Maxwell boundary conditions for various temperature differences in the case of He (ΔT=58K)

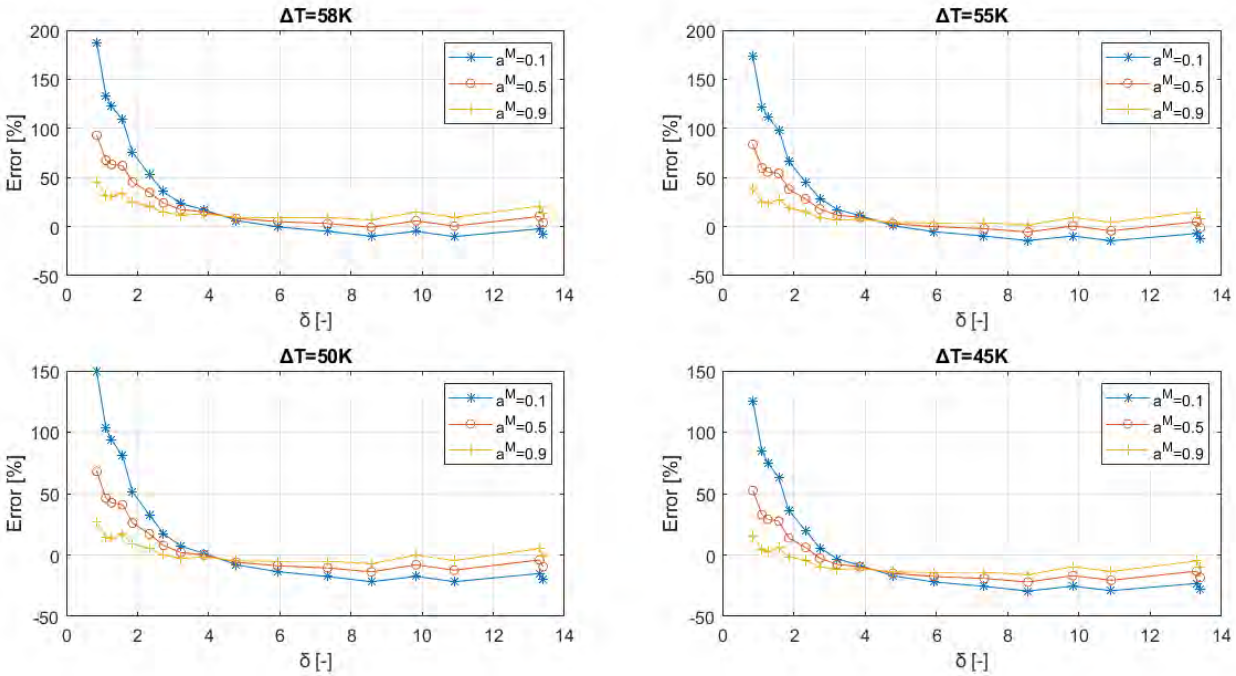

Figure D.2: Relative difference between experimental and computational mass flow rates with Maxwell boundary conditions for various values of a_T^M and temperature differences in the case of He (ΔT=58K)

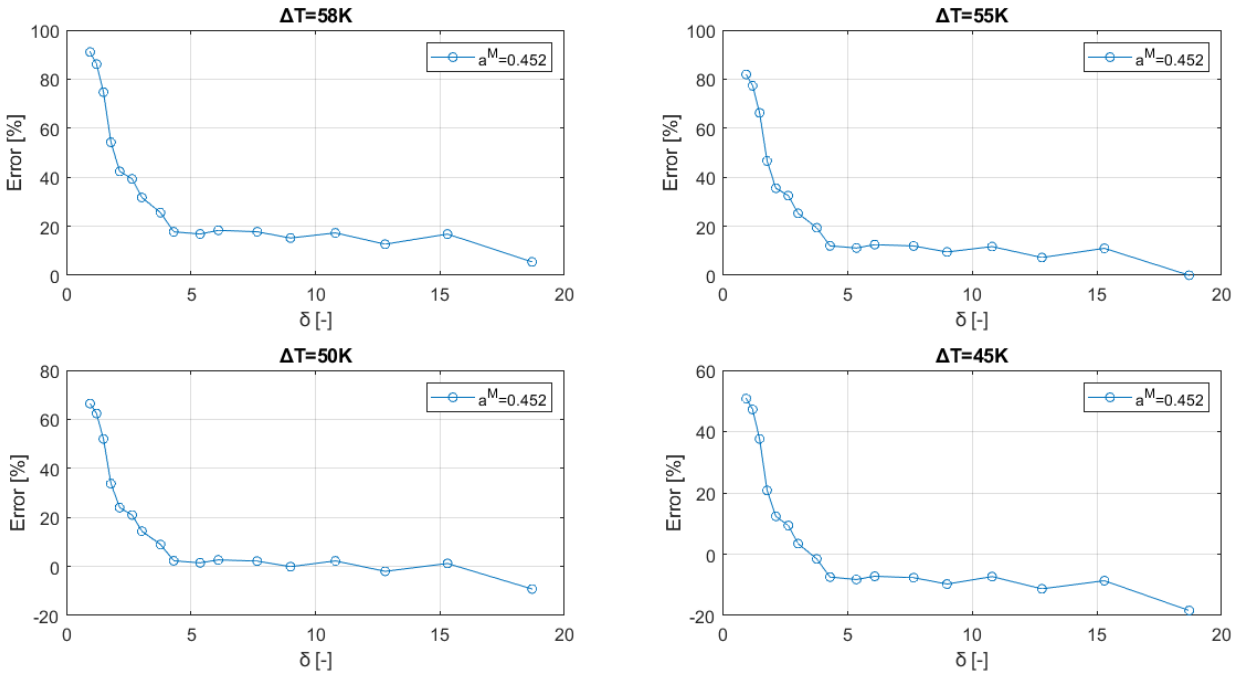

Figure D.3: Relative difference between experimental and computational mass flow rates with Maxwell boundary conditions for various temperature differences in the case of Ne (ΔT=58K)

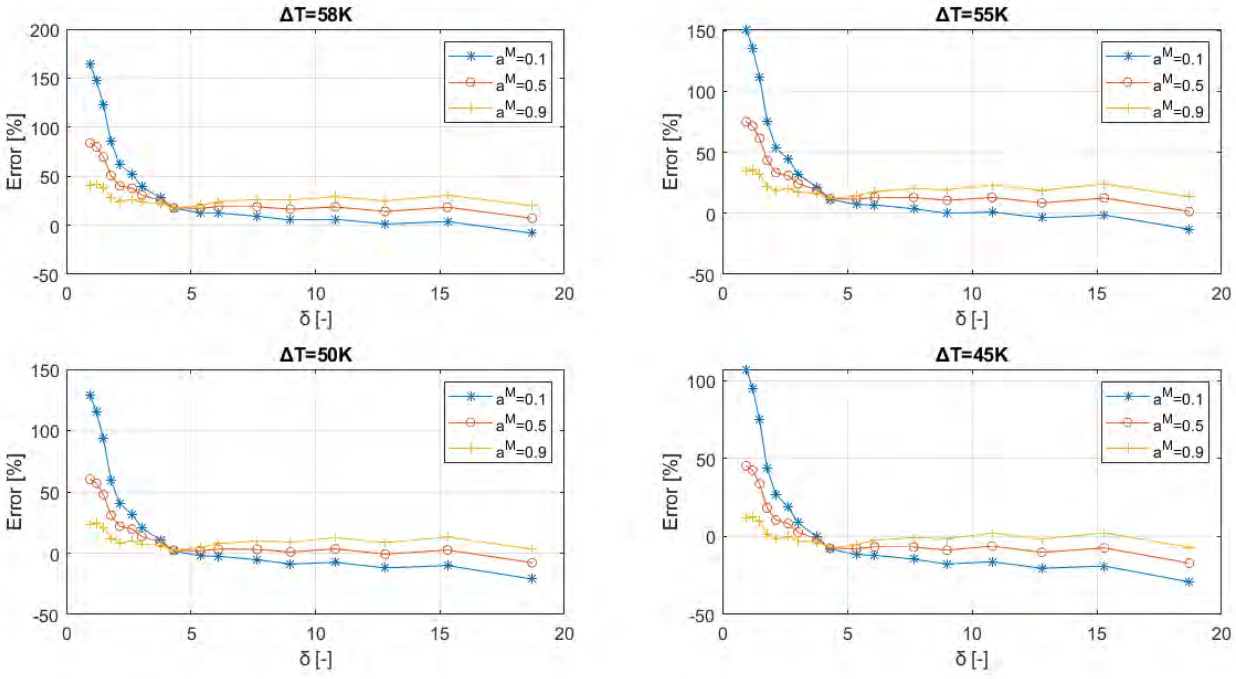

Figure D.4: Relative difference between experimental and computational mass flow rates with Maxwell boundary conditions for various values of a_T^M and temperature differences in the case of Ne (ΔT=58K)

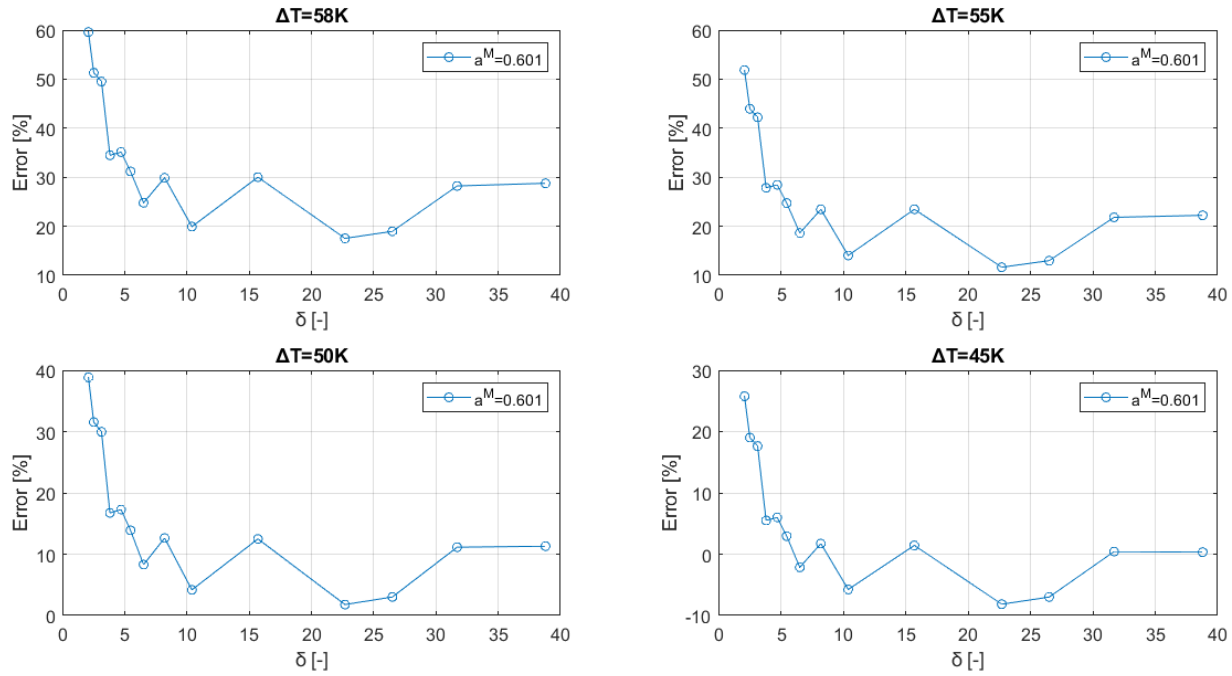

Figure D.5: Relative difference between experimental and computational mass flow rates with Maxwell boundary conditions for various temperature differences in the case of N_2 (ΔT=58K)

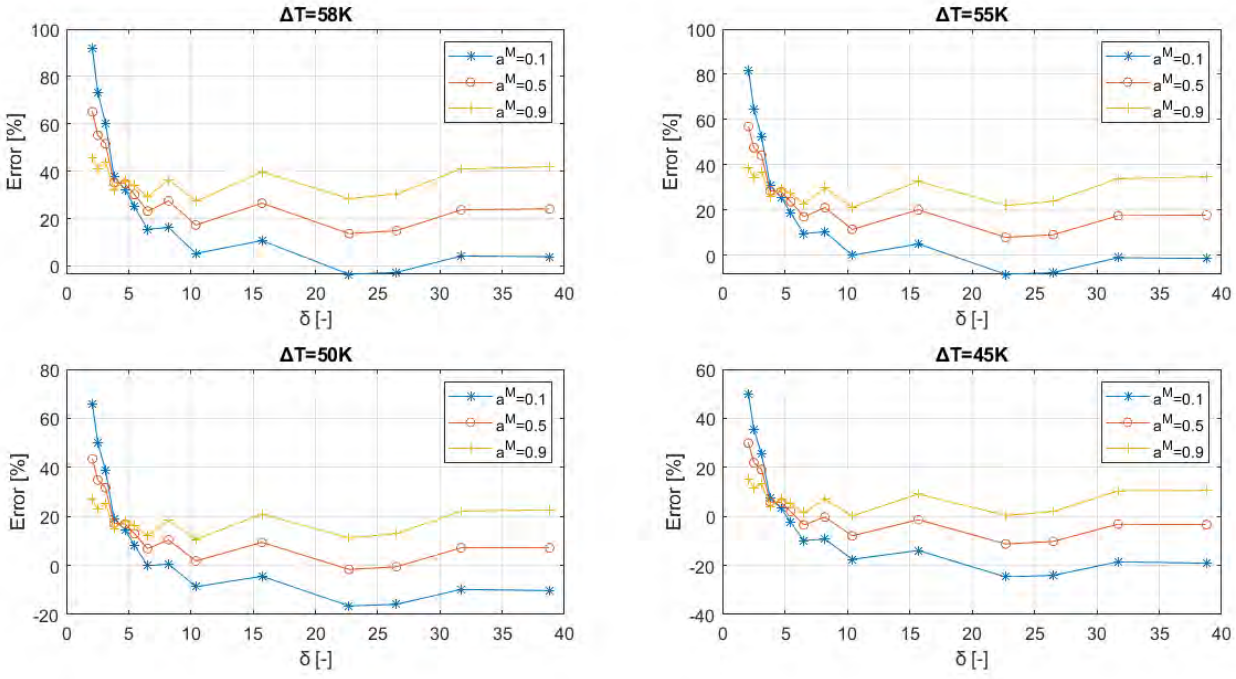

Figure D.6: Relative difference between experimental and computational mass flow rates with Maxwell boundary conditions for various values of a_T^M and temperature differences in the case of N_2 (ΔT=58K)

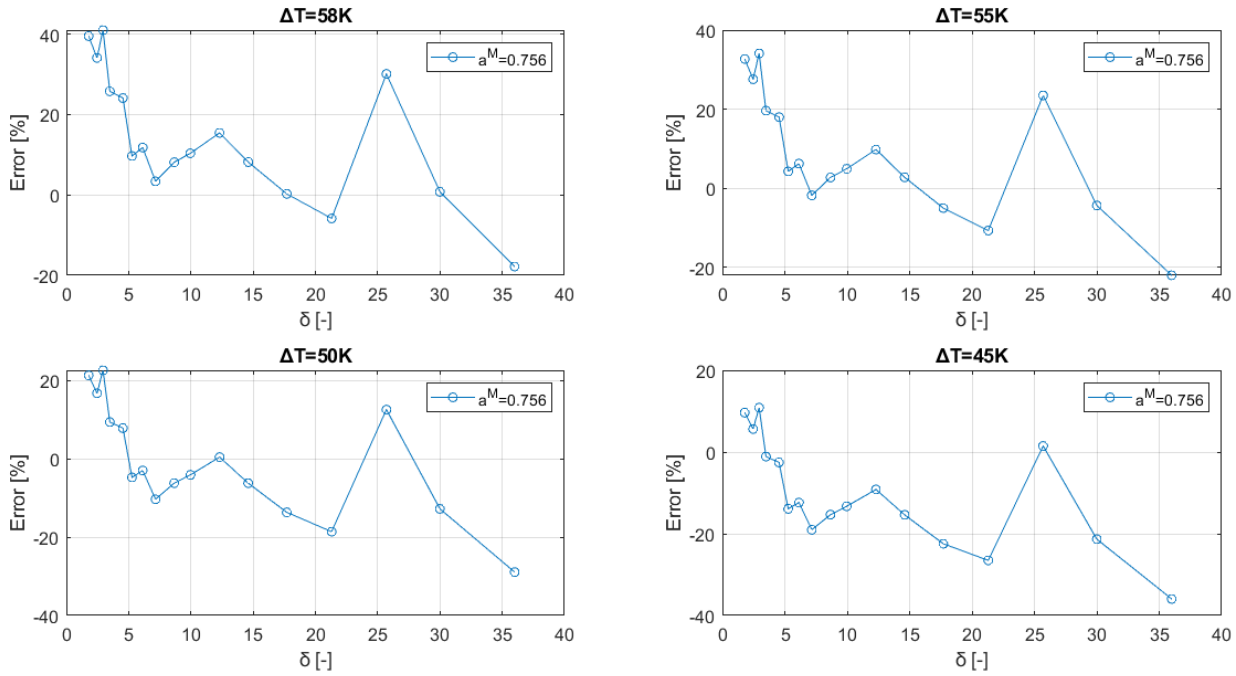

Figure D.7: Relative difference between experimental and computational mass flow rates with Maxwell boundary conditions for various temperature differences in the case of Ar (ΔT=58K)

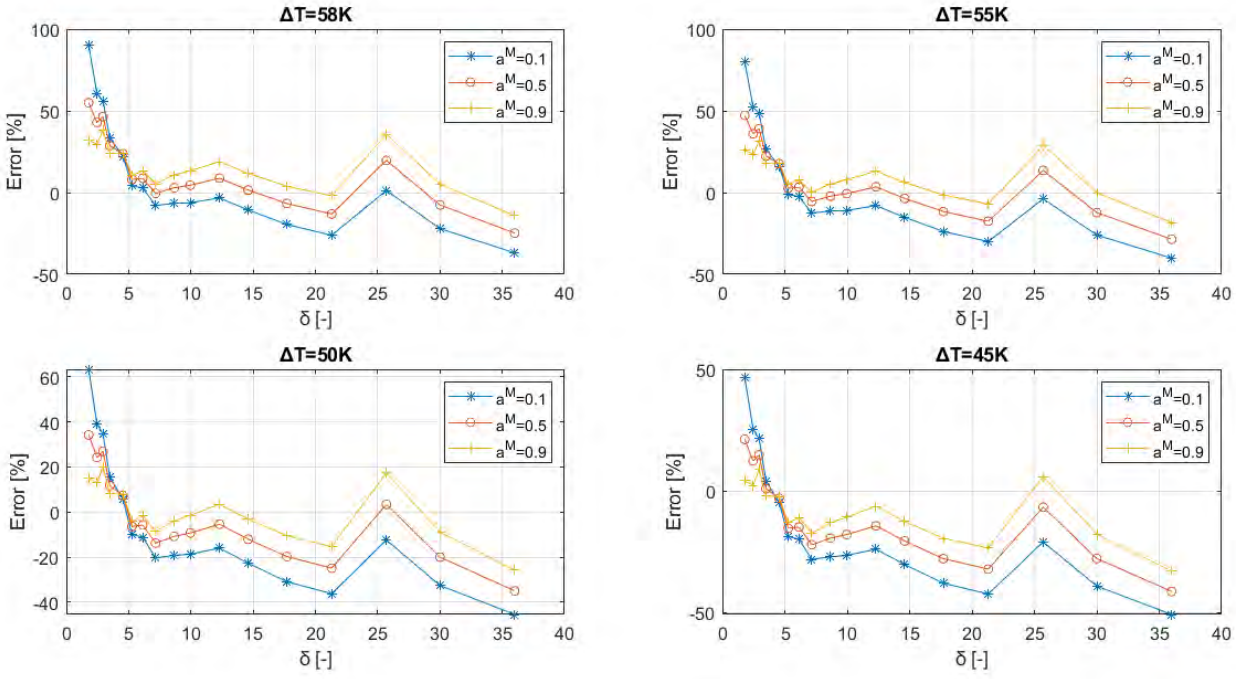

Figure D.8: Relative difference between experimental and computational mass flow rates with Maxwell boundary conditions for various values of a_T^M and temperature differences in the case of Ar (ΔT=58K)

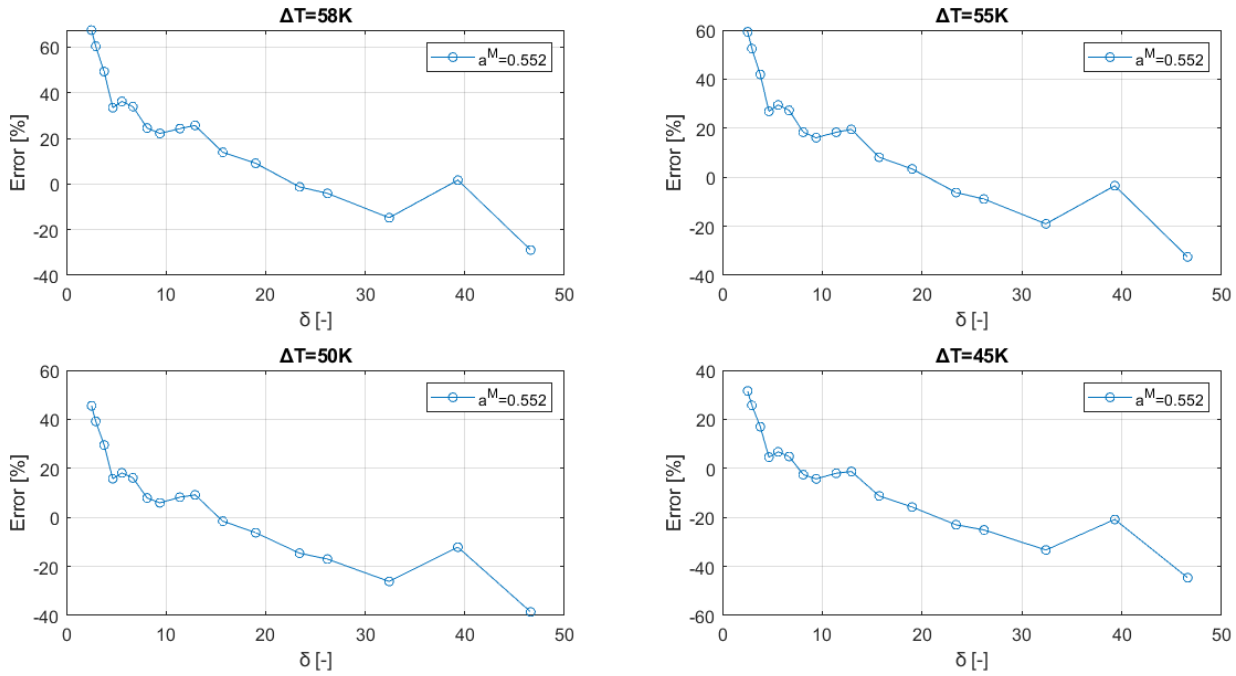

Figure D.9: Relative difference between experimental and computational mass flow rates with Maxwell boundary conditions for various temperature differences in the case of Kr (ΔT=58K)

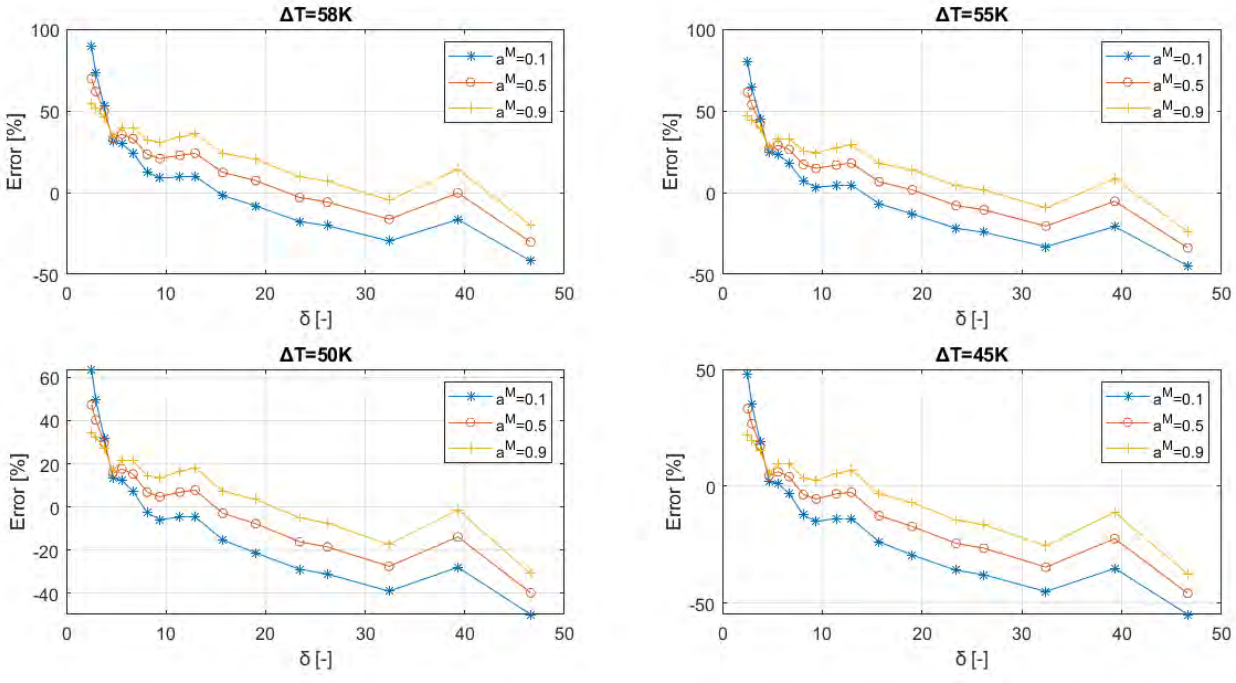

Figure D.10: Relative difference between experimental and computational mass flow rates with Maxwell boundary conditions for various values of a_T^M and temperature differences in the case of Kr (ΔT=58K)

Mass flow rate graphs

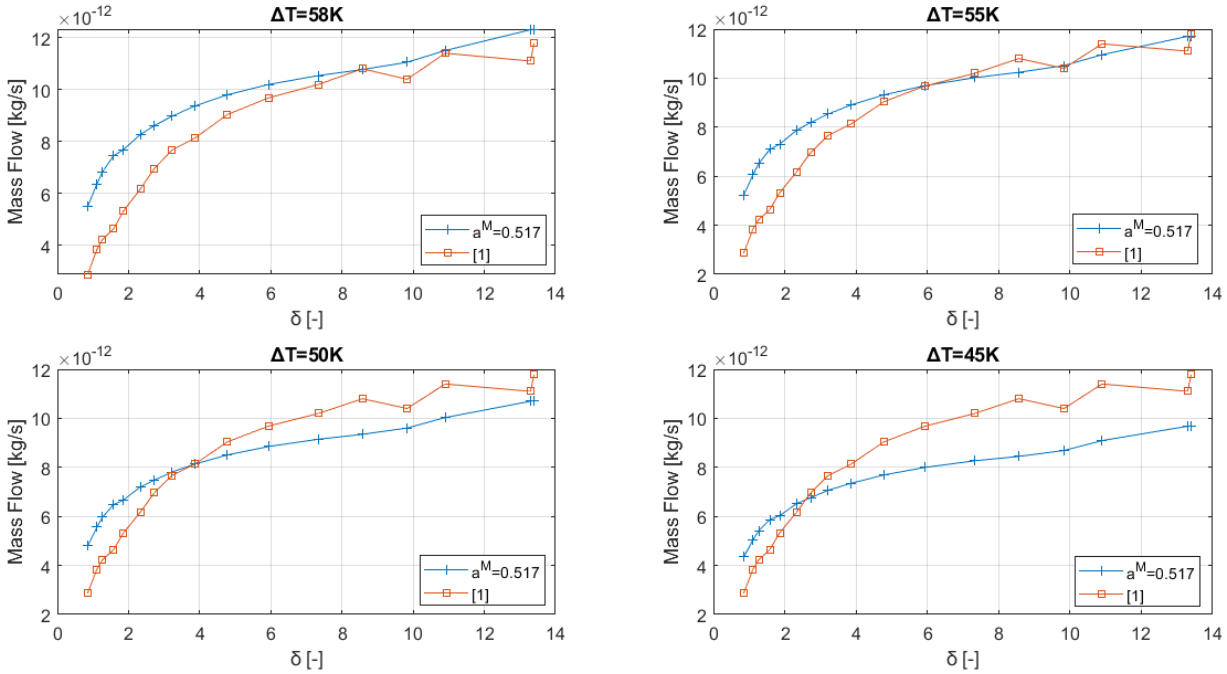

Figure D.11: Computational and experimental mass flow rates with Maxwell boundary conditions for various temperature differences in the case of He (ΔT=58K)

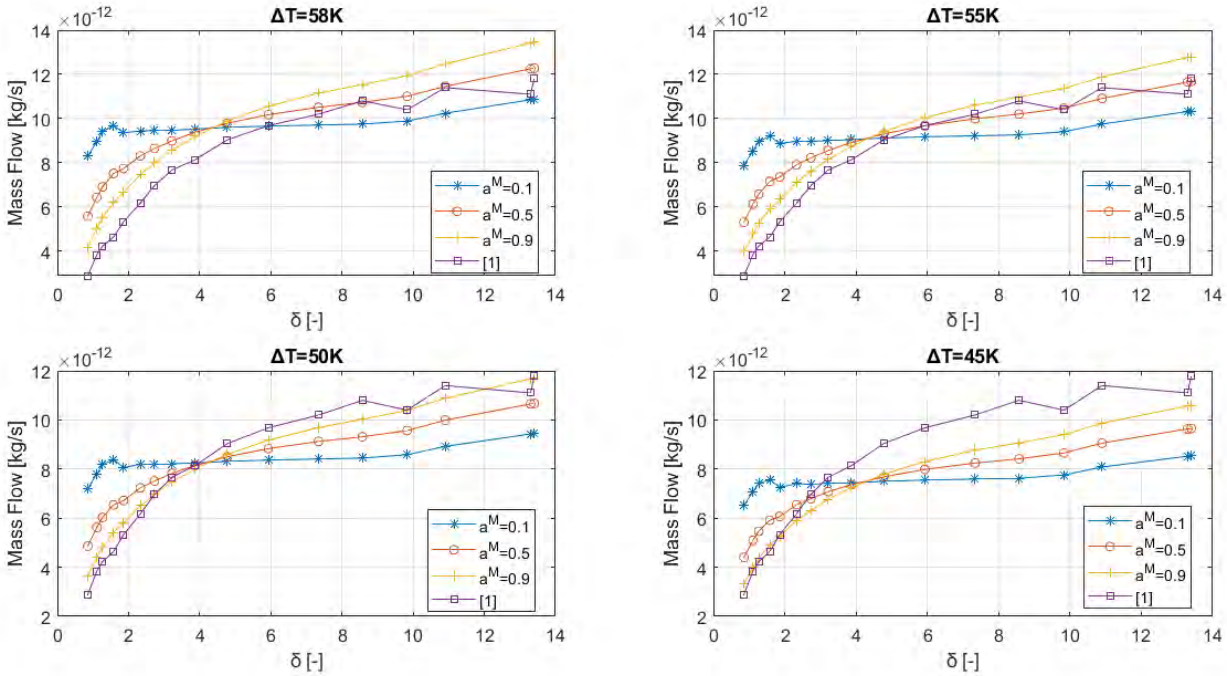

Figure D.12: Computational and experimental mass flow rates with Maxwell boundary conditions for various values of a_T^M and temperature differences in the case of He (ΔT=58K)

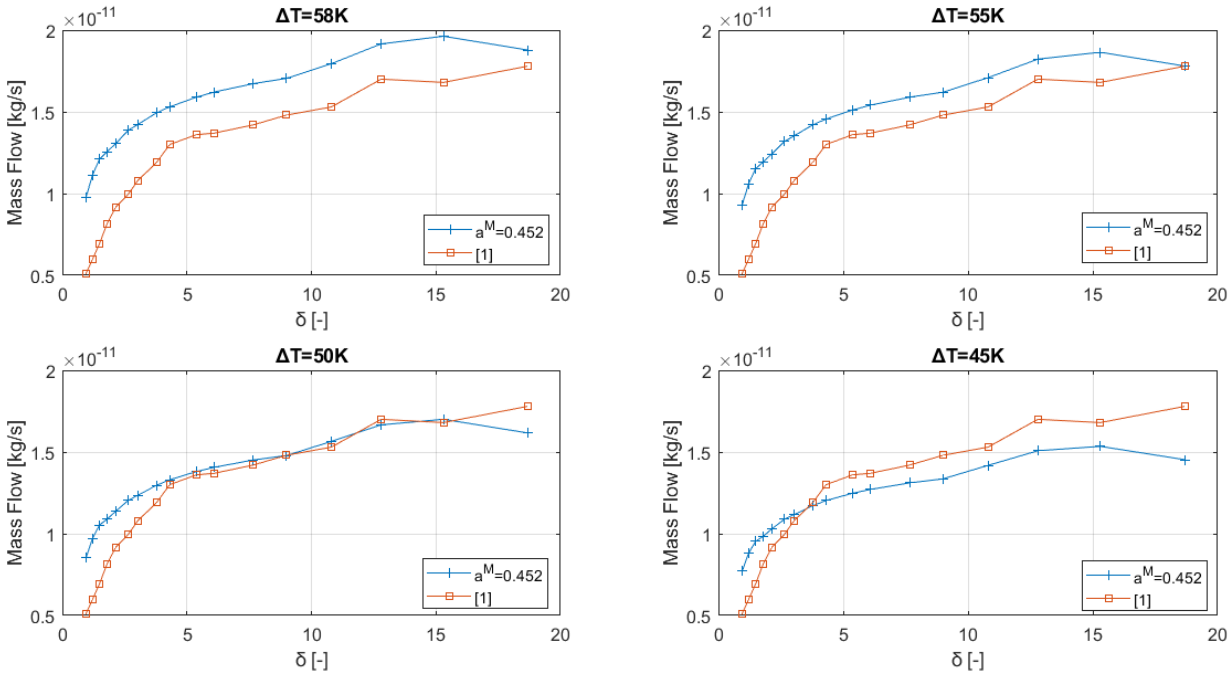

Figure D.13: Computational and experimental mass flow rates with Maxwell boundary conditions for various temperature differences in the case of Ne (ΔT=58K)

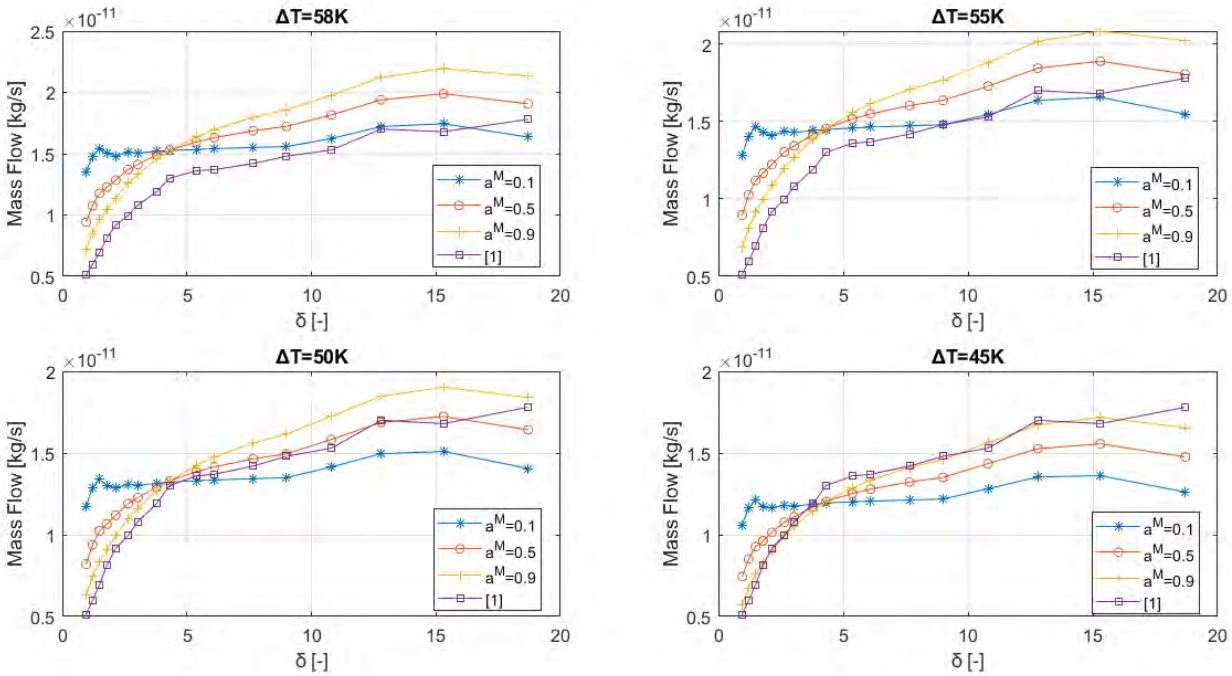

Figure D.14: Computational and experimental mass flow rates with Maxwell boundary conditions for various values of a_T^M and temperature differences in the case of Ne (ΔT=58K)

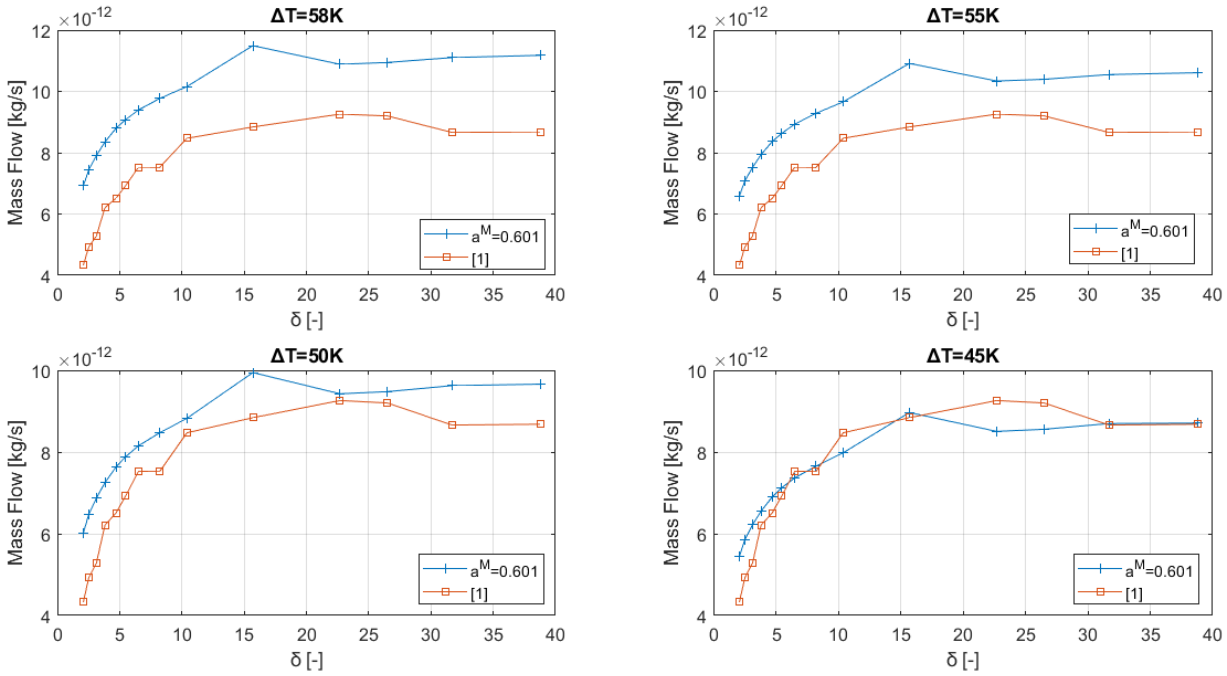

Figure D.15: Computational and experimental mass flow rates with Maxwell boundary conditions for various temperature differences in the case of N_2 (ΔT=58K)

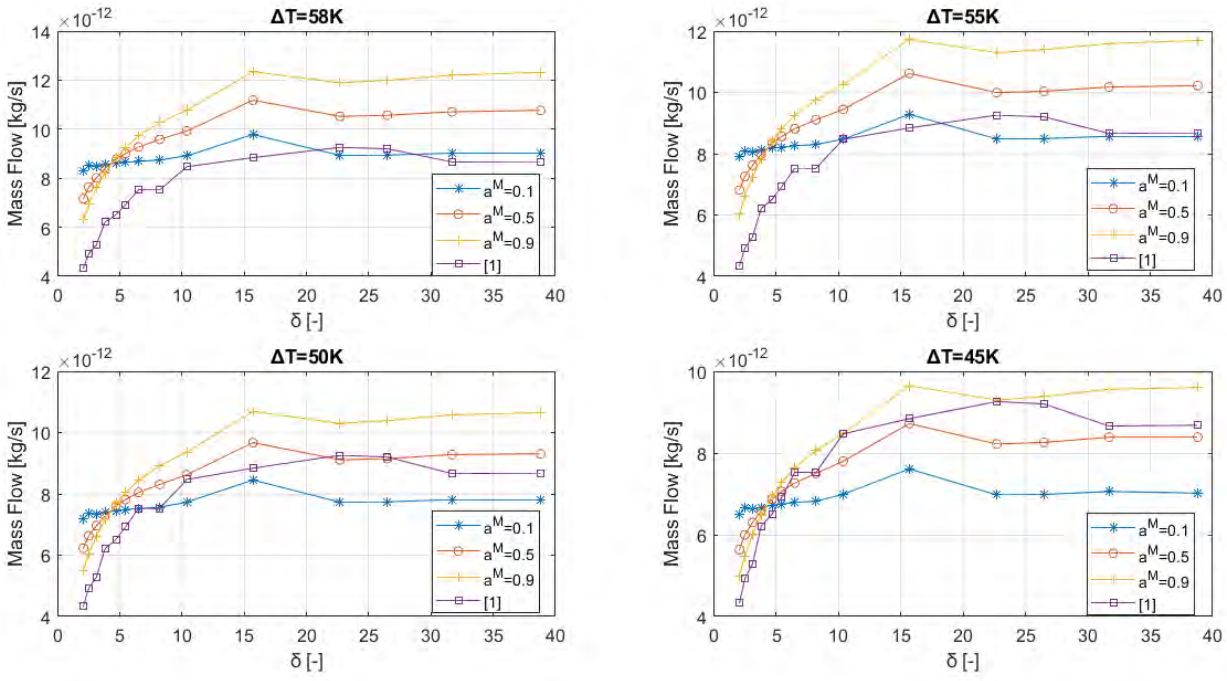

Figure D.16: Computational and experimental mass flow rates with Maxwell boundary conditions for various values of a_T^M and temperature differences in the case of N_2 (ΔT=58K)

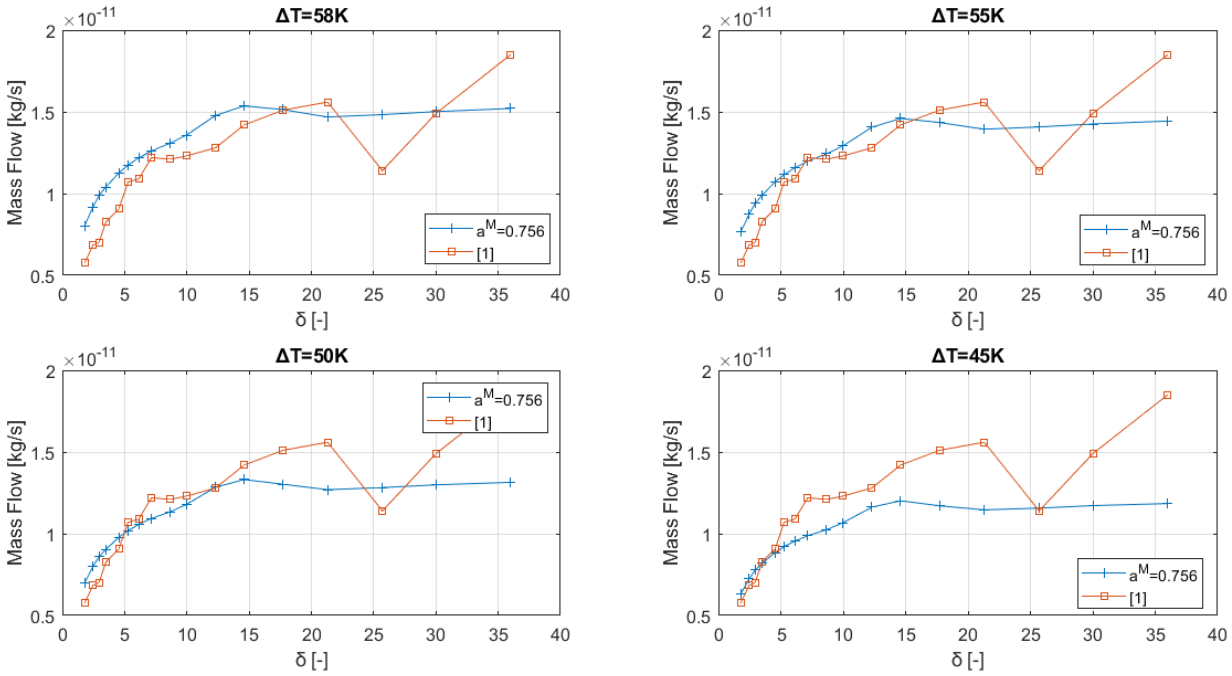

Figure D.17: Computational and experimental mass flow rates with Maxwell boundary conditions for various temperature differences in the case of Ar (ΔT=58K)

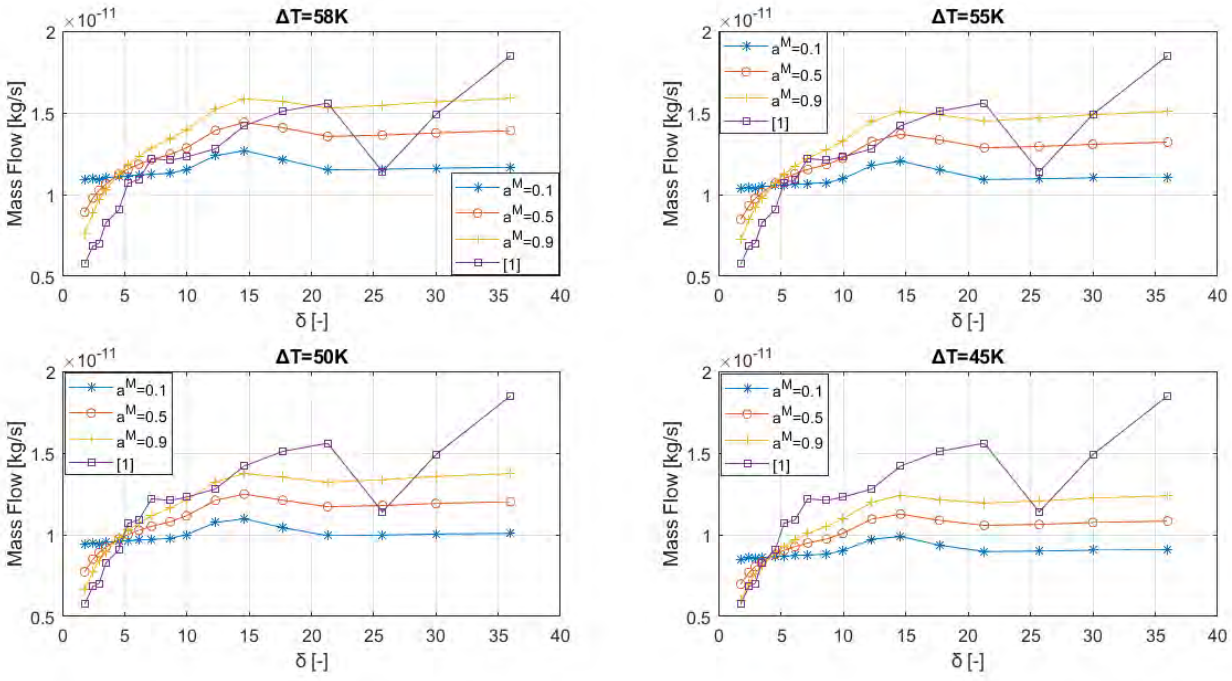

Figure D.18: Computational and experimental mass flow rates with Maxwell boundary conditions for various values of a_T^M and temperature differences in the case of Ar (ΔT=58K)

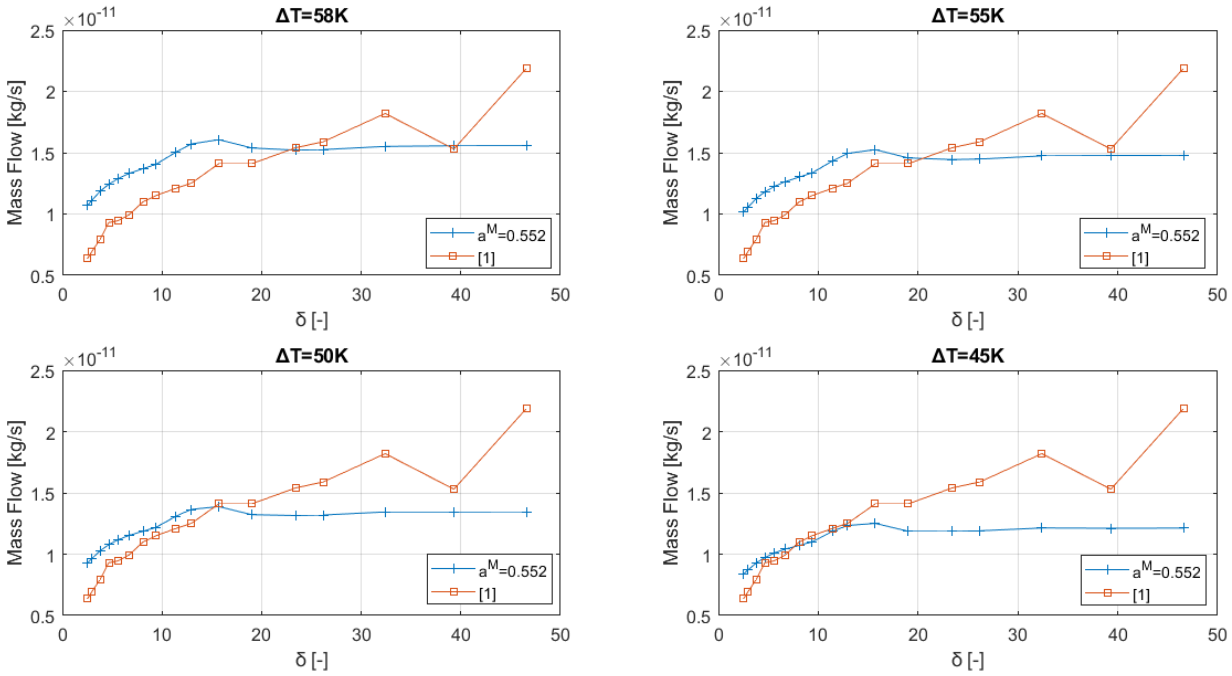

Figure D.19: Computational and experimental mass flow rates with Maxwell boundary conditions for various temperature differences in the case of Kr (ΔT=58K)

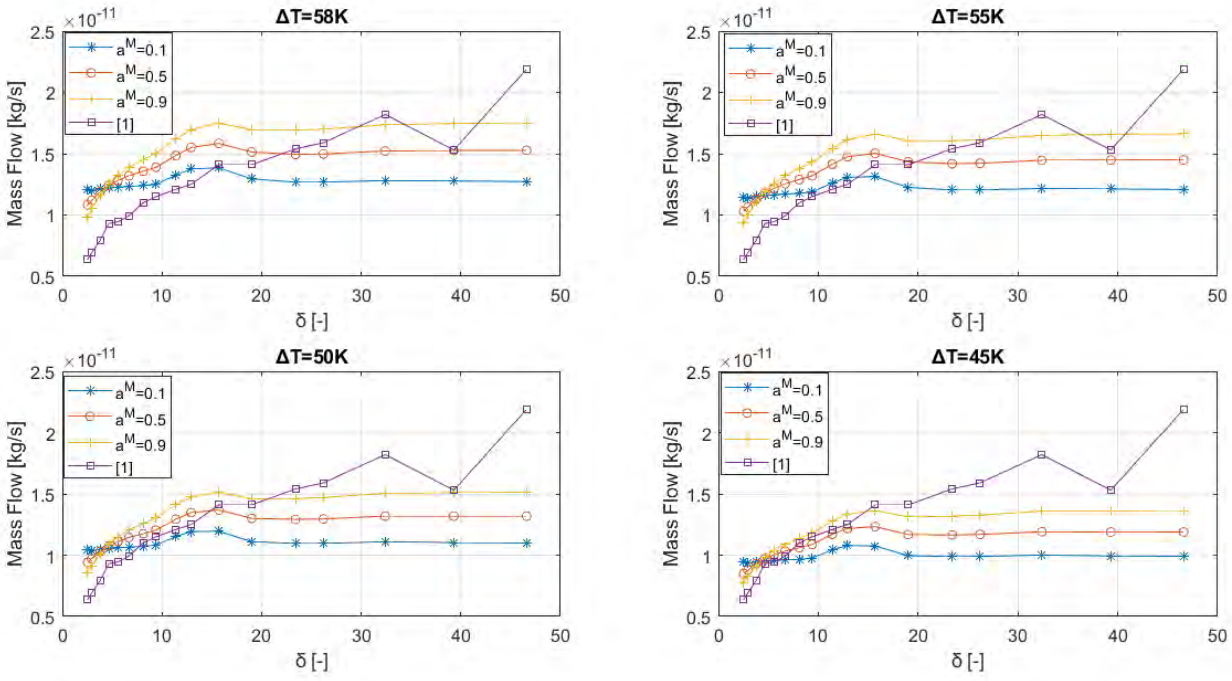

Figure D.20: Computational and experimental mass flow rates with Maxwell boundary conditions for various values of a_T^M and temperature differences in the case of Kr (ΔT=58K)

Appendix E. Results for the temperature driven flow with Cercignani-Lampis boundary conditions (ΔT=58K)

Concerning the comparison for ΔT=58K, Helium's curve has again the smallest deviations but for a shorter range than before, $\delta \in [3,8]$. The minimum error occurs at ΔT=55K, which as before is close with the measured one. Neon presents a smooth curve in the range of $\delta \in [6,12]$, with most suitable temperature difference ΔT=45K, where the error ranges between -5% and 2% depending on a_n. Nitrogen's results are improved compared to the previous and in the range of $\delta \in [10,25]$ the curve is quite smooth. The minimum error is achieved at ΔT=45K and regarding the value of coefficient a_n, the error is between -4% and 4%. Argon once more presents bad results with error curve filled with oscillations, while Krypton's curve is almost linear, but constantly diminishes from positive to negative values of error. Only in the range of $\delta \in [7,13]$ the error remains steady and for ΔT=45K is close to zero.

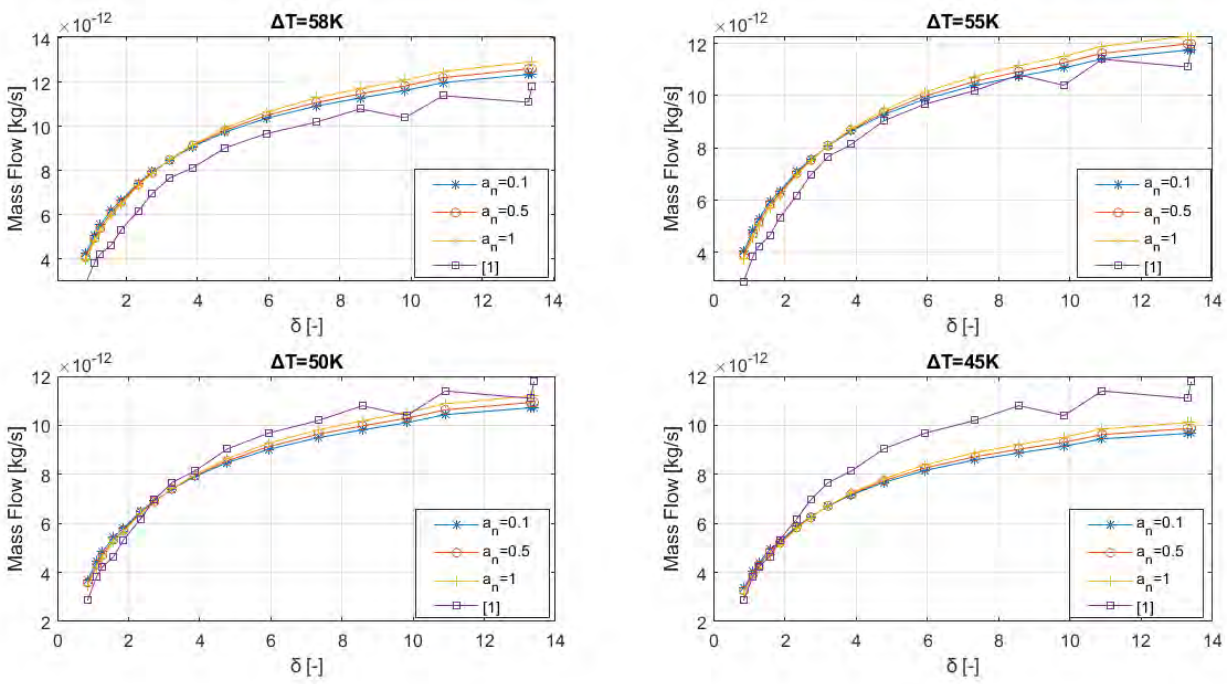

Figure E.1: Computational and experimental mass flow rates with CL boundary conditions for various values of a_n and temperature differences in the case of He (ΔT=58K)

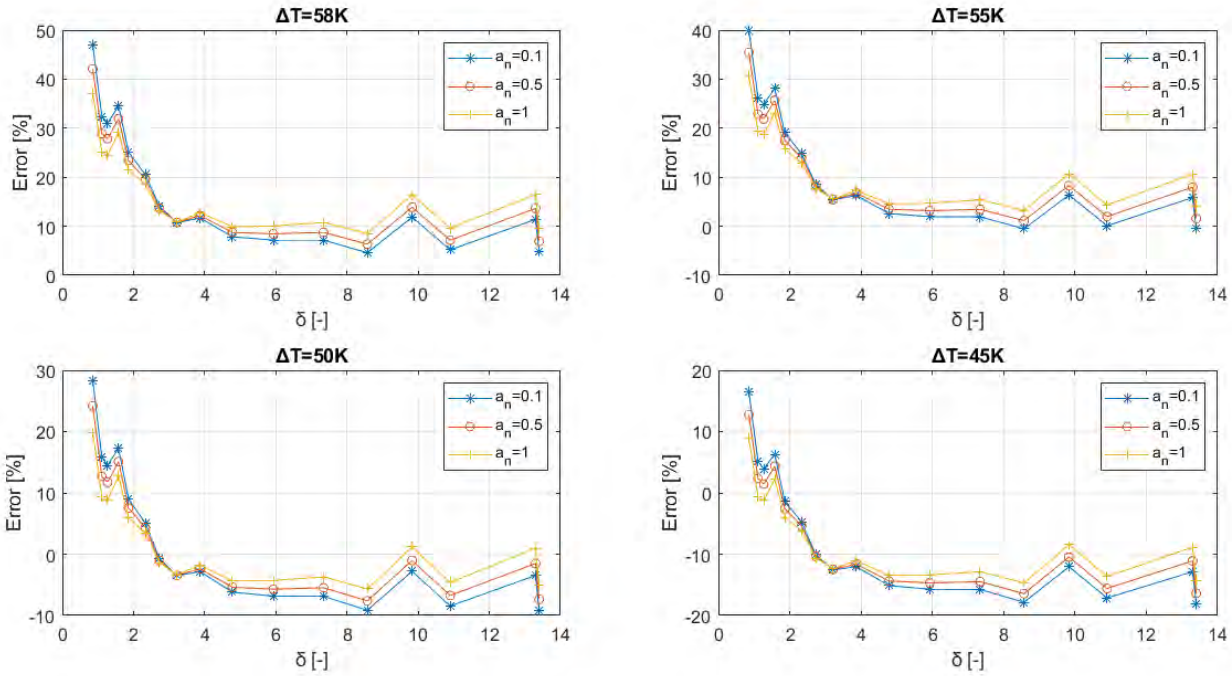

Figure E.2: Relative difference between computational and experimental mass flow rates with CL boundary conditions for various values of a_n and temperature differences in the case of He (ΔT=58K)

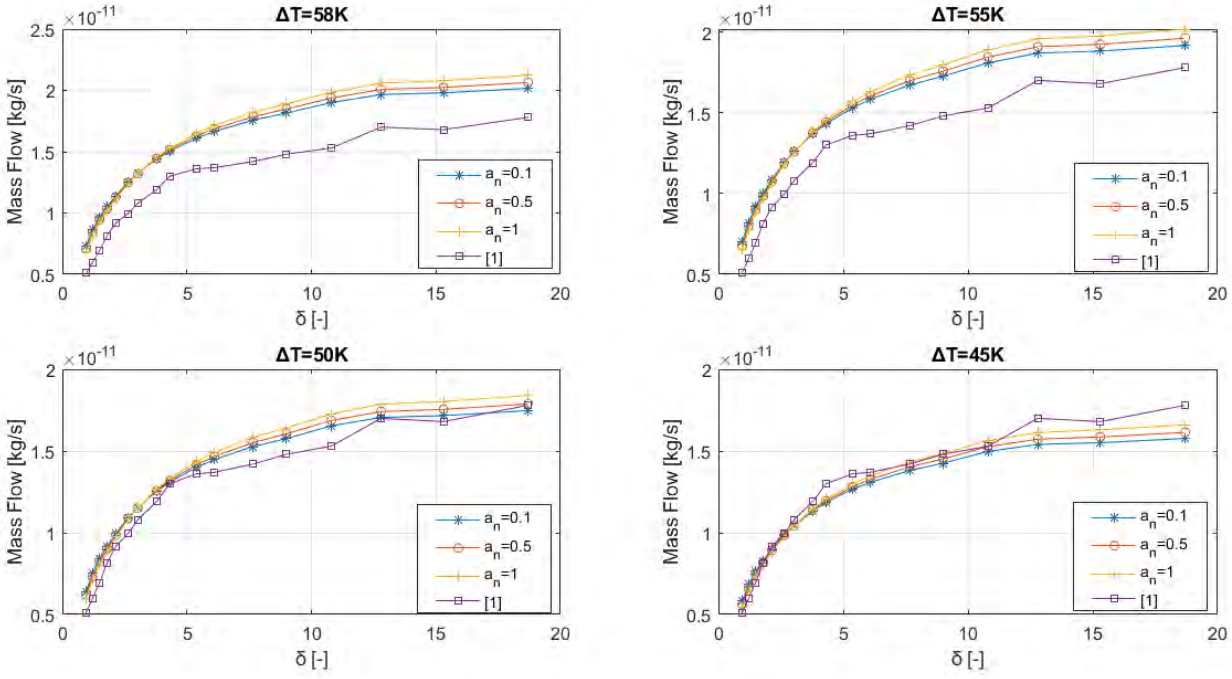

Figure E.3: Computational and experimental mass flow rates with CL boundary conditions for various values of a_n and temperature differences in the case of Ne (ΔT=58K)

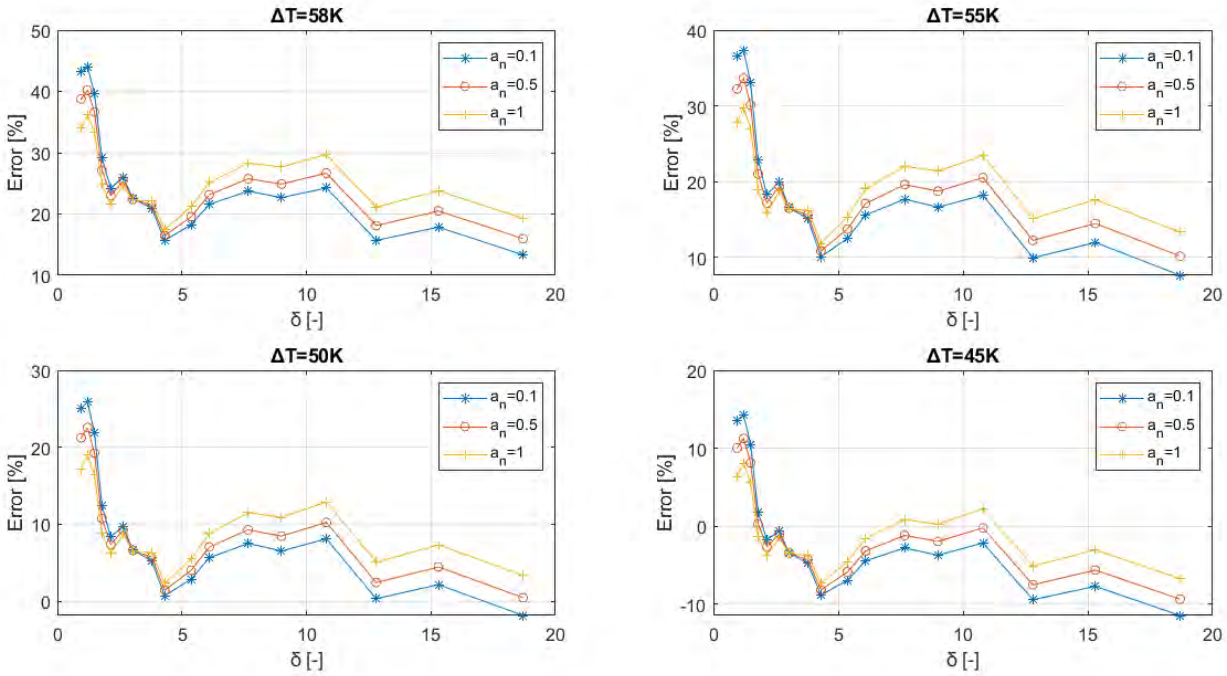

Figure E.4: Relative difference between computational and experimental mass flow rates with CL boundary conditions for various values of a_n and temperature differences in the case of Ne (ΔT=58K)

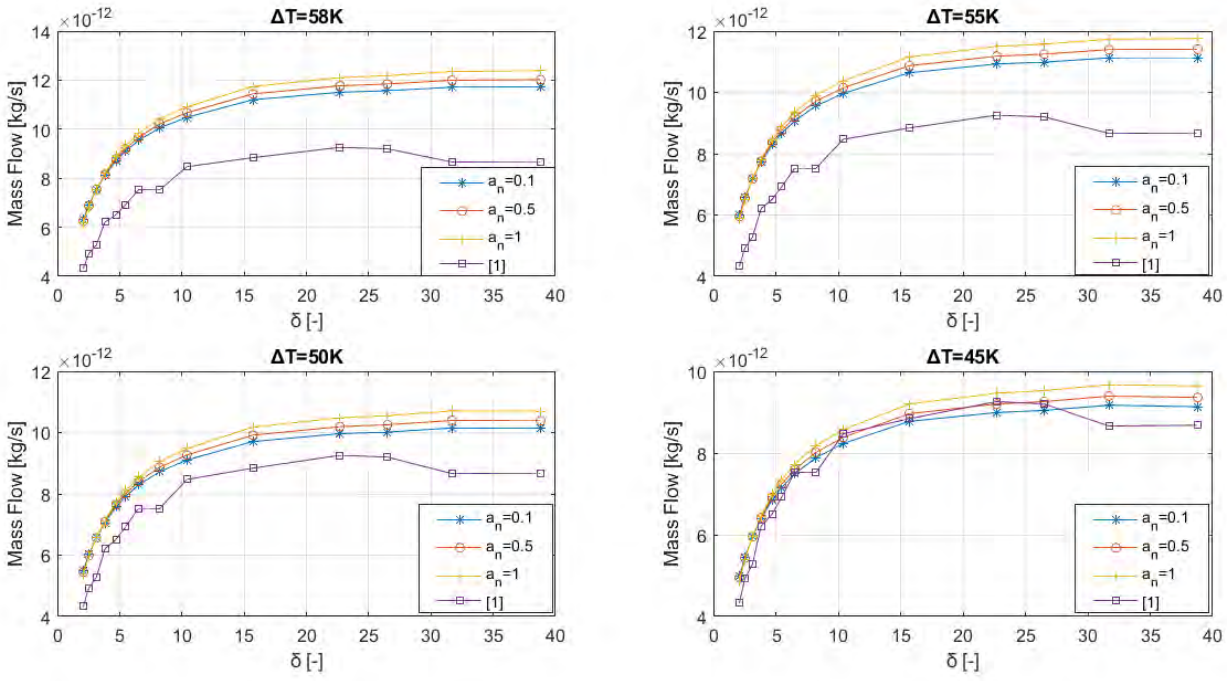

Figure E.5: Computational and experimental mass flow rates with CL boundary conditions for various values of a_n and temperature differences in the case of N_2 (ΔT=58K)

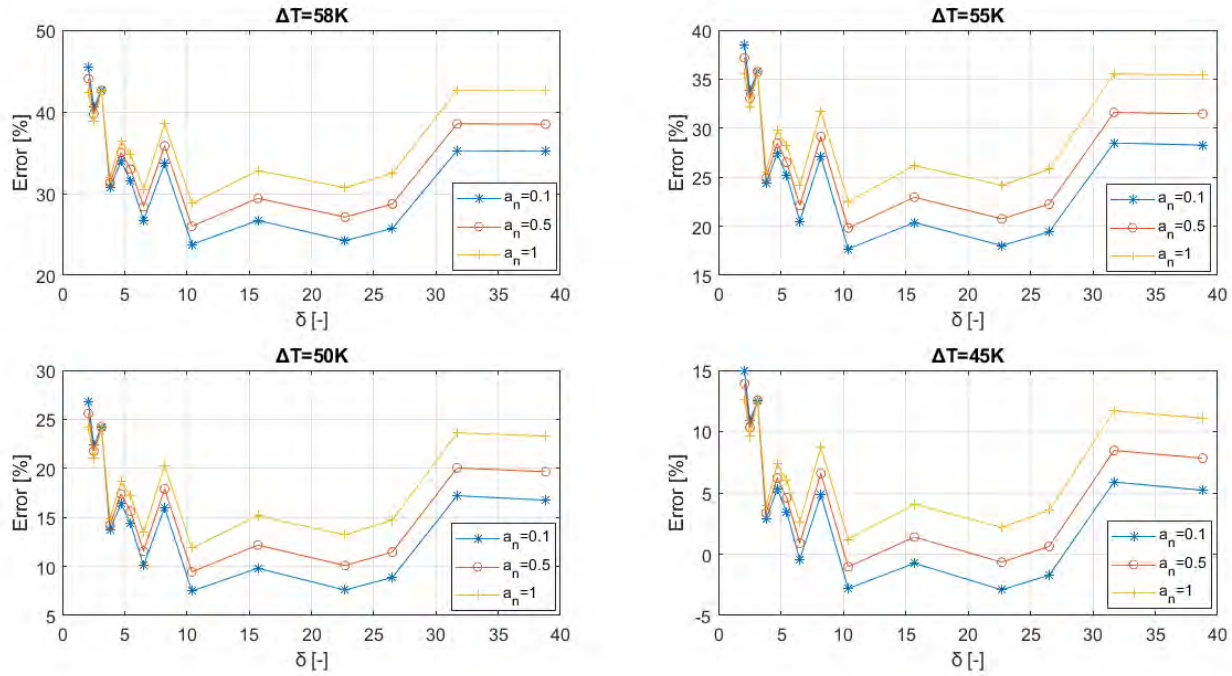

Figure E.6: Relative difference between computational and experimental mass flow rates with CL boundary conditions for various values of a_n and temperature differences in the case of N_2 (ΔT=58K)

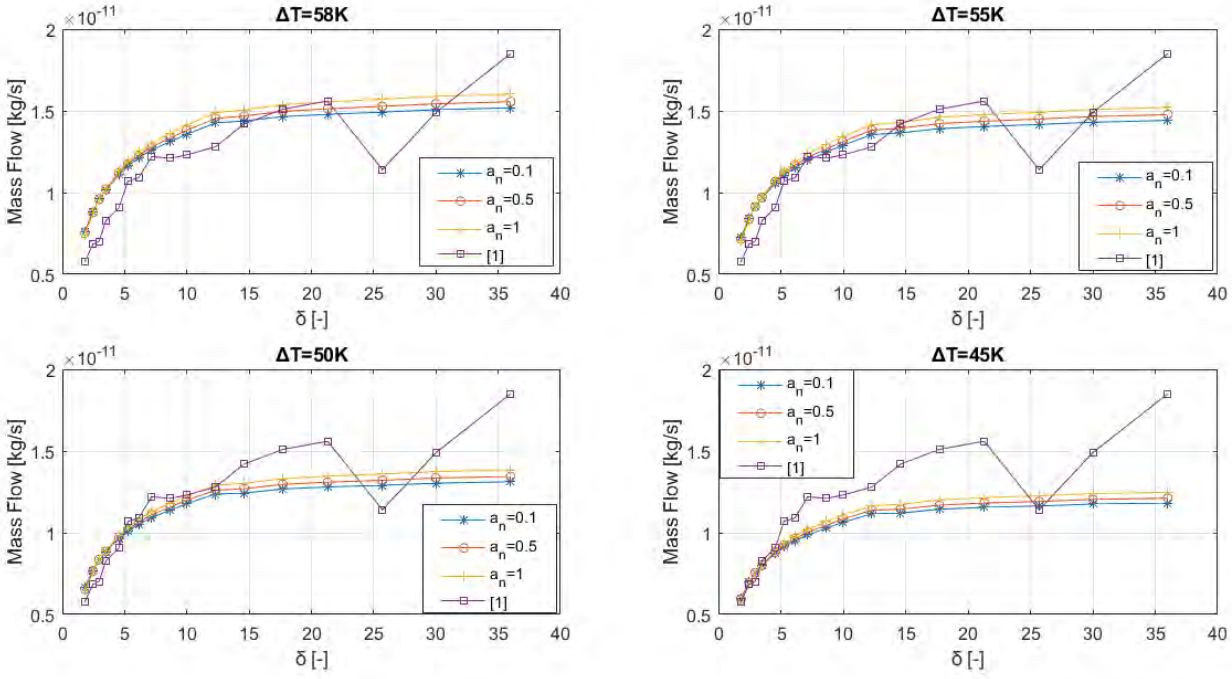

Figure E.7: Computational and experimental mass flow rates with CL boundary conditions for various values of a_n and temperature differences in the case of Ar (ΔT=58K)

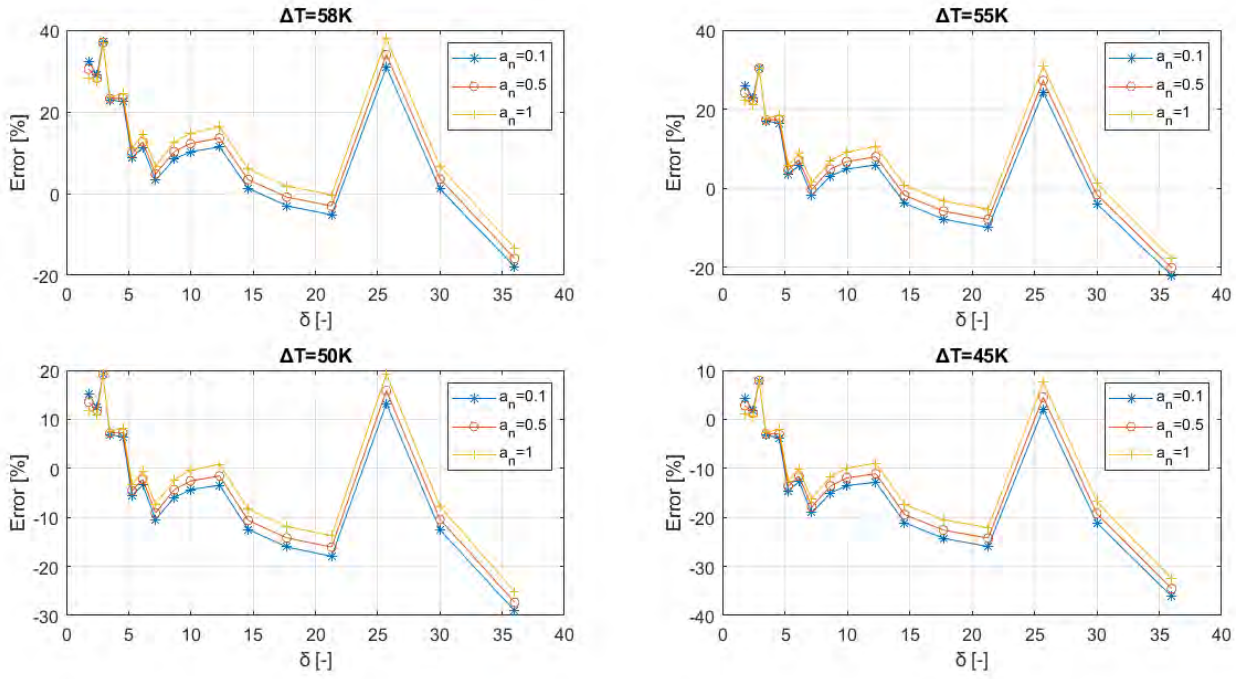

Figure E.8: Relative difference between computational and experimental mass flow rates with CL boundary conditions for various values of a_n and temperature differences in the case of Ar (ΔT=58K)

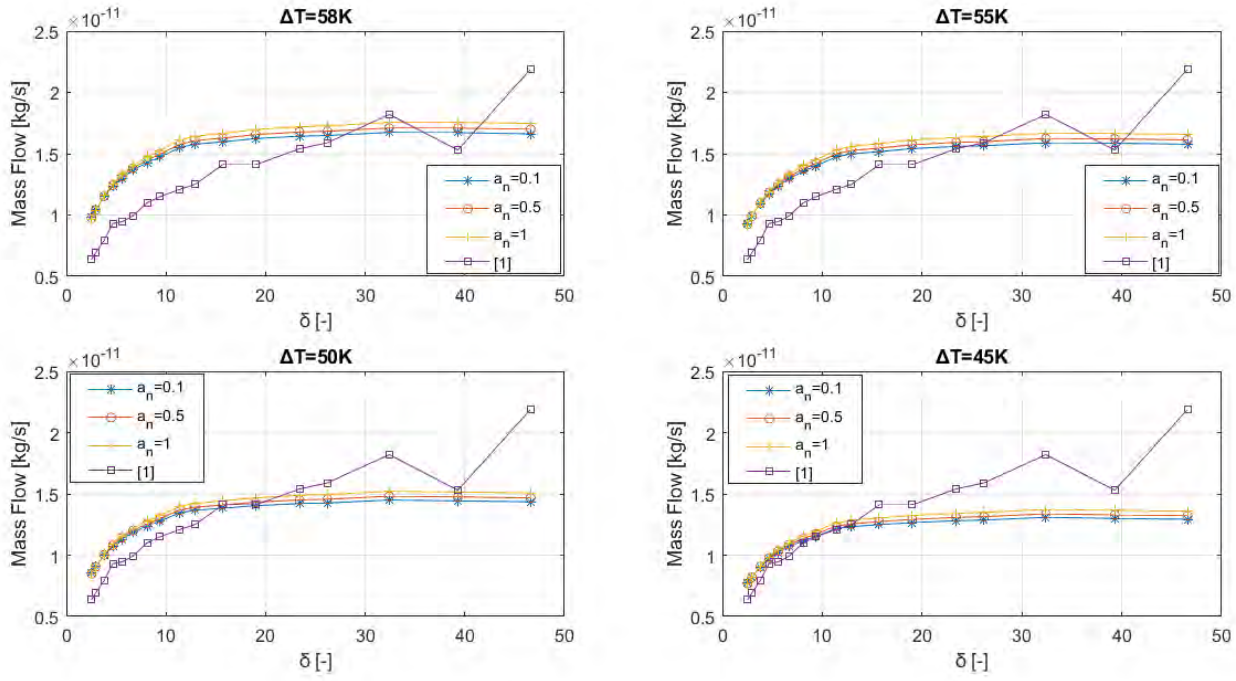

Figure E.9: Computational and experimental mass flow rates with CL boundary conditions for various values of a_n and temperature differences in the case of Kr (ΔT=58K)

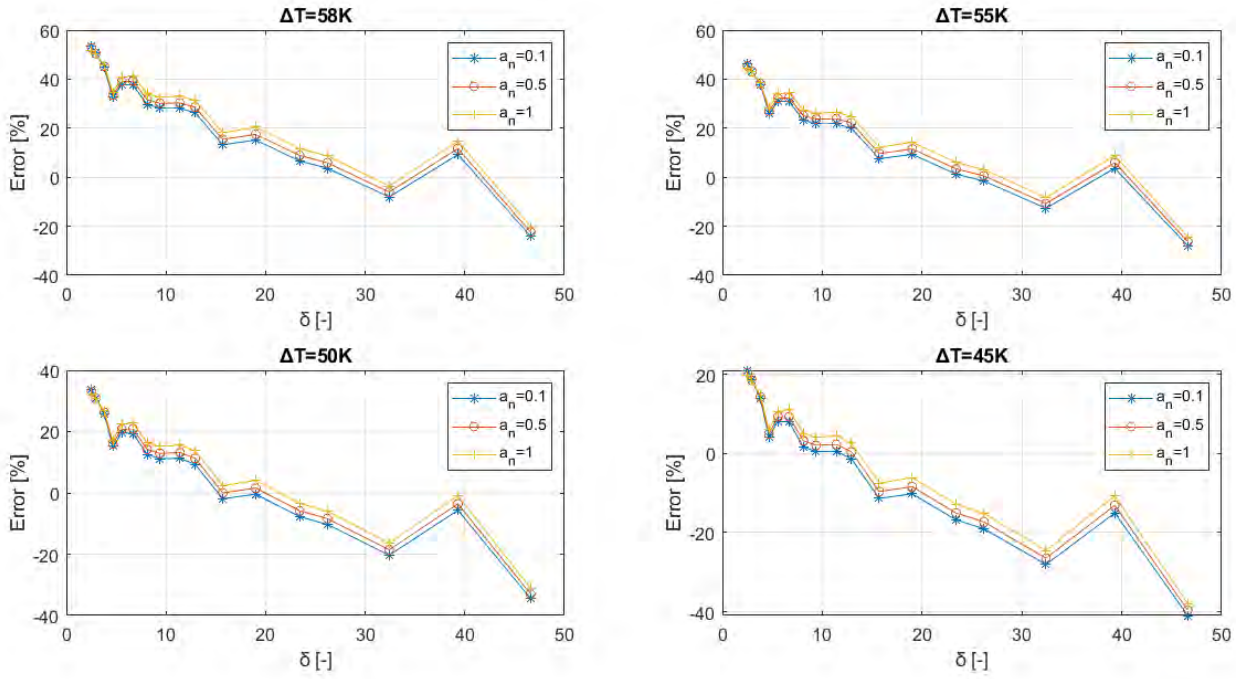

Figure E.10: Relative difference between computational and experimental mass flow rates with CL boundary conditions for various values of a_n and temperature differences in the case of Kr (ΔT=58K)